

Optimization of a neutrino beam for the study of CP violation with the LENA and JUNO detectors

Von der Fakultät für Mathematik, Informatik und Naturwissenschaften der RWTH Aachen University zur Erlangung des akademischen Grades einer Doktorin der Naturwissenschaften genehmigte Dissertation

vorgelegt von

M.Sc. Marta Meloni
aus Cagliari, Italien

Berichter: Universitätsprofessor Prof. Dr. Achim Stahl
Universitätsprofessor Prof. Dr. Livia Ludhova

Tag der mündlichen Prüfung: 09.12.2016

Diese Dissertation ist auf den Internetseiten der Hochschulbibliothek online verfügbar.

In Molise!
(Leo Ortolani)

Abstract

Optimization of a neutrino beam for the study of CP violation with the LENA and JUNO detectors

Neutrino beams are nowadays a commonly used and well investigated tool to study neutrino oscillations, e.g. T2K, NO ν A experiments. Beam neutrinos are produced by the decays of properly focused particles - mostly pions and kaons - generated by the collisions of accelerated protons with a target. The shape and composition of the obtained neutrino fluxes depend on the properties of the neutrino production apparatus. Primary beam, target, focusing system and decay tunnel must be optimized relatively to the neutrino detector, in order to achieve the highest possible sensitivity to oscillation parameters such as the CP-violating phase δ_{CP} .

This work focuses on the use of genetic algorithm for the optimization of simulated neutrino beams to the liquid scintillator neutrino detectors LENA (50kt), proposed in the Pyhäsalmi mine in Finland, and JUNO (20kt), under construction in Jiangmen, China, respectively from the European Spallation Source (ESS) in Lund, Sweden, and from the China Spallation Neutron Source in Dongguan, China.

As a result of the neutrino beam simulation and optimization, $\delta_{CP} = 0$ or $\delta_{CP} = \pi$ could be excluded by LENA with a 3σ sensitivity for $\sim 56\%$ of the whole δ_{CP} range at the chosen baseline; for JUNO the maximum value reached by the test statistics would be around $\Delta\chi^2 \sim 6$.

Zusammenfassung

Optimierung eines Neutrinostrahls zur Untersuchung der CP-Verletzung mit den LENA- und JUNO-Detektoren

Neutrinostrahlen sind heutzutage ein übliches und gut verstandenes Werkzeug zu Studien von Neutrino-Oszillationen, z.B. in den T2K, NO ν A Experimenten. Strahlneutrinos werden in den Zerfällen von den fokussierten Teilchen - meist Pionen und Kaonen - durch die Kollisionen der beschleunigten Protonen an einem Targetmaterial produziert. Die Form und die Zusammensetzung des resultierenden Neutrinostrahls sind abhängig von den Eigenschaften des Neutrino-Erzeugungsapparats. Der Primärstrahl, das Target, das Fokussystem und der Zerfallstunnel müssen relativ zu dem Neutrino-Detektor optimiert werden, um eine möglichst hohe Sensitivität gegenüber den Oszillationsparametern, wie der CP-Verletzungsphase δ_{CP} , zu erreichen.

Diese Arbeit konzentriert sich auf die Nutzung eines genetischen Algorithmus für die Optimierung der simulierten Neutrinostrahlen zu zwei Flüssigszintillator-Neutrino-Detektoren. Low-Energy-Neutrino-Astronomy (LENA) ist ein Detektor mit 50kt Szintillatormasse, vorgesehen in der Pyhäsalmi-Mine in Finnland. Jiangmen-Underground-Neutrino-Observatory (JUNO) ist ein Detektor mit 20kt Szintillatormasse, gegenwärtig im Bau in Jiangmen, China. Als jeweiligen Neutrinostrahlquellen werden die European-Spallation-Source (ESS) in Lund, Schweden, und die China-Spallation-Neutron-Source in Dongguan, China, angenommen.

Als Ergebnis der Neutrinostrahl-Simulation und -Optimierung, kann $\delta_{CP} = 0, \pi$ durch LENA mit einer 3σ -Sensitivität für $\sim 56\%$ des gesamten δ_{CP} -Bereichs ausgeschlossen werden. Für JUNO wird der von der Teststatistik erreichte Maximum $\Delta\chi^2 \sim 6$ betragen.

Contents

1	Introduction	1
2	Neutrino Physics	3
2.1	The neutrino	3
2.2	Neutrino interactions	3
2.2.1	Neutrino-electron elastic scattering	3
2.2.2	Neutrino weak scattering	4
2.3	Neutrino mixing	6
2.4	Neutrino oscillation	6
2.4.1	Oscillation parameters and mass hierarchy	7
2.4.2	Matter effects	8
2.4.3	CP violation	9
3	The source: neutrino beam setup	13
3.1	Introduction	13
3.2	The proton beam	14
3.3	The target	15
3.3.1	Target material	15
3.3.2	Target shape and size	15
3.4	The focusing system	15
3.5	The decay tunnel	17
4	The detectors: LENA and JUNO	19
4.1	Liquid scintillator neutrino detectors	19
4.1.1	Detection principle	19
4.1.2	Features and advantages of liquid scintillator detectors	20
4.2	The LENA detector	22
4.2.1	LENA location in Finland	22
4.2.2	LENA detector setup	22

4.2.3	Physics program	23
4.3	The JUNO detector	25
4.3.1	JUNO location	25
4.3.2	JUNO detector setup	25
4.3.3	JUNO physics goals	26
5	Determination of sensitivity to CP violation	29
5.1	Neutrino beam simulation	29
5.1.1	Beam setup	29
5.1.2	Determination of the neutrino flux	32
5.1.3	Test simulation	34
5.2	Determination of sensitivity to CP violation	36
5.2.1	Asimov data sets and Monte Carlo simulations	37
5.2.2	Neutrino oscillation and density parameters	38
5.2.3	Detector mass and baseline	38
5.2.4	Cross-sections	39
5.2.5	Energy reconstruction	40
5.2.6	Signal and background channels and efficiencies	42
6	Genetic Algorithm	45
6.1	Introduction	45
6.2	Definition of individuals	46
6.3	Fitness evaluation	47
6.4	Selection method	47
6.5	Crossover	48
6.6	Mutation	49
6.7	Behaviour of the algorithm	51
6.7.1	Effects of statistical fluctuations	51
6.7.2	Local optimization maxima	52
6.8	Implementation	53
7	Results	55
7.1	Optimization of the ESS-LENA neutrino beam	55
7.2	Beam optimization for the LENA detector	56
7.2.1	Best beam setup configurations for LENA	58
7.2.2	A good beam setup: an example	61
7.2.3	Effect of beam contamination	62
7.3	Beam optimization for the JUNO detector	64

7.3.1	Best beam setup configurations for JUNO	66
7.3.2	A “good” beam setup: an example	66
7.3.3	Effect of beam contamination	69
8	Conclusions	71
A	Beam parameters distributions for 30 generations	73
	Bibliography	81

Chapter 1

Introduction

The aim of this work is to assess the sensitivity to CP violation of the LENA and JUNO experiments with an optimized neutrino beam at a given baseline.

CP violation, i.e. the violation of the product of *charge conjugation* symmetry (C) and *parity* symmetry (P), is an urgent topic in modern physics since it could be a key to the explanation of one of the most important unsolved puzzles: the matter-antimatter asymmetry in the Universe.

Neutrinos are electrically neutral particles with small masses; they carry information about their sources and for this reason they are used in neutrino experiments to probe many terrestrial and extraterrestrial phenomena. The small interaction cross-sections, though, make neutrino detection extremely difficult and only possible with large detector masses.

Liquid-scintillator detectors have proven to be very efficient since the beginning of experimental neutrino physics and are used today in several experiments with target masses ranging from the order of one ton (Double Chooz) to one kiloton (KamLAND). *The next-generation liquid-scintillator detectors* will have target mass of tens of kilotons and be able to address a multitude of physics questions; two examples of such a large-volume detector are the detectors considered in this study: the *Low Energy Neutrino Astronomy* (LENA), a proposed 50kt European observatory, and the *Jiangmen Underground Neutrino Observatory* (JUNO), a 20kt detector currently under construction in Jiangmen, China.

Muon neutrino beams can be produced by proton accelerators in the direction of neutrino detectors to investigate intrinsic properties of neutrinos and could provide information on leptonic CP violation thanks to the phenomenon known as *neutrino oscillation*. The properties of the beam (energy spectrum, contamination) are decisive for the experiment's sensitivity to the studied oscillation parameters.

In this study two beam setups are optimized for LENA and JUNO to be used as neutrino accelerator experiments to research leptonic CP violation; the optimization procedure follows the principles of the so-called *genetic algorithm*, that allows to effectively explore the parameter space of a beam setup.

This thesis is structured as follows:

- chapter 2 reviews the fundamental aspects of neutrino physics that are most relevant to this work, including neutrino interactions and neutrino oscillations with the influence of CP violation and matter effects;
- in chapter 3 the basic components and features of the setup for the production of a neutrino beam are outlined.
- chapter 4 describes the main properties of liquid-scintillator detectors in general and provides more details on the LENA and JUNO detectors;
- chapter 5 illustrates the procedure to assess the sensitivity to CP violation of the two experiments, from the simulation of a neutrino beam to the oscillation analysis;
- chapter 6 explains the functioning of the genetic algorithm used in this work to optimize the neutrino beam parameters in order to obtain the highest sensitivity to CP violation;
- chapter 7 presents the results of the beam optimizations and gives an estimate for the maximum sensitivity reached by LENA and JUNO with accelerator neutrinos;
- in chapter 8 the work is summarized and conclusions are given.

Chapter 2

Neutrino Physics

This chapter gives a short summary of the aspects of neutrino physics that are most relevant to this work.

2.1 The neutrino

Neutrinos (ν) are elementary particles with no electric charge, only interacting through the gravitational and weak force (and therefore difficult to detect). Their existence was first suggested by Wolfgang Pauli in 1930 to explain the continuous electron energy spectrum in the β decay [1] and confirmed in 1956 by Reines and Cowan [2].

Experiments at the Large Electron Positron Collider (LEP) on the decay width of the Z-boson have proved the existence of three generations of active light neutrinos [3], associated with the three lepton families (flavours): the particle discovered by Cowan and Reines was actually an electron antineutrino ($\bar{\nu}_e$), while muon neutrino ν_μ was discovered in 1962 at Brookhaven National Laboratory [4] and tau neutrino ν_τ in 2001 at Fermilab [5].

According to the standard model of elementary particles, neutrinos are supposed to be massless; this last assumption is in contrast with a now-established phenomenon, the so-called neutrino oscillation.

2.2 Neutrino interactions

Neutrinos are detected in two main kinds of scattering processes that are here shortly presented (see [6]): non-elastic weak scattering on leptons and nuclei and neutrino-electron elastic scattering.

2.2.1 Neutrino-electron elastic scattering

Neutrinos can elastically scatter off electrons in interactions like $\nu + e^- \rightarrow \nu + e^-$; this interaction's cross-section is proportional to the neutrino energy:

$$\sigma(E_\nu) \sim \frac{\sigma_0 E_\nu}{m_e}, \quad \sigma_0 \sim 10^{-44} \text{cm}^2. \quad (2.1)$$

This kind of process does not have an intrinsic threshold but a detection threshold in order to have a signal above the background.

The scattering $\nu_e + e^- \rightarrow \nu_e + e^-$ has a charged current (mediated by the W boson) and a neutral current (mediated by the Z boson) contributions, whose Feynman diagrams are shown in 2.1, while the contributions for $\bar{\nu}_e + e^- \rightarrow \bar{\nu}_e + e^-$ are illustrated in 2.2.

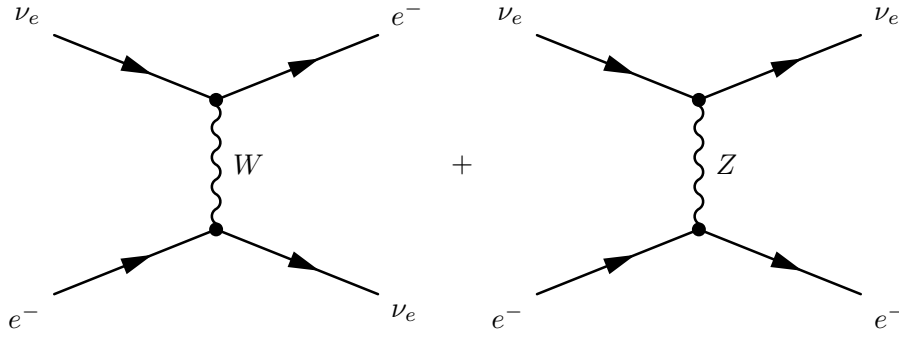


Figure 2.1: Charged-current (left) and neutral-current (right) tree-level contributions to the elastic scattering process $\nu_e + e^- \rightarrow \nu_e + e^-$.

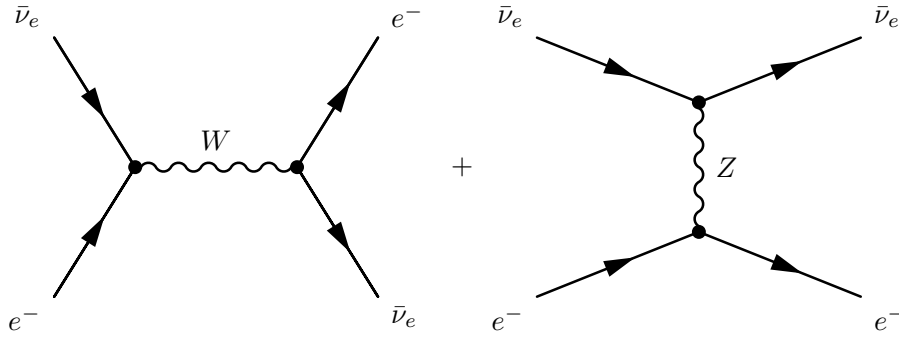


Figure 2.2: Charged-current (left) and neutral-current (right) tree-level contributions to the elastic scattering process $\bar{\nu}_e + e^- \rightarrow \bar{\nu}_e + e^-$.

The scattering $\nu_{(\mu,\tau)} + e^- \rightarrow \nu_{(\mu,\tau)} + e^-$ is a pure neutral current interaction and is represented by the right part of Figure 2.1, with μ, τ replacing e .

2.2.2 Neutrino weak scattering

Neutrinos can interact with matter through charged current or neutral current scattering processes of the type $\nu + A \rightarrow \sum_X X$. This scattering can occur on a target particle A at rest if the neutrino energy is greater than a threshold energy given by (see [6]):

$$E_\nu^{th} = \frac{(\sum_X m_X)^2}{2m_A} - \frac{m_A}{2}. \quad (2.2)$$

Different kinds of scattering processes can be more prominent depending on the energy of the neutrino: in the low-energy domain ($E_\nu \leq 100\text{MeV}$) the main interactions are *inverse beta decay* (IBD) and *neutrino-nucleus interactions*.

Inverse beta decay $\bar{\nu}_e + p \rightarrow e^+ + n$

The energy threshold for this reaction is $E_{\text{th}} = 1.806\text{MeV}$. It is the main detection channel in liquid-scintillator detectors because it produces a characteristic signature, given by a prompt signal from the annihilation of the positron and a delayed signal from the capture of the neutron.

In the high energy range, with $E_\nu > 100\text{MeV}$, the dominant interactions are (see [7]):

- **elastic and quasi-elastic scattering:** neutrinos can elastically scatter off an entire nucleon, freeing a nucleon (or multiple nucleons) from the interaction target. The elastic scattering is a neutral-current process, while the so-called “quasi-elastic scattering” is a charged-current interaction.
- **Resonance production:** Neutrinos excite the target nucleon to a resonance state; the resulting baryonic resonance (e.g. Δ) can then decay to a several possible mesonic final states and produce combinations of nucleons and mesons (pions).
- **Deep inelastic scattering:** if the neutrino energy is high enough, the interaction can resolve the individual quarks in a nucleon. This process involves the creation of a hadronic shower. The Feynman diagrams of the charged-current $\nu_\ell + N \rightarrow \ell + X$ and neutral-current $\nu_\ell + N \rightarrow \nu_\ell + X$ DIS process at lowest order are illustrated in Figure 2.3.

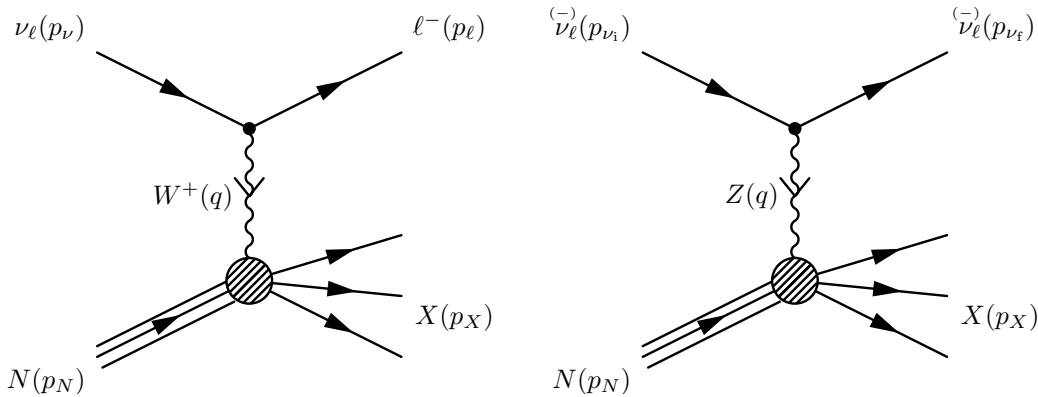


Figure 2.3: Charged-current (left) and neutral-current (right) deep inelastic scattering processes at lowest order. Diagrams taken from [6].

2.3 Neutrino mixing

Neutrino flavour eigenstates ν_α ($\alpha = e, \mu, \tau$) do not coincide with the mass eigenstates, which are solutions to the Schrödinger's equation that describes neutrinos' propagation in space, but are a linear superposition of them; the two sets are related through a mixing matrix:

$$|\nu_\alpha\rangle = \sum_i U_{\alpha i} |\nu_i\rangle \quad \text{and} \quad |\nu_i\rangle = \sum_\alpha U_{\alpha i}^* |\nu_\alpha\rangle \quad (2.3)$$

For antineutrinos the U matrix is replaced by its conjugate U^* .

Current data on neutrino oscillations can be described by 3-flavour neutrino mixing with at least 3 light neutrinos with different masses ($m_{1,2,3} < 1\text{eV}$, $m_1 \neq m_2 \neq m_3$); experimental data hint at the existence of sterile neutrinos (e.g. [8, 9]), but their role will not be discussed here.

At present it is not possible to determine whether neutrinos are Dirac ($\nu \neq \bar{\nu}$) or Majorana ($\nu \equiv \bar{\nu}$) particles.

The neutrino mixing matrix is called the Pontecorvo-Maki-Nakagawa-Sakata matrix U_{PMNS} and it is unitary if there are no sterile neutrinos, so that:

$$U^\dagger U = 1 \quad \sum_i U_{\alpha i} U_{\beta i}^* = \delta_{\alpha\beta} \quad \sum_\alpha U_{\alpha i} U_{\alpha j}^* \delta_{ij} \quad (2.4)$$

In the 3-flavour mixing frame, with $n = 3$ massive neutrinos, it can be parameterized by 3 mixing angles and CP-violation phases:

$$U_{PMNS} = \begin{pmatrix} c_{12}c_{13} & s_{12}c_{13} & s_{13}e^{-i\delta_{CP}} \\ -s_{12}c_{23} - c_{12}s_{23}s_{13}e^{i\delta_{CP}} & c_{12}c_{23} - s_{12}s_{23}s_{13}e^{i\delta_{CP}} & s_{23}c_{13} \\ s_{12}s_{23} - c_{12}c_{23}s_{13}e^{i\delta_{CP}} & -c_{12}s_{23} - s_{12}c_{23}s_{13}e^{i\delta_{CP}} & c_{23}c_{13} \end{pmatrix} \times \begin{pmatrix} 1 & 0 & 0 \\ 0 & e^{i\frac{\alpha_1}{2}} & 0 \\ 0 & 0 & e^{i\frac{\alpha_2}{2}} \end{pmatrix}$$

In the definition of the matrix element $U_{\alpha i}$ $s_{ij} = \sin\theta_{ij}$ and $c_{ij} = \cos\theta_{ij}$, where $(i, j = 1, 2, 3)$, with $\theta_{ij} = [0, \pi/2]$ [3]. δ_{CP} is the Dirac CP violation phase, while α_1 and α_2 are only non-zero if neutrinos are Majorana particles and do not influence the oscillation mechanism. Neglecting the Majorana phases the mixing matrix can be also parameterized as in 2.5:

$$\begin{pmatrix} \nu_e \\ \nu_\mu \\ \nu_\tau \end{pmatrix} = \begin{pmatrix} 1 & 0 & 0 \\ 0 & c_{23} & s_{23} \\ 0 & -s_{23} & c_{23} \end{pmatrix} \begin{pmatrix} c_{13} & 0 & s_{13}e^{-i\delta_{CP}} \\ 0 & 1 & 0 \\ -s_{13}e^{i\delta_{CP}} & 0 & c_{13} \end{pmatrix} \begin{pmatrix} c_{12} & s_{12} & 0 \\ -s_{12} & c_{12} & 0 \\ 0 & 0 & 1 \end{pmatrix} \begin{pmatrix} \nu_1 \\ \nu_2 \\ \nu_3 \end{pmatrix} \quad (2.5)$$

2.4 Neutrino oscillation

The phenomenon of neutrino oscillation consists in the change of neutrino flavour during propagation in space as a direct consequence of neutrino mixing and non-zero neutrino masses.

It was first suggested by Bruno Pontecorvo in 1967 [10] and has since been confirmed by many evidences from different experiments: first by Super-Kamiokande [11] and Sudbury Neutrino Observatory [12], then MACRO [13], Soudan [14], K2K [15], MINOS [16], T2K [17] and more

recently ANTARES [18], IceCube [19] and OPERA [20]. Neutrino oscillation is now an established explanation for the so-called "solar neutrino problem" deriving from the neutrino deficit recorded first by the Homestake experiment [21].

The probability of transition $\nu_\alpha \rightarrow \nu_\beta$ in vacuum is given by the square of the transition amplitude:

$$P(\alpha \rightarrow \beta) = |A(\alpha \rightarrow \beta)|^2 = |\langle \nu_\beta | \nu_\alpha(x, t) \rangle| \quad (2.6)$$

Using a plane wave description we can write the time evolution of the eigenstates as:

$$|\nu_{i(x,t)}\rangle = e^{-iE_i t} |\nu_{i(x,0)}\rangle. \quad (2.7)$$

$|\nu_{i(x,0)}\rangle$ is a neutrino emitted at time $t = 0$ in a position x with momentum p :

$$|\nu_{i(x,0)}\rangle = e^{ipx} |\nu_i\rangle. \quad (2.8)$$

From 2.3, 2.7 and 2.8 we can derive, for a neutrino emitted with flavour α after a time t :

$$|\nu_{(x,t)}\rangle = \sum_i U_{\alpha i} e^{-iE_i t} |\nu_{i(x,0)}\rangle = \sum_i U_{\alpha i} e^{-i(E_i t - px)} |\nu_i\rangle = \sum_i \sum_\beta U_{\alpha i} U_{\beta i}^* e^{-i(E_i t - px)} |\nu_\beta\rangle \quad (2.9)$$

Considering the relativistic nature of neutrinos, for $p \gg m_i$ and $E \approx p$ as neutrino energy we can write $E_i \simeq E + \frac{m_i^2}{2E}$ and $L = x = ct$ as the distance between the neutrino source and the detector. The oscillation probability over a distance L 2.6 can now be written as [22]:

$$P(\alpha \rightarrow \beta) = \sum_i \sum_j U_{\alpha i} U_{\alpha j}^* U_{\beta i}^* U_{\beta j} e^{-i(E_i - E_j)t} = \sum_i |U_{\alpha i} U_{\beta i}^*|^2 + 2\Re \sum_{i>j} U_{\alpha i} U_{\alpha j}^* U_{\beta i}^* U_{\beta j} e^{-i(\frac{\Delta m_{ij}^2}{2}) \frac{L}{E}} \quad (2.10)$$

In 2.10 $\Delta m_{ij}^2 = m_i^2 - m_j^2$; the first term is an average transition probability, while the second term is time-(space-)dependent.

Equation 2.10 shows that neutrino oscillations are only possible if at least one mass eigenstate is non-zero and if there is neutrino mixing (i.e. if there are non-diagonal terms in the PMNS matrix).

2.4.1 Oscillation parameters and mass hierarchy

Since the phenomenon of oscillation has been established, a large part of neutrino research has aimed to determine the values of the oscillation parameters: mixing angles, CP-violating phase and mass differences.

θ_{12} and Δm_{12}^2 are called "solar parameters" because they are better constrained by experiments on solar neutrinos; in fact, they were measured from a combined analysis of solar data with KamLAND data [23].

θ_{23} and Δm_{23}^2 are called "atmospheric parameters". θ_{13} was only proved to be non-zero in

2012 by the Daya Bay experiment [24].

The absolute values of neutrino masses have not been determined yet, nor has the sign of Δm_{23}^2 : this raises the problem of the so called "neutrino mass hierarchy", that is whether the mass eigenstates are ordered as $m_3 > m_2 > m_1$ (*normal hierarchy*) or as $m_2 > m_1 > m_3$ (*inverted hierarchy*).

Figure 2.4 illustrates the problem of mass hierarchy and shows the flavour content of the three neutrino mass eigenstates, depending on the value of $\cos\delta_{cp}$.

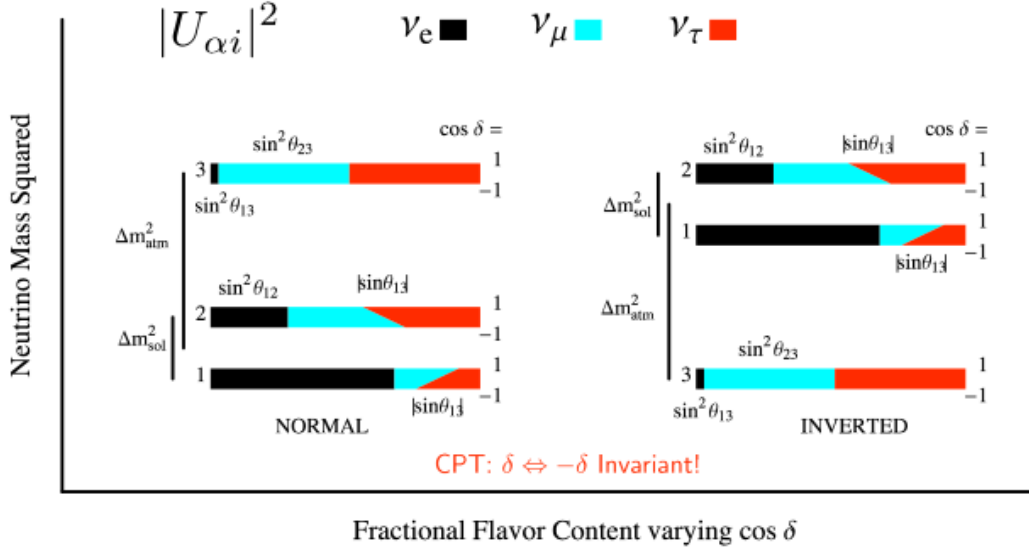


Figure 2.4: Flavour fraction of the three mass eigenstates as a function of δ_{cp} (δ) [25].

The present knowledge on the values of the oscillation parameters and their uncertainties is summarized in table 2.1.

Parameter	value
$\sin^2(2\theta_{12})$	0.846 ± 0.021
$\sin^2(2\theta_{23})$	$0.999^{+0.001}_{-0.018}$ (NH) $1.000^{+0.000}_{-0.017}$ (IH)
$\sin^2(2\theta_{13})$	$(9.3 \pm 0.8) \cdot 10^{-2}$
Δm_{21}^2	$(7.53 \pm 0.18) \cdot 10^{-5} eV^2$
Δm_{32}^2	$(2.44 \pm 0.06) \cdot 10^{-3} eV^2$ (NH) $(2.52 \pm 0.07) \cdot 10^{-3} eV^2$ (IH)

Table 2.1: Current values of neutrino oscillation parameters from [3]. NH = normal hierarchy, IH = inverted hierarchy.

2.4.2 Matter effects

While propagating in matter electron neutrinos have one interaction mode that is not available to ν_μ and ν_τ , that is elastic scattering off electrons by charged current reactions $\nu_e e \rightarrow \nu_e e$. This

extra interaction mode makes electron neutrinos' cross section larger, introducing an additional potential $V \equiv \pm\sqrt{2}G_F n_e$ to the Hamiltonian of the system, so that $H_0 \rightarrow H = H_0 + V$, where H_0 is the Hamiltonian in vacuum [26].

After diagonalization in the flavour base the Hamiltonian is:

$$H(n_e) = \frac{1}{2E} U \begin{pmatrix} 0 & 0 & 0 \\ 0 & \Delta m_{21}^2 & 0 \\ 0 & 0 & \Delta m_{31}^2 \end{pmatrix} U^\dagger + \begin{pmatrix} \pm\sqrt{2}G_F n_e & 0 & 0 \\ 0 & 0 & 0 \\ 0 & 0 & 0 \end{pmatrix} \quad (2.11)$$

In 2.11 G_F is the Fermi coupling constant and n_e is the electron density; the latter is related to the matter density ρ by $n_e \simeq 0.5\rho m_N$, m_N being the nucleon mass [27].

The positive sign applies to neutrinos while the negative sign applies to antineutrinos; this difference in the sign of the additional potential ensures that the changes in eigenstates and mixing parameters that follow from the change in the Hamiltonian are also different for neutrinos and antineutrinos.

The oscillation probability $\nu_\mu \rightarrow \nu_e$ in constant density matter at a distance L can be written to the leading order as [28]:

$$\begin{aligned} P(\nu_\mu \rightarrow \nu_e) &= \sin^2 \theta_{23} \sin^2 2\theta_{13} \frac{\sin^2(\Delta_{31} - aL)}{(\Delta_{31} - aL)^2} \Delta_{31}^2 \\ &+ \sin 2\theta_{23} \sin 2\theta_{13} \sin 2\theta_{12} \frac{\sin(\Delta_{31} - aL)}{\Delta_{31} - aL} \Delta_{31} \frac{\sin(aL)}{aL} \Delta_{21} \cos(\Delta_{31} - \delta_{CP}) \\ &+ \cos^2 \theta_{23} \sin^2 2\theta_{12} \frac{\sin^2(aL)}{(aL)^2} \Delta_{21}^2. \end{aligned} \quad (2.12)$$

where $a \equiv G_F n_e / \sqrt{2}$ and $\Delta_{ij} \equiv \Delta m_{ij}^2 L / 4E$. This is valid for normal and inverted hierarchy. For the CP conjugate process, $\bar{\nu}_\mu \rightarrow \bar{\nu}_e$ a and δ_{CP} must be replaced with $-a$ and $-\delta_{CP}$.

2.4.3 CP violation

CP violation in neutrino oscillation is a pure three - or more - flavour effect: it can be observed when at least two different Δm^2 and three mixing angles are involved in an interference between flavour oscillations.

Using the unitarity condition for the PMNS matrix, $U = U^*$, equation 2.10 can be rewritten for neutrinos and antineutrinos:

$$P(\nu_\alpha \rightarrow \nu_\beta) = \delta_{\alpha\beta} - 4 \sum_{i>j} \Re[U_{\alpha i} U_{\alpha j}^* U_{\beta i}^* U_{\beta j}] \sin^2(\Delta_{ij}) - 2 \sum_{i>j} \Im[U_{\alpha i} U_{\alpha j}^* U_{\beta i}^* U_{\beta j}] \sin(2\Delta_{ij}) \quad (2.13)$$

$$P(\bar{\nu}_\alpha \rightarrow \bar{\nu}_\beta) = \delta_{\alpha\beta} - 4 \sum_{i>j} \Re[U_{\alpha i} U_{\alpha j}^* U_{\beta i}^* U_{\beta j}] \sin^2(\Delta_{ij}) + 2 \sum_{i>j} \Im[U_{\alpha i} U_{\alpha j}^* U_{\beta i}^* U_{\beta j}] \sin(2\Delta_{ij}) \quad (2.14)$$

The difference between oscillation probabilities of neutrinos and antineutrinos provides the

simplest measure of CP violation [28]:

$$\Delta P_{\nu\bar{\nu}\alpha\beta} \equiv P(\nu_\alpha \rightarrow \nu_\beta) - P(\bar{\nu}_\alpha \rightarrow \bar{\nu}_\beta) = -16J_{\alpha\beta} \sin\Delta_{12} \sin\Delta_{23} \sin\Delta_{31} \quad (2.15)$$

$$J_{\alpha\beta} \equiv \Im(U_{\alpha 1} U_{\alpha 2}^* U_{\beta 1}^* U_{\beta 2}) = \pm J, \quad J \equiv s_{12} c_{12} s_{23} c_{23} s_{13} c_{13}^2 \sin\delta_{CP} \quad (2.16)$$

with positive (negative) sign for (anti-)cyclic permutation of the flavour indices.

From 2.15 we can see that it is impossible to observe CP violation if $\delta_{CP} = 0$ or π or if two or more masses are degenerate.

The expression also shows that CP violation cannot be observed in disappearance channels ($\alpha = \beta$) because $\nu_\alpha \rightarrow \nu_\alpha$ and $\bar{\nu}_\alpha \rightarrow \bar{\nu}_\alpha$ are related by CPT.

The main oscillation channel in this study is between muon and electron neutrino, for which we can summarize the CP and T relations in table 2.2.

$$\begin{array}{ccc} & & \text{CP} \\ & \nu_\mu \rightarrow \nu_e & \Leftrightarrow \bar{\nu}_\mu \rightarrow \bar{\nu}_e \\ \text{T} & \Downarrow & \Downarrow \text{T} \\ & \nu_e \rightarrow \nu_\mu & \Leftrightarrow \bar{\nu}_e \rightarrow \bar{\nu}_\mu \\ & & \text{CP} \end{array}$$

Table 2.2: CP and T relations for the $\nu_\mu \rightarrow \nu_e$ channel.

The horizontal processes are related by CP, the vertical processes are related by T and the diagonal processes are related through CPT, so that:

$$P(\nu_\mu \rightarrow \nu_e, \delta) = P(\bar{\nu}_\mu \rightarrow \bar{\nu}_e, -\delta) = P(\nu_e \rightarrow \nu_\mu, -\delta) = P(\bar{\nu}_e \rightarrow \bar{\nu}_\mu, \delta). \quad (2.17)$$

Figure 2.5 shows the ν_μ and $\bar{\nu}_\mu$ oscillation probabilities in matter as a function of energy for different values of δ_{CP} .

Matter effects must be taken into account since they can mimic a fake CP violating effect, making ΔP as defined in 2.15 different from zero even for $\delta_{CP} = 0, \pi$, as illustrated in figure 2.6. The CP-invariant factor in matter $J(m)$ is related to the value in vacuum by [28]:

$$J(m) = \frac{\Delta m_{21}^2 \Delta m_{32}^2 \Delta m_{31}^2}{\Delta m_{21}^2(m) \Delta m_{32}^2(m) \Delta m_{31}^2(m)} J. \quad (2.18)$$

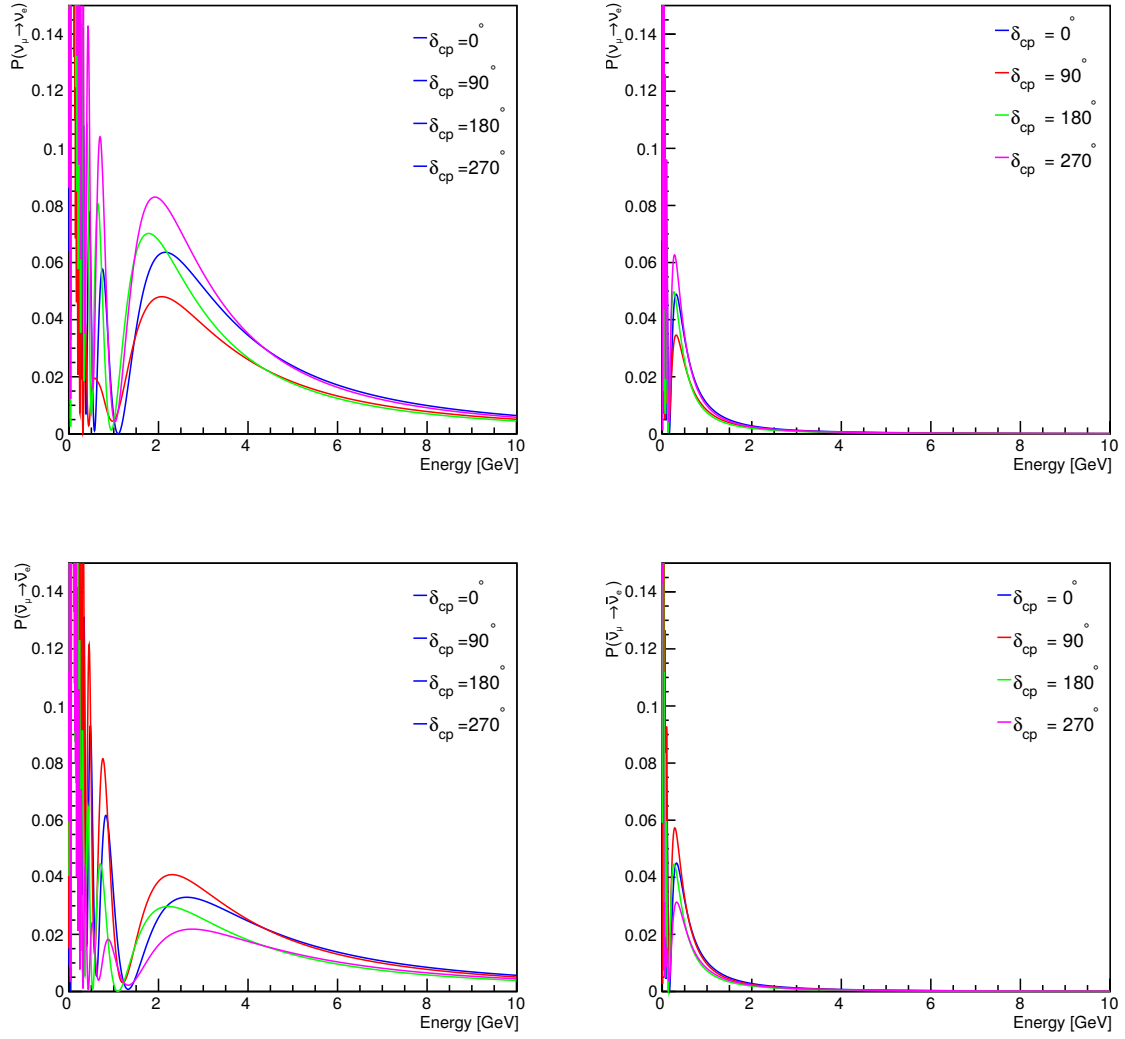


Figure 2.5: Oscillation probability for ν_μ as a function of energy for different values of δ_{CP} (left: LENA, right:JUNO).

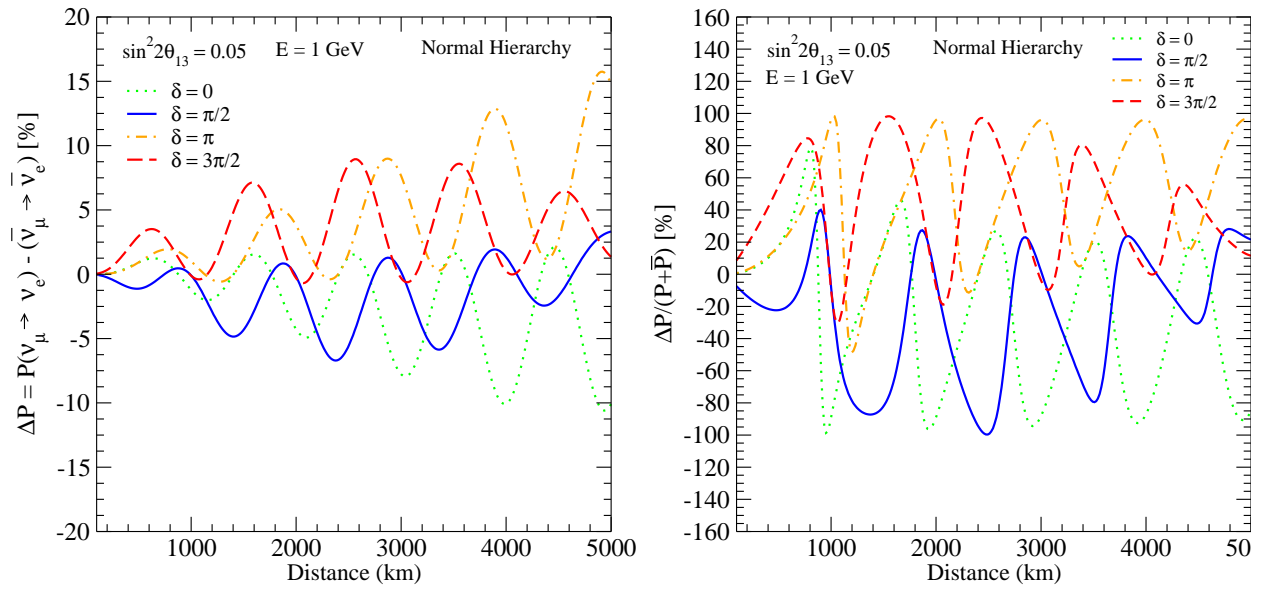


Figure 2.6: $\Delta P \equiv P(\nu_\mu \rightarrow \nu_e) - P(\bar{\nu}_\mu \rightarrow \bar{\nu}_e)$ as a function of distance for $E = 1 \text{ GeV}$ for different values of δ_{CP} . Figure taken from [28].

Chapter 3

The source: neutrino beam setup

3.1 Introduction

Neutrino beams have been extensively used for decades now to investigate neutrino physics issues.

The first accelerator based neutrino beam was produced in 1962 at BNL (Brookhaven National Laboratory) from a 15 GeV proton beam shot into a beryllium target. That experiment led to the discovery of the muon neutrino, awarded with the Nobel prize to Lederman, Schwartz and Steinberger in 1988 [4].

Since then accelerator based neutrino experiments have studied neutrino oscillations, with measurements of neutrino mixing parameters (Minos, T2K, *No ν a*, Opera - see [16, 17, 29, 20]), and non-standard neutrino mixing (LSND [8], MiniBoone [9]). They have also been used for electroweak tests and to investigate neutrino interactions (e.g. Minerva, MicroBOONE [30, 31]).

The main components of the apparatus for the production of a neutrino beam are (see Figure 3.1):

- proton beam;
- target;
- focusing system;
- decay tunnel.

To obtain a conventional neutrino beam, protons of chosen energy are shot to interact with a target, where they produce secondary particles - pions and kaons. These secondary particles are focused by a magnetic horn system and decay in a decay region in the following main leptonic modes (for negatively charged particles the decay modes are charge conjugates of the modes below)[3]:

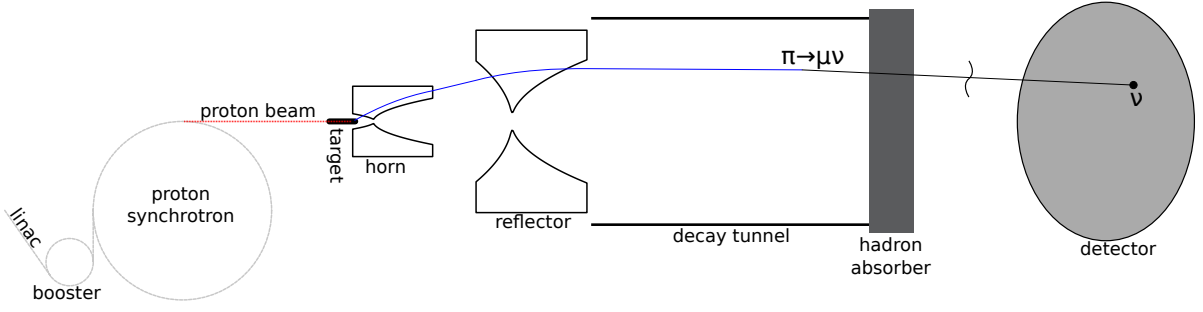


Figure 3.1: The picture illustrates the basic components of the apparatus for the production of a neutrino beam.

$\pi^+ \rightarrow \mu^+ \nu_\mu$	$(99.98770 \pm 0.00004)\%$
$\mu^+ \nu_\mu \gamma$	$(2.00 \pm 0.25) \times 10^{-4}$
$e^+ \nu_e$	$(1.230 \pm 0.004) \times 10^{-4}$
$K^+ \rightarrow \mu^+ \nu_\mu$	$(63.55 \pm 0.11)\%$
$\pi^0 e^+ \nu_e$	$(5.07 \pm 0.04)\%$
$\pi^0 \mu^+ \nu_\mu$	$(3.353 \pm 0.034)\%$

The neutrino beam produced in this way is mainly composed of ν_μ (or $\bar{\nu}_\mu$, depending on the focusing mode), with a small contamination from $\bar{\nu}_\mu$ (ν_μ) plus ν_e and $\bar{\nu}_e$, as can be seen in Figure 5.5.

Setups for the production of a neutrino beam usually contain also a beam dump at the end of the decay region to absorb muons and undecayed secondaries; since the beam dump doesn't affect the produced neutrino flux, it was not simulated in this study.

The next paragraphs describe the elements of the neutrino beam setup as they are commonly used.

3.2 The proton beam

The proton beam is the first ingredient for the production of a neutrino beam.

The beam power is defined as the product of the number of protons on target per year (*p.o.t./y*) and the proton energy.

The number of produced neutrinos depends on the proton beam power; their energy depends on the energy of the parent particles (pions and kaons), which in turn depends on the initial proton energy. Proton energies can vary from less than 8GeV (FNAL Booster [32]) to 400GeV (the CNGS beam from the CERN SPS proton driver [33]), while beam power ranges from $5 \cdot 10^{-3}$ MW (KEK [34]) to 5MW (planned for the European Spallation Source - ESS [35], producing 10^{20} *p.o.t./y*).

In this work the properties of the acceleration facility (LINAC or synchrotron, number of

protons per bunch, repetition rate) were not considered; only the number of *p.o.t./y* was simulated, as a function of beam energy and beam power.

3.3 The target

The proton target is the second crucial component of a neutrino beam production setup.

The target material, its shape and size determine the amount of proton interactions and the production of secondary particles, as well as their final direction and the probability to be focused in a convenient direction.

The amount of proton interactions also influences the temperature of the target and the required cooling, but this issue is not addressed in this work.

The choice of the proton target must take into account several contrasting needs and correlations with the other parts of the setup, like the focusing system.

3.3.1 Target material

In choosing the target material one should consider that in materials with a low atomic number Z protons can interact without losing a large amount of energy. For this reason elements like Beryllium, Aluminium and Carbon are usually preferred ([34]); nonetheless, an adequate balancing of the target dimensions can give good results with high- Z materials, too.

3.3.2 Target shape and size

The most common shapes chosen for proton targets are cylinders or rulers, with the longest dimension along the direction of the beam, so that protons have larger probability to interact and more neutrinos can be produced. The length l_{tar} of the target is normally chosen to be $l_{int} < l_{tar} < 2 \cdot l_{int}$, where l_{int} is the *nuclear interaction length*. For configurations with high beam power more complex designs have been proposed (see [36]) with a granular target composed of titanium spheres; this design would allow the coolant to flow between the spheres and act more effectively in the high irradiation environment.

3.4 The focusing system

A proton striking a target with momentum p_0 produces a secondary particle emerging at an angle θ from the beam axis, with longitudinal momentum p_z and transverse momentum p_T (see Fig. 3.2).

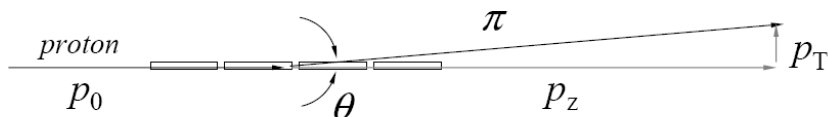


Figure 3.2: A secondary pion produced by a proton striking a segmented target. Picture taken from [37].

The number of π^+ produced in the interaction of protons with the target grows almost linearly

with the momentum of the incident proton. The momentum of the pions also scales with the energy of the protons (see [37]).

Production spectra in transverse momentum p_T should be independent of $x_F \simeq p_z/p_0$ - peak transverse momentum is 250MeV for secondaries [37]. This is important because transverse momentum controls the divergence of the secondary beam; the amount of p_T to remove by focusing does not grow rapidly with pion momentum.

The requested neutrino beam energy is achieved by focusing a particular secondary beam pion momentum.

Neutrino beam setups are provided with a focusing system composed of one or more so-called *magnetic horns*, devices designed to increase the flux of neutrinos by focusing the parent mesons in the most convenient directions.

A magnetic horn, as first invented by Simon van der Meer [38], is made of two thin conductor layers that, by circulating an electric current, produce a magnetic field to give a kick to transverse momentum p_T and deflect charged pions in the radial directions (see Fig. 3.3).

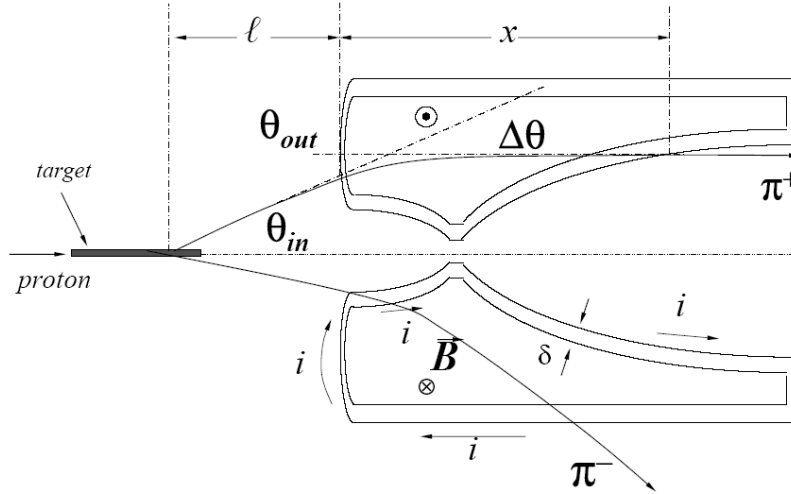


Figure 3.3: Trajectories of a π^+ and a π^- through a parabolic horn. In the picture θ_{in} indicates the initial angle of the pion with respect to the beam axis before focusing, while θ_{out} represents the final angle and $\Delta\theta$ their difference. δ indicates the thickness of the horn, \vec{B} the induced magnetic field inside the horn, ℓ is the distance traversed before focusing and x the pathlength through the horn. Figure taken from [37].

In this work the simulated focusing system was composed by two different parabolic horns, both 2.97 m long, at a 4.03 m distance from each other, as in Figure 5.3).

A parabolic horn focuses a given momentum for all possible entry angles. If the curve of the inner conductor is described by $z = ar^2$, the transverse momentum kick gives a change in the direction $\Delta\theta = \frac{Bx}{p}$, with $x = 2ar^2$ =pathlength through the horn.

Particles entering the horn at larger radii traverse a thick layer of material; for this reason horns are often designed with tapered conductor thicknesses, where the neck region is the thickest.

Palmer first developed the idea of a multi-horn system (see Fig. 3.4) [39], with the second horn collecting particles not properly focused by the first horn; the aperture of the second horn is larger than that of the first horn so that the properly focused particles can travel unperturbed.

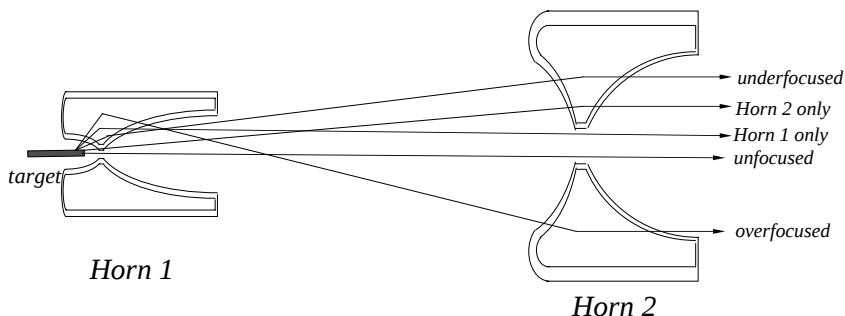


Figure 3.4: Two-lens focusing system: the second horn, at a considerable distance from the target, improves the collection of secondaries that are ill-focused by the first horn. Figure taken from [37].

The position of the target with respect to the focusing system influences the focused momenta and the final neutrino spectra: the peak energy of neutrinos increases when the target is closer or inside the (see [37, 40]).

When the currents are circulating in the horns so that π^+ and K^+ are focused along the beam axis, the beam is said to operate in *positive focusing mode* (PF) and will have ν_μ as its main component; vice versa, when the direction of the currents is inverted π^- and K^- are focused: the beam is in *negative focusing mode* (NF) and $\bar{\nu}_\mu$ will be the principal component.

3.5 The decay tunnel

A long and broad pipe is placed next to the focusing system along the beam direction to allow drift space for secondary particles to decay; for example, a 5GeV pion has $\gamma = 35$, that means it travels $\gamma\beta c\tau_\pi \sim 280\text{m}$ before decaying. Nonetheless, one must consider that a longer tunnel also provides drift space for *muon decay*, that leads to a bigger ν_e contamination of the beam, since $\pi \rightarrow \mu\nu_\mu \rightarrow (e\nu_e\nu_\mu)\nu_\mu$.

The decay tunnel diameter is also not irrelevant to the produced neutrino flux because a wider pipe allows for a larger divergence of underfocused low-energy secondaries.

Decay pipes are most commonly evacuated or filled with He gas as in T2K [17] to reduce absorption and scattering probability for the secondary particles and avoid loss of neutrinos.

Chapter 4

The detectors: LENA and JUNO

This chapter will illustrate the main features of the two neutrino detectors involved in this study, after a short general description of liquid scintillator detectors.

4.1 Liquid scintillator neutrino detectors

The use of scintillating material is now an established technique for the detection of charged particle radiation and of neutrinos (especially in the low energy region, up to the order of 10 MeV). Liquid scintillator was used in the experiment that led to the first confirmation of the existence of neutrinos ($\bar{\nu}_e$, see [2]) and it has been used since in many other detectors that provided measurements on solar and geo-neutrinos (KamLAND [23] and Borexino [41], [42]) and constraints on oscillation parameters like θ_{13} (Daya Bay [24], Double Chooz [43] and RENO [44]).

Liquid scintillator neutrino detectors can be called *unsegmented* detectors, since the target material is homogeneously distributed in a single volume and belong to the category of *real-time* detectors, because a time stamp can be assigned to each observed event.

4.1.1 Detection principle

A liquid scintillator for radiation detection is typically made up of two components:

- a **solvent**, i.e. the scintillating material that is the target of interactions: liquid scintillators are organic materials made of aromatic hydrocarbon compounds with benzene-ring structures; among the most used solvents are LAB (*linear alkylbenzene*, $C_{18}H_{30}$) and PXE (*phenyl-*o*-xylylene*, $C_{16}H_{18}$).

Charged particle radiation or photons deposit energy in the scintillator material, exciting the free valence electrons in the benzene rings; the deexcitation occurs with emission of ultraviolet light in the phenomenon of *luminescence* (*fluorescence* if the time τ between excitation and light emission is $\sim 10^{-9} - 10^{-8}$ s or *phosphorescence* for $\tau \gtrsim 10^{-4}$ s), with an energy spectrum characteristic of the material.

- a **solute**: since the emission and absorption spectra of the solvent often overlap at least partially, a *wavelength shifter* (also called a *fluor*) is needed to prevent the solvent from

re-absorbing the scintillation light; the scintillator transfers the excitation energy to the solute, which emits light in a different (usually higher) wavelength region, for which the solvent is transparent. Examples of wavelength shifters, usually added to a scintillator mixture in a concentration of a few g/l, are PPO (*2,5-diphenyloxazole*, $C_{15}H_{11}NO$) and bis-MSB (*1,4-Bis(2-methylstyryl)benzene*, $C_{24}H_{22}$).

Light from the scintillator is then collected by a photosensor and converted in electric signal that can be digitized and processed by the *data acquisition system* (DAQ).

The most common kind of photosensor is the *photomultiplier tube* (PMT), often combined with a *light concentrator* to increase the light collection area. In a PMT photons incoming on an evacuated tube are collected by a *photocathode* and converted through photoelectric effect to *photoelectrons*; these are accelerated by an applied electric field to a series of electrodes (*dynodes*), each of which multiplies the number of free electrons, leading to a cascade that is finally collected at an *anode* as measurable current, amplifying the initial signal $10^3 - 10^8$ times (see 4.1).

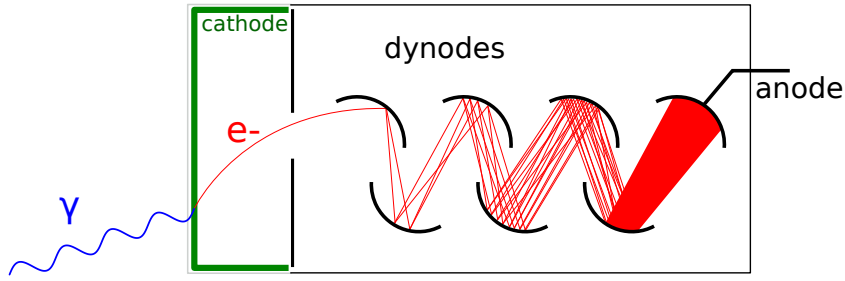


Figure 4.1: Schematical view of a photomultiplier tube.

4.1.2 Features and advantages of liquid scintillator detectors

The main advantages of liquid scintillator detectors are (see [45]):

- **sensitivity to energy:** the light emitted by the scintillator is directly proportional to the exciting energy deposited by the incoming particle. The *light yield* of the scintillator is defined as the number of photons emitted per amount of energy deposited by an ionizing particle and it is directly related to the energy resolution and the energy threshold of the detector.
- **Fast time response:** the decay time of liquid scintillators is of the order of 3-4ns. This allows the detectors to accept high count rates and to perform *real time* neutrino detection, attributing a time stamp to each event.
- **Pulse shape discrimination.** The radiative decay of the excited scintillator molecules can be described by an exponential function with several components depending on the population of the electron states and on the deexcitation processes involved:

$$n(t) = \sum n_i e^{-\frac{t}{\tau_i}} \quad (4.1)$$

where n_i is the amplitude of a process and τ_i its decay constant. The amplitude of each time component depends on the energy deposition per unit length, which is different for particles with different ionizing power; so an analysis of the pulse shape can discriminate incoming particles and improve background rejection.

- **Track reconstruction:** even though scintillation light emitted by low-energy events is isotropically distributed and does not carry directional information, high-energy particles create long ionization tracks; the superposition of spherical light waves along a track forms a light front similar to a Cherenkov light cone, whose shape can be used to resolve energy and momentum of the incident particle, as it was recently found out [46].

It is essential, when designing a liquid scintillator detector, to take into account the **attenuation length** L of the scintillator: this is defined as the length after which the number of photons $N(x)$ has dropped to $1/e$ of its initial value N_0 because of the absorption and scattering processes that occur in light propagation:

$$N(x) = N_0 e^{-\frac{x}{L}} \quad (4.2)$$

$$\frac{1}{L} = \frac{1}{l_A} + \frac{1}{l_S} \quad (4.3)$$

where l_A is the *absorption length*, accounting for the phenomena in which scintillation photons are absorbed by molecules, and l_S is the *scattering length*, accounting for Rayleigh scattering off the bound electrons of molecules in the mixture, Mie scattering from dirt or dust particles in the liquid and absorption-re-emission processes that change the photons' direction (see [47]).

The attenuation length is characteristic of the scintillator material and depends on the photon energy.

The **energy resolution** of a particle detector is defined as the relative uncertainty ΔE on the *visible energy* E (i.e. the energy of an incoming particle that is deposited in the detector, without escaping it or being converted to an undetectable form).

For a liquid scintillator detector a model for the energy resolution is ([48]):

$$\frac{\Delta E}{E} = \sqrt{a^2 + \frac{b^2}{E} + \frac{c^2}{E^2}} \quad (4.4)$$

where the parameter a accounts for energy leakage and non-uniformity of the detector, b depends on the statistics of detected photo-electrons and c takes into account systematic uncertainties related to background and noise.

The energy resolution of a liquid scintillator detector is usually good and accompanied by the absence of an intrinsic energy threshold.

Other important aspects in choosing and handling the scintillator mixture are its **radiopurity** (i.e. the contamination with radionuclides as ^{238}U , ^{232}Th and ^{40}K), that affects backgrounds, and safety issues like flammability.

4.2 The LENA detector

LENA (*Low Energy Neutrino Astronomy*) is a liquid scintillator neutrino detector that has been proposed within the LAGUNA-LBNO design studies (see [49]) as a neutrino observatory in order to address a variety of physics questions [50].

While Borexino (278t target mass) and KamLAND (1kt target mass) have proven the capabilities of the liquid scintillator technology, a next-generation detector like LENA at a new mass scale (50kt) would provide high statistics (hence high precision) neutrino measurements from astrophysical and terrestrial sources.

4.2.1 LENA location in Finland

The LAGUNA studies investigated the possibility of building new large size neutrino observatories in seven European locations. One of the favourite sites according to those studies would be the *Pyhäsalmi mine* in Finland: this is a currently operational mine, situated $\sim 1450\text{m}$ below ground at its deepest level, which would provide the detector with more than 4000m.w.e. (*meters water equivalent*) shielding.

The closest nuclear power plant, that would be source of background reactor neutrinos, is 350km away from Pyhäsalmi.

The Pyhäsalmi mine already hosts the *Centre for Underground Physics in Pyhäsalmi* and would allow the possibility to use the existing infrastructure to ease the excavation and construction works.

A view of the LENA detector in the Pyhäsalmi mine is given in figure 4.2.

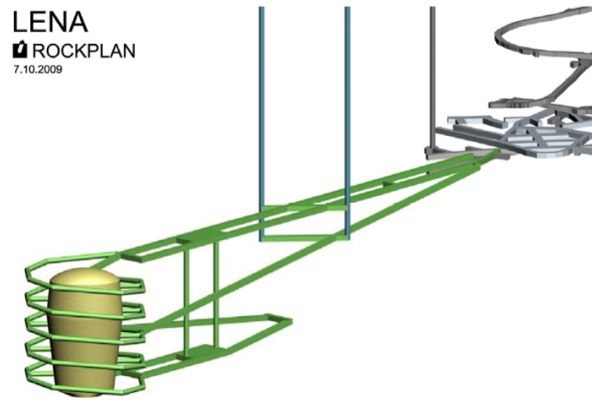


Figure 4.2: External view of the LENA detector at the Pyhäsalmi mine [50].

4.2.2 LENA detector setup

Figure 4.3 shows the planned design for the LENA detector in the Pyhäsalmi mine.

A $\sim 115\text{m}$ tall **cavern** hosts the detector: its walls are egg-shaped in order to better withstand horizontal and vertical stresses from the surrounding rock.

A **water-filled volume** with radius greater than 2m separates the cavern walls from the external side of a concrete tank containing the inner volumes of the detector; this volume acts as a shield against external radioactivity and fast neutrons produced by incoming cosmic rays

and is planned to be equipped with about 2000 PMT so that it can be used as a Cherenkov veto against incident muons.

The **concrete tank** has a height of 96m and an inner radius of 16m; its thickness ranges from 30cm to 60cm because of cylindrical cavities in the concrete allowing for installations (e.g. for cooling or cables).

A **muon veto system** is placed on top of the concrete tank to track muons entering the detector from above; this muon veto is right below the 15m height dome containing all the **electronics equipment** necessary for data acquisition.

Inside the tank a **buffer volume filled with liquid scintillator** provides shielding against radiation and contaminants from the concrete walls. The buffer volume also hosts a stainless steel scaffolding structure holding the optical modules.

The detector will be equipped with ~ 30000 **optical modules** (OM): each OM includes a 12 inches PMT and an attached light concentrator, both contained in a steel encapsulation to resist pressure from liquid scintillator at the bottom of the tank. The space inside the OM encapsulation is filled with non-scintillating mineral oil in order to absorb γ rays from radioactivity in the PMT glass. The optical modules are placed so that their apertures are at the edge of the target volume and an optical shielding is between them along the side of the support structure prevents light detection from the buffer region. The total number of optical modules would bring a 30% optical coverage of the detector's inner surface; considering that each OM has a 20% photo detection efficiency, the light detection efficiency in LENA would be $\sim 6\%$.

The **neutrino target volume** is a 96m tall cylinder and with a 14m radius filled with ~ 50 kt liquid scintillator; the chosen scintillator mixture is made of LAB as the solvent and concentrations of 3g/l PPO and 20mg/l bis-MSB for the fluors, resulting in a peak in the emission spectrum at 430nm wavelength with a fast decay component of about 4.4ns. The LAB-PPO-bis-MSB admixture satisfies the requirements for a large attenuation length (~ 15 m) and high light yield ($\sim 10^4$ photons/MeV) due to the size of the detector, with the advantage of a high number of free target protons, in addition to a wide experience in the use of LAB from other experiments.

4.2.3 Physics program

LENA has been planned as a multi-purpose facility, focusing mainly but not exclusively on low-energy neutrinos from astrophysical sources. Besides measurements of neutrinos from sources like the Sun or galactic core-collapse supernovae, LENA could provide precious information on the Diffuse Supernova Neutrino Background (DSNB), geoneutrinos and neutrino oscillation at short distances with the use of a strongly radioactive probe placed close to the detector.

In the GeV energy range LENA could offer the possibility to lead research on proton decay or, as investigated in this study, be used as a far detector for a long-baseline neutrino experiment.

The following paragraphs provide a short overview on the main topics of LENA's physics program.

Solar neutrinos LENA could perform measurements of neutrinos from the Sun from different production mechanisms; detection of **pep** neutrinos would probe oscillations in the MSW

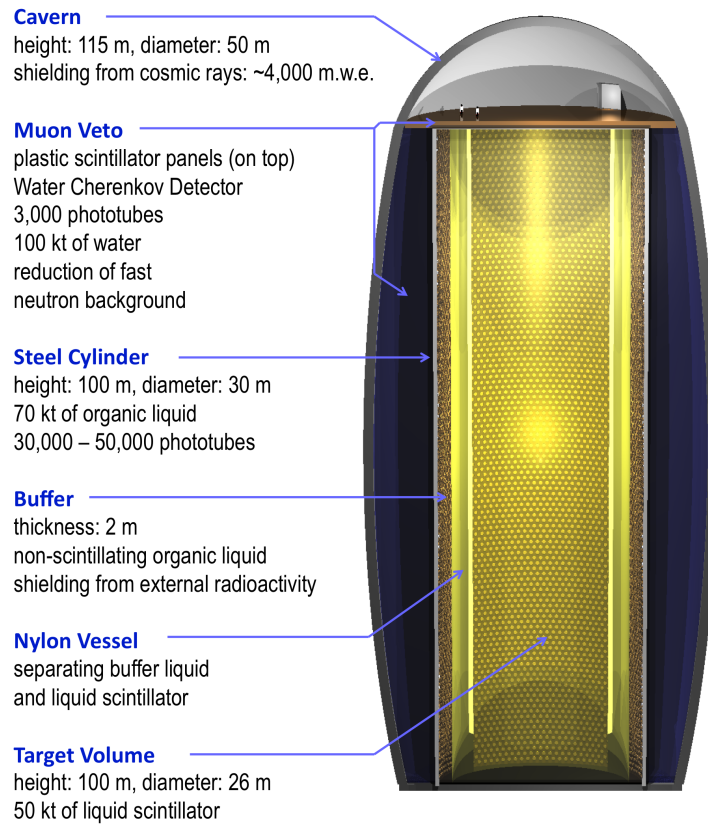


Figure 4.3: Schematical view of the LENA detector [50].

transition region while **CNO** neutrinos would give insight on solar metallicity; these measurements could be accomplished through the use of a fiducial volume of 30kt, necessary to deal with the gamma ray background from the photomultiplier tubes, that would also allow for the detection of low-energy ^8B neutrinos above 2MeV; above 3MeV a time and space cut would suppress the cosmogenic ^{10}C background. ^7Be would be detected with a very high statistics (10^4 events/day in a 35kt fiducial volume), making it possible to measure temporal variation of the solar neutrino flux.

Supernova neutrinos If a supernova collapse occurred in the Milky Way at a 10kpc distance LENA would detect around 10^4 events from the main channel (inverse beta decay), which, thanks to the detector's high energy resolution and flavour identification would give information on oscillation effects that are sensitive to the neutrino mass hierarchy.

LENA would be able to measure the DSNB in the 9.5-25MeV energy range, because of indistinguishable background from reactor and atmospheric neutrinos, as well as neutral current interactions; the latter background can be reduced through pulse shape discrimination with a loss of 60% of the signal. Detection of 20-40 events in 10 years would confirm the existence of DSNB at a 3σ level, while observation of no signal would set an upper limit on the DSNB flux.

Geoneutrinos Geoneutrinos are $\bar{\nu}_e$ produced in the beta decays of radioactive isotopes in the Earth. LENA could measure the geoneutrino flux from the U and Th chains via inverse beta decay (while detection of neutrinos from ^{40}K is forbidden by the 1.8MeV threshold of the IBD reaction). The main backgrounds for the geoneutrino detection would be given by neutrons produced inside the target by alpha decays of ^{210}Po causing $^{13}\text{C}(\alpha, n)^{16}\text{O}$ reactions and fast neutrons emitted in beta decays of ^9Li and ^8He produced by cosmic muons crossing the detector; the latter background can be suppressed by applying a veto for a 2m radius around each muon track, while the expected rate for the $^{13}\text{C}(\alpha, n)^{16}\text{O}$ background is 10 ± 1 events per year if LENA reaches the same radiopurity levels as Borexino.

The geoneutrino flux could be measured with a 1% precision after 10 years, providing a test for current geochemical models, while the abundance ratio U/Th could be determined with 6% precision in 10 years.

Proton decay can be investigated in liquid scintillator detectors through the favourite channel $p \rightarrow K^+ + \bar{\nu}$. This decay mode has a clear signature, given by a prompt scintillation signal from the kaon and a delayed signal from its decay products, that would allow for an efficient rejection of the background from atmospheric muon neutrinos. If no event were detected in LENA in 10 years the limit for the proton lifetime would be set to $\tau_p > 4 \cdot 10^{34}\text{y}$ at 90% CL.

4.3 The JUNO detector

JUNO (*Jiangmen Underground Neutrino Observatory*) [51] is a project currently under construction in China with the main goal of determining neutrino mass hierarchy through the detection of reactor $\bar{\nu}_e$.

The data acquisition is planned to start in 2020.

4.3.1 JUNO location

The JUNO detector is presently being constructed near Kaiping in south China, at an equal distance of 52.48km from the ten reactors distributed between the power plants of Yangjiang (6 reactor cores) and Taishan (4 cores), whose combined thermal power will be 35.8GW (26.6 initially).

The Daya Bay nuclear power plant is situated 215km away from JUNO and will provide 2.8% of the total $\bar{\nu}_e$ flux.

The laboratory will be built about 460m below ground level under a 286m tall hill (for a total of $\sim 700\text{m}$ vertical overburden): this will provide a 2000m.w.e. shielding from cosmogenic background.

4.3.2 JUNO detector setup

JUNO is designed as a spherical detector in order to provide a uniform photoelectron yield, made of several concentric layers (see[52]).

A cylindrical **water pool** contains the whole detector and is equipped with ~ 1600 PMTs, serving, as for LENA, as a shielding and as a Cherenkov detector. 25% of the water pool's upper

surface is going to be covered with plastic scintillator strips (from the OPERA experiment) that provide a muon tracker.

An **inner acrylic sphere** with an inner diameter of 35.4m and a thickness of about 12 cm contains 20kt of liquid scintillator. The chosen scintillator mixture is similar to the one proposed for LENA, with LAB as a solvent and PPO and bis-MSB as solutes; it should ensure the satisfaction of mandatory requirements as a high light yield and an attenuation length greater than 20m at 430 nm.

A **stainless-steel support structure** surrounds and holds the inner sphere; a steel open truss with a 40m inner diameter would provide a ready frame for the installation of the **~17000 20" PMTs** facing the target volume. An opaque layer is placed behind the PMTs to separate the central detector from outside veto detector.

A schematic view of the layered structure of the JUNO detector is provided in fig. 4.4.

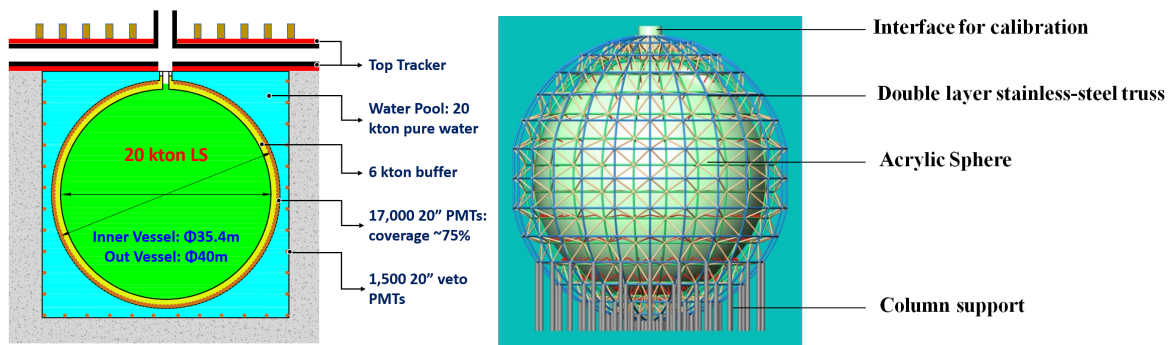


Figure 4.4: Schematic view of a vertical section of the JUNO detector (left) and of its exterior part (right) [52].

4.3.3 JUNO physics goals

The determination of neutrino mass hierarchy is the main goal of the JUNO experiment but it is accompanied by a rich physics program similar to LENA's program, including supernova and solar neutrinos, geoneutrinos and investigations on nucleon decays (for details see [51]).

Neutrino mass hierarchy The JUNO detector can measure precisely the antineutrino reactor spectrum at the medium baseline of 53km and probe the interference of two fast oscillation modes.

The observation of the spectrum of inverse beta decay events could allow the determination of $|\Delta m_{31}^2|$ and $|\Delta m_{32}^2|$ with a precision that would resolve the mass ordering.

After six years of operation, collecting 10^5 IBD events based on 36GW thermal power from the reactors, JUNO's sensitivity to neutrino mass hierarchy could reach the 3σ level. This estimate for the sensitivity assumes the expected energy resolution for JUNO of 3% at 1MeV, as well as 1% uncertainty on the energy scale (achievable with a comprehensive calibration of the detector) and a 1% uncertainty on the shape of the reactors' $\bar{\nu}_e$ spectra (see [51]).

Besides the study of reactor neutrino oscillations, JUNO could use other approaches to determine the neutrino mass hierarchy:

- Matter effects influence the long-baseline (15km to 13000km) oscillations of **atmo-**

spheric neutrinos: the *Mikheyev-Smirnov-Wolfenstein resonance* may enhance the oscillation of neutrinos in the normal mass hierarchy (NH) and the oscillation of antineutrinos in the inverted mass hierarchy (IH) [3].

- $\nu_e/\bar{\nu}_e$ appearance searches with **beam neutrinos**.

Chapter 5

Determination of sensitivity to CP violation

This chapter describes the procedure to determine the sensitivity of the LENA and JUNO detectors to CP violation for a given configuration of the neutrino beam setup at a chosen baseline.

The first section focuses on the simulation of a neutrino beam setup while the second section explains how to calculate sensitivity to CP violation considering the detectors' properties and the simulated muon neutrino and antineutrino fluxes.

5.1 Neutrino beam simulation

The setups considered in this study for the production of a conventional neutrino beam were simulated using the Monte Carlo toolkit **Geant4** (version 4.9.4, see [53, 54]) and the **ROOT** framework for the output storage [55].

5.1.1 Beam setup

The general composition and features of the beam production apparatus follow the scheme illustrated in chapter 3. The **Geant4** toolkit is used to simulate the interaction of primary protons on the target, the production of secondary particles, their focusing in the beam direction and their decay in the end tunnel (see Figure 5.1).

The details of the proton drivers and the end beam dump and muon monitors do not influence the resulting neutrino flux and are neglected in the simulations presented here.

Many parameters of the setup are optimized in order to produce the neutrino flux that would give the best sensitivity to CP violation (see chapter 6). A comprehensive summary of the main beam parameters is given in Table 5.1.

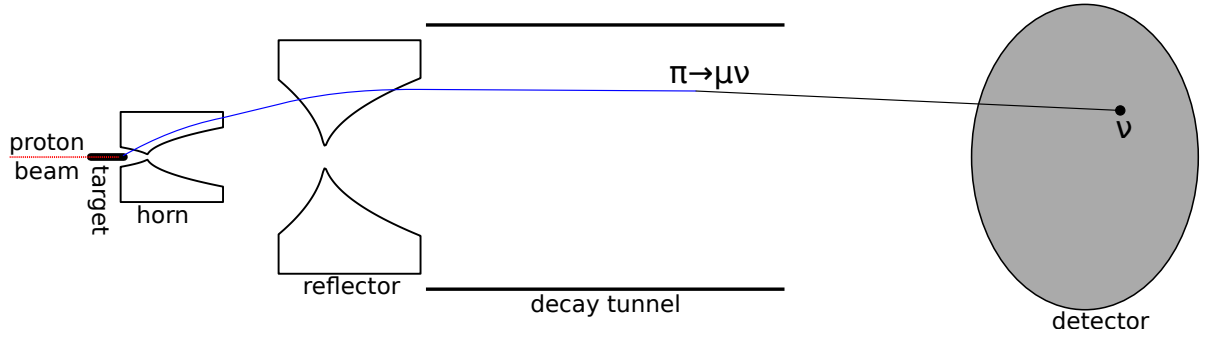


Figure 5.1: The picture illustrates the basic components of the apparatus for the production of a neutrino beam.

Proton energy	0.5-70GeV
Beam power	0.2-5MW
Target shape	solid cylinder
Target material	Aluminium, Beryllium, Graphite, Iron, Mercury, Molybdenum, Tungsten, Zirconium
Target diameter	1-10mm
Target length	20-200cm
Target position	-50/+50cm
Horn 1 shape	parabolic
Horn 1 current	0-350 kA
Horn 2 shape	parabolic
Horn 2 current	0-350 kA
Decay tunnel filling	air at 0.001238atm
Decay tunnel shape	cylinder
Decay tunnel radius	50-500cm
Decay tunnel length	10-500m

Table 5.1: Neutrino beam setup parameters.

The target position refers to the distance between the upstream edges of the target and of the first horn.

Proton beam

The two main parameters considered in this study with respect to the first element of the setup are the **beam power** and the **kinetic energy of the protons**. These two parameters are related by the number of *protons on target* per year (p.o.t./y):

$$N(\text{p.o.t.})/y = \frac{P}{E_p}, \quad (5.1)$$

where P is the beam power and E_p is the proton kinetic energy; with the range boundaries given in Table 5.1 the number of simulated p.o.t./y spans an interval from $\sim 10^{20}$ to $\sim 10^{32}$. The number of simulated proton events is, for limitations due to computing time, usually much smaller, of the order of 10^4 , with the resulting flux being scaled to the number of desired p.o.t./y.

The upper limit of 5MW for the beam power was chosen according to current design and plans for the *European Spallation Source* (ESS, [35]).

Important construction and operation parameters for the proton driver, such as pulse length and pulse rate, do not influence the result in terms of neutrino flux and are therefore not considered in this simulation.

Proton target

The setup geometry simulated in this study includes one solid proton target in the shape of a cylinder, as in the T2K experiment [17], though other configurations with multiple targets have been proposed and are perhaps better suited to withstand the stress and heat coming with high beam power [36].

Optimizable parameters in this work's configuration are the target's diameter, its length and its material, as well as the target's position d with respect to the first horn (see Figure 5.2).

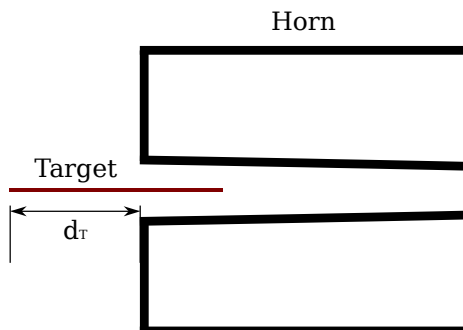


Figure 5.2: Illustration of the possible relative distance between the target and the first focusing horn.

The materials used for the simulation of the target in this study are listed in table 5.2; only pure elements were considered for simplicity. Even though low- Z materials are usually preferred as targets for neutrino beams, some elements with higher atomic number are studied in these simulations to explore the effects of high values for the atomic masses and densities.

Material	Symbol	Z	a (g/mol)	ρ (g cm^{-3})	Nuclear int. length (cm)
Beryllium	Be	4	9.01	1.85	42.1
Graphite	C	6	12.01	2.26	38.83
Aluminium	Al	13	26.98	2.7	39.7
Iron	Fe	26	55.85	7.874	16.77
Zirconium	Zr	40	91.22	6.511	23.58
Molybdenum	Mo	42	95.95	10.28	15.25
Tungsten	W	74	183.84	19.25	9.946
Mercury	Hg	80	200.59	13.54	14.58

Table 5.2: Materials considered in this study for the optimization of the target. Z is the atomic number, a the atomic mass and ρ the density. The properties of the materials are taken from [3] and [56].

Focusing system

The focusing system in the setup presented here is made of two magnetic horns - or, better, a *horn* and a *reflector*. The reflector is needed to focus the secondary particles that are not focused or underfocused by the first horn (see chapter 3).

In this study the material of the conductors for both horns is Aluminium, while the parabolic shapes, sizes and positions of the two horns, as well as their relative distance, are not optimized but kept fixed in the same configuration as in [40], illustrated in Figure 5.3. Each current circulating in the horns is an open parameter changing in each configuration, varying in a range from 100kA to 350kA; the lower limit is lowered to 0A for the optimization of the JUNO beam, because of the lower proton energy needed.

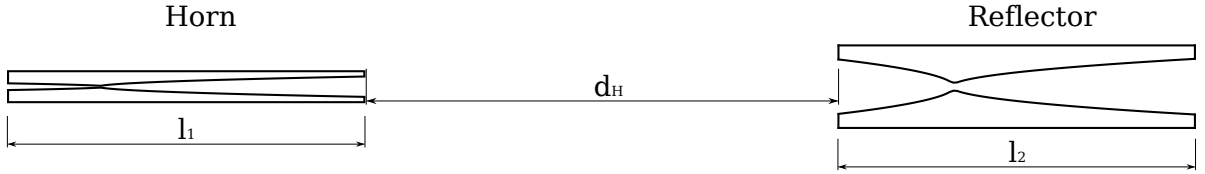


Figure 5.3: The focusing system used in this study, made by two parabolic horns. The horns have a length $l_1 = l_2 = 2.97m$, while the distance between them is $d_H = 4m$.

Decay tunnel

Taking into account the considerations in chapter 3, the decay pipe simulated in this work is a cylinder with length ranging from 100m to 500m, diameter range from 50 cm to 5 m and contains air at the very low pressure of 0.001238atm.

5.1.2 Determination of the neutrino flux

The simulation considers three sources for neutrino production from secondary particles and calculates the corresponding probabilities for the neutrinos to reach a far detector, that is then used as a weight factor for the neutrino energy spectrum (see [36]).

- Two-body decay of a charged pion or kaon

$$\pi^+, K^+ \rightarrow l^+ \nu_l$$

$$\pi^-, K^- \rightarrow l^- \bar{\nu}_l$$

where $l = e, \mu$ The probability for a decay neutrino to be emitted through a surface A at a distance L is described in 5.2:

$$P_2 = \frac{A}{4\pi L^2} \frac{1 - \beta^2}{(\beta \cos \alpha - 1)^2} \quad (5.2)$$

where β is a relativistic factor of the parent particle and α is the emission angle with respect to the beam axis. Equation 5.2 works when considering the decay region as point-like from the detector distance.

- **Muon decay**

$$\begin{aligned}\mu^+ &\rightarrow e^+ \nu_e \bar{\nu}_\mu \\ \mu^- &\rightarrow e^- \bar{\nu}_e \nu_\mu\end{aligned}$$

The probability for neutrinos from μ decays to be emitted in a direction parallel to the beam axis depends on their energy, so that

$$\frac{dP}{dE_\nu} = \frac{2(f_0 \mp \Pi_\mu^L f_1 \cos \theta^*)}{m_\mu \gamma_\mu (1 + \beta_\mu \cos \theta^*)} \cdot P_2(\mu) \quad (5.3)$$

In Equation 5.3 we define:

$$\begin{aligned}f_0(\bar{\nu}_\mu) &= 2x^2(3 - 2x) \\ f_1(\bar{\nu}_\mu) &= 2x^2(1 - 2x) \\ f_0(\nu_e) &= f_1(\nu_e) = 12x^2(1 - x)\end{aligned}$$

with $x = 2E_\nu^*/m_\mu$, where E_ν^* is the neutrino energy in the muon's rest frame; θ^* is the angle between the muon's direction and the neutrino's direction, while Π_μ^L is the muon longitudinal polarization:

$$\Pi_\mu^L = \sqrt{1 - \left(\frac{\gamma_p \beta_p}{\gamma_\mu \beta_\mu} \sin \theta_\mu^* \right)^2}.$$

Here θ_μ^* is the angle between the muon and the beam axis in the rest frame of the parent particle ($p = \pi, K$). The sign in front of Π_μ^L is - for μ^+ decays and + for μ^- decays.

The differential probability is integrated sampling the neutrino energy in bins of 1MeV width.

To compute the number of neutrinos obtained from muon decays, each produced muon is weighted with its decay probability in the decay tunnel length.

- **Three-body decay of kaons**

$$K \rightarrow \pi l \nu_l$$

with $l = \mu, e$ and $K = K^\pm, K^0$. In this case the probability to reach a detector is

$$\frac{dP}{dE_\nu} = \frac{2f(E_\nu^*)}{(m_K - m_\pi - m_l) \gamma_K (1 + \beta_K \cos \theta^*)} \cdot P_2(K) \quad (5.4)$$

In Equation 5.4 θ^* is the angle between the directions of the neutrino and the kaon in the latter's rest frame, while $f(E_\nu^*)$ is a parametrization of the neutrino energy distribution in the kaon's rest frame.

In this case the differential probability is integrated in neutrino energy through 200 sampling points.

5.1.3 Test simulation

To ensure the correctness of the beam simulation with **Geant4** and the reliability of the resulting neutrino fluxes, a comparison was made with the neutrino fluxes produced by a simulation of a neutrino beam from the accelerator complex at the Institute for *High Energy Physics (IHEP)* in Protvino, Russia.

This facility, consisting in four accelerators connected in a cascade, hosts many physics studies, e.g. research on rare kaon decays and hadron spectroscopy and produces a 70GeV proton beam. The accelerator at IHEP is situated at a 1160Km distance from the Pyhäsalmi mine and has been considered for a complementary neutrino beam in addition from a beam from CERN to Pyhäsalmi in the LBNO studies [57].

The beam setup configuration used to simulate the Protvino beam is taken from [57] and it is summarized in Table 5.3.

Proton energy	70GeV
Beam power	450kW
Target shape	solid cylinder
Target material	Graphite
Target diameter	4mm
Target length	100cm
Target position	-30cm
Horn 1 shape	parabolic
Horn 1 current	250 kA
Horn 2 shape	parabolic
Horn 2 current	250 kA
Decay tunnel filling	low-pressure air
Decay tunnel shape	cylinder
Decay tunnel radius	150cm
Decay tunnel length	400m

Table 5.3: Setup parameters used in the IHEP neutrino beam simulation (see [57]).

Figure 5.5 shows a comparison between the simulation of neutrino fluxes from IHEP made with the code used in this study and the simulated neutrino fluxes published in [57], renormalized to a 100km distance on a $100m^2$ surface and 200MeV binning. The green line is the average spectrum obtained from 38 simulations of 10^5 events, while the red lines that enclose it represent the range of the 38 simulations.

The differences between the neutrino fluxes simulated in [57] and those simulated in this work may be due to a non perfect matching of simulation parameters, e.g. the usage of a different hadronic model or different specification of the properties of the target material. Especially for the contamination components of the beam, discrepancies might also have a statistical contribution because of a low number of simulated events.

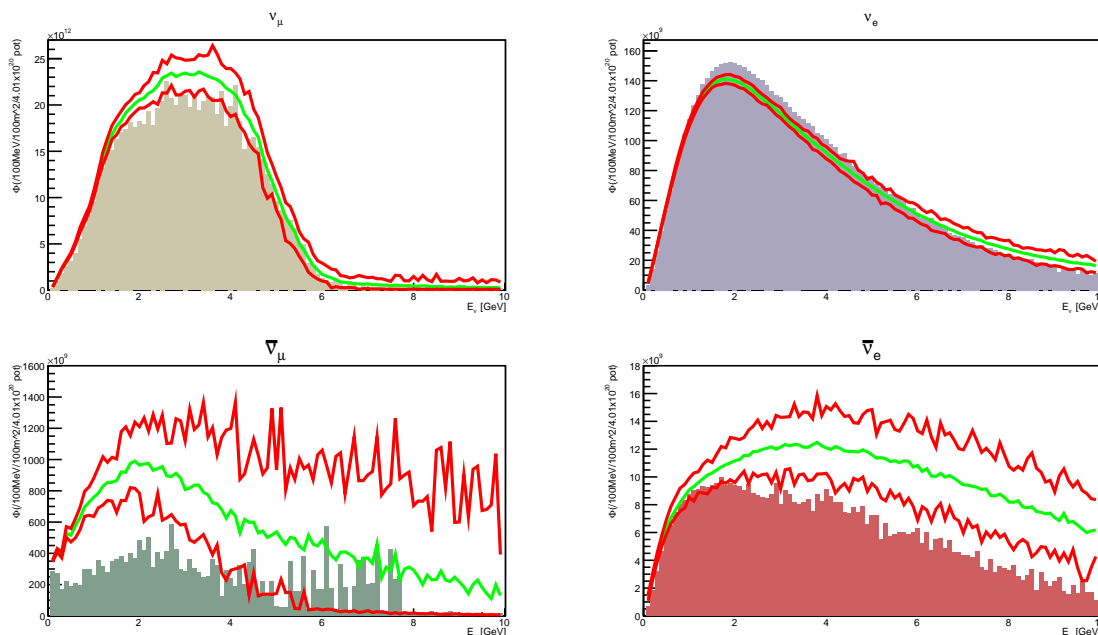


Figure 5.4: Comparison between simulations of neutrino fluxes from a IHEP beam with positive focusing mode. See also Figure 5.5

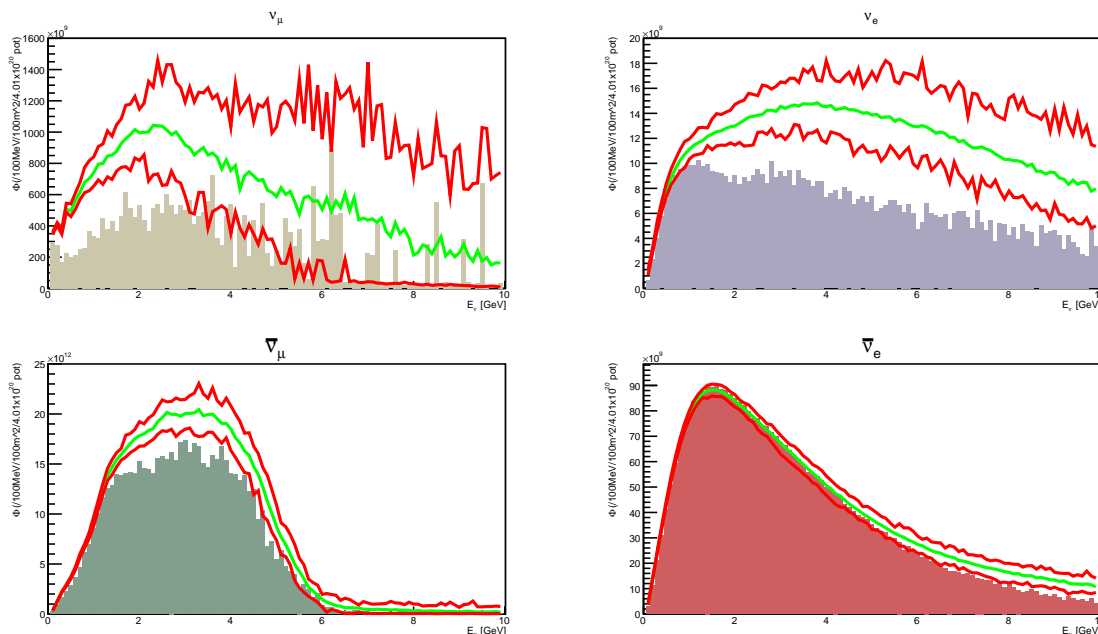


Figure 5.5: Comparison between simulations of neutrino fluxes from a IHEP beam with negative focusing mode. The histograms with coloured background are renormalized from [57], the green line is the average from 38 test simulations of 10^5 events performed with the code used in this work. The range of the test simulations is enclosed between the red lines.

5.2 Determination of sensitivity to CP violation

Once the `Geant4` simulation provides the neutrino fluxes from the chosen beam setup configuration they can be used as input signal and backgrounds in the detector to calculate its sensitivity to CP violation.

As explained in chapter 2, sensitivity to CP violation in neutrino oscillation derives from the difference in oscillation probabilities for $\nu_\mu \rightarrow \nu_e$ and $\bar{\nu}_\mu \rightarrow \bar{\nu}_e$.

The oscillation study in the three-flavour frame is performed with the `GLOBES` package (*General Long Baseline Experiment Simulator*, [58, 59]).

Given a set of “true” oscillation parameters and information on the detector’s properties and efficiencies (see following sections), `GLOBES` computes the expected event rates (e.g. for ν_e appearance and its backgrounds) for this set; it then calculates the event rates for a set of *test* oscillation parameters and fits the result to the event rates for the true values, calculating the goodness-of-fit as a χ^2 function.

The χ^2 that `GLOBES` minimizes in the parameters fit is described in Equation 5.5:

$$\chi^2 = \chi_{app}^2 + \chi_{dis}^2 + \chi_{sys}^2 \quad (5.5)$$

where χ_{app}^2 derives from the search for ν_e and $\bar{\nu}_e$ appearance, χ_{dis}^2 from the disappearance of ν_μ and $\bar{\nu}_\mu$ and χ_{sys}^2 comes from constraints on the oscillation parameters and systematics.

The minimization of χ^2 is performed with respect to all non-fixed oscillation parameters (all but δ_{CP}), the global mass density scaling and the systematic parameters.

χ_{app}^2 is defined as in Equation 5.6 from logarithmic likelihood:

$$\begin{aligned} \chi_{app}^2 &\equiv -2\ln\lambda(\mathbf{o}_{test}) \\ &= 2 \sum_{PF/NF} \sum_{E_{rec}} \left[n_e(E_{rec}; \mathbf{o}_{test}, \mathbf{f}_{test}) - n_e(E_{rec}; \mathbf{o}_{true}, \mathbf{f}_{true}) \right. \\ &\quad \left. + n_e(E_{rec}; \mathbf{o}_{true}, \mathbf{f}_{true}) \ln \frac{n_e(E_{rec}; \mathbf{o}_{true}, \mathbf{f}_{true})}{n_e(E_{rec}; \mathbf{o}_{test}, \mathbf{f}_{test})} \right]. \end{aligned} \quad (5.6)$$

n_e is the total number of electron-like events (see below).

The first sum in Equation 5.6 runs over the different polarities of the beam: positive polarity or positive focusing (PF) produces a muon-neutrino beam, while negative focusing (NF), obtained inverting the currents circulating in the horns, produces a beam with muon antineutrinos as the main component. The second sum runs over the reconstructed energy bins in the chosen analysis energy window.

The expression for χ_{dis}^2 is similar to Equation 5.6 but n_e is replaced by n_μ , the number of muon-like events.

χ_{sys}^2 is given in Equation 5.7 by summing Gaussian penalties to the fit with the *pull method*:

$$\chi_{sys}^2 = \sum_i \frac{(\mathbf{o}_{0,i} - \mathbf{o}_i)^2}{\sigma_{\mathbf{o}_i}^2} + \sum_j \frac{(1 - \mathbf{f}_j)^2}{\sigma_{\mathbf{f}_j}^2}. \quad (5.7)$$

The first term refers to the oscillation parameters with their *prior* values $\mathbf{o}_{0,i}$ and their uncertainties $\sigma_{\mathbf{o}_i}$.

The second term in Equation 5.7 is relative to the systematic parameters f_j . The systematic uncertainties are the uncertainties deriving from a not precise knowledge of all the parameters discussed above, e.g. neutrino fluxes and cross sections.

In this work the systematic uncertainties are considered as bin-to-bin correlated errors in the energy spectra, so they do not influence the shape of the spectra but only their normalization; they are considered uncorrelated between the single appearance and disappearance searches, so that:

$$n_e(E_{rec}; \mathbf{o}, \mathbf{f}) = f_{sig} n_{e,sig}(E_{rec}; \mathbf{o}) + f_{bkg} n_{e,bkg}(E_{rec}; \mathbf{o}). \quad (5.8)$$

The same formula applies to the number of muon-like events n_μ . $n_{e,sig}$ is the number of accepted signal events.

The values for the systematic parameters are given in Table 5.4 and are taken from [60].

Name	Parameter	Central value	Relative error
Signal normalization	f_{sig}	1	$\pm 5\%$
Background normalization	f_{bkg}	1	$\pm 10\%$

Table 5.4: Values and 1σ errors for the systematic parameters.

The sensitivity of the experiment to CP violation is given by the test statistics S :

$$S = \Delta\chi^2 = \chi_{0,\pi}^2 - \chi_{best}^2, \quad (5.9)$$

where $\chi_{0,\pi}^2$ is the minimized χ^2 for δ_{CP} fixed at a value $\delta_{CP} = 0, \pi$ and χ_{best}^2 is the global minimum χ^2 when the test value of δ_{CP} can vary over the whole range.

5.2.1 Asimov data sets and Monte Carlo simulations

In this study it was assumed that the test statistics $S = \Delta\chi^2$ has a χ^2 *distribution with one degree of freedom* and the sensitivity to CP violation was calculated on one simulation of a given experimental configuration (beam and detector's properties), considered as an *Asimov data set*, representative of the outcome of the experiment.

This procedure follows the established method for the determination of experimental sensitivities (see also [57]).

It was discussed in [61] that this assumption only holds if the experiment has a good sensitivity to CP violation, because the cyclic nature of the variable δ_{CP} violates the premises of Wilk's theorem, on which the assumption is based.

In order to find the real distribution of the test statistics and evaluate the experiment's sensitivity correctly, the same experiment should be simulated a large number of times (many realizations of the experiment), calculating the test statistics S for each realization.

CP conservation is rejected at confidence level (CL) x if the measured value of S is among the

$1 - x$ fraction of largest values in the distribution of S . A critical value $S_c(x)$ is defined such that CP conservation is rejected at CL x if $S > S_c(x)$. By construction, $S_c(x)$ is the inverse of the cumulative distribution function (CDF) of S under the CP conserving hypothesis.

The expected sensitivity of an experiment that does not have data yet is defined as the CL obtained for the median of the distribution (*median sensitivity*) and is typically shown as a function of the value of δ_{CP} (*median sensitivity*).

The median sensitivity does not necessarily coincide with the significance computed with the Asimov data set, but the differences resulting from these two definitions are neglected in this work.

5.2.2 Neutrino oscillation and density parameters

The values used here for the *true* neutrino oscillation parameters are obtained from the values in Table 2.1 for normal mass hierarchy.

Since matter effects are also taken into account in GLOBES oscillation analysis, matter density and the corresponding uncertainty constitute a prior involved in Equation 5.7. Here a constant matter density was used along the baseline, equal to the average matter density from the PREM onion shell model of the earth [62, 63].

5.2.3 Detector mass and baseline

The first detector parameters to be taken into account in the oscillation analysis are its target mass and the baseline, i.e. the distance between the neutrino source and the detector.

Detector mass As mentioned in chapter 4, the designed detector mass for LENA is 50kt and 20kt for JUNO. It is assumed in this work that the liquid scintillator in both detectors is made of pure LAB; the molecular weight of LAB is 241g/mol, so considering a LAB molecule as a neutrino/antineutrino target we obtain $2.5 \cdot 10^{30}$ /kt target molecules. This means a total of $1.25 \cdot 10^{32}$ target molecules for LENA and $5 \cdot 10^{31}$ for JUNO.

ESS-LENA baseline The assumed origin of the neutrino beam to LENA in this work is the *European Spallation Source (ESS)*, [35] in Lund, Sweden, at a distance of 1134km from the proposed site for LENA in Pyhäsalmi.

The European Spallation Source is a multi-disciplinary research facility currently under construction based on a powerful neutron source. It is planned to be fully operational in 2025 and will allow research in life science topics, materials science, physics and chemistry.

ESS will be equipped with a proton linear accelerator, providing a 2GeV proton beam at 5MW by 2022. This configuration was the basis of this work; the results of the optimization of a neutrino beam from the planned ESS accelerator to LENA and the corresponding sensitivity to CP violation are shown in chapter 7.

CSNS-JUNO baseline The facility considered in this study as a possible source for a neutrino beam to JUNO is the *China Spallation Neutron Source (CSNS)*, [64], operated by

the *Institute of High Energy Physics*. This structure is, like ESS, an accelerator-based neutron source, currently under construction in Dongguan, in the Guangdong province, 150km from the JUNO location.

The main accelerator in CSNS will have at first a beam power of 120kW in the first phase (*CSNS-I*) and of 240kW in a second phase (*CSNS-II*), with the potential for further upgrade to 500kW [65]. The detector mass and baseline parameters for LENA and for JUNO are summarized in Table 5.5.

	detector mass (kton)	target molecules	baseline (km)
LENA	50	$1.25 \cdot 10^{32}$	1134
JUNO	20	$5 \cdot 10^{31}$	150

Table 5.5: Detector mass and baseline of the neutrino beam for LENA and JUNO.

Another important parameter for the oscillation analysis is the experiment's **running time** (in years) for both the positive focusing and the negative focusing modes; while the total running time is set to 10 years for both LENA and JUNO, the time allocation for PF and NF is a variable in the optimization procedure (see chapter 6).

5.2.4 Cross-sections

In both studies of LENA and JUNO detection, the used neutrino and antineutrino cross-sections for CC and NC interactions on LAB molecules ($C_{18}H_{30}$) are taken from [60] and shown in Figure 5.6.

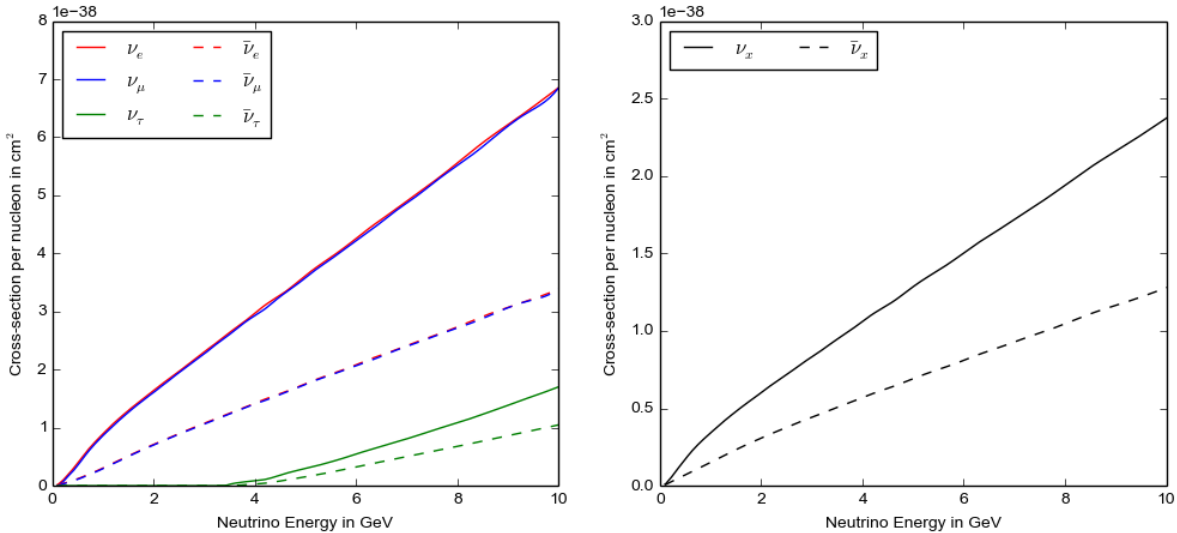


Figure 5.6: Neutrino and antineutrino cross-sections per nucleon for charged-current interactions (left) and neutral-current interactions (right) on a LAB molecule ($C_{18}H_{30}$) from [60].

5.2.5 Energy reconstruction

Event reconstruction based on the photoelectron distribution at the PMTs does not allow to determine the *true* energy of the incoming neutrino but an estimate E_{rec} , given by the sum of the estimate for the *visible* energy E_{vis} and the estimate for the leakage E_{inv} ; when it is not possible to recover the missing energy $E_{rec} \equiv E_{vis}$ is assumed.

The reconstructed energy E_{rec} enters the neutrino oscillation analysis and it is determined through so-called *energy migration matrices*, tabulating the probability distribution $P(E_{rec}|E_{true})$ as a function of the true energy of the neutrino.

Energy migration matrices for LENA The energy migration matrices for the LENA detector used in this study are shown in Figure 5.7. They are taken from [66] and were compiled following a simulation of the detector, assuming no recovery of missing energy. The binning is not uniform throughout the 0-10GeV but is 0.2GeV for energies below 5GeV and 0.5GeV for higher energies to take into account the deterioration on energy resolution with energy.

The $\nu_\mu - CC$ matrix was built considering only events having the primary muon fully contained in the active volume of the detector.

The loss of statistics due to the rejection of not contained events is taken into account in the GLOBES analysis through the use of energy-dependent containment efficiencies as *pre-smearing efficiencies* from [60].

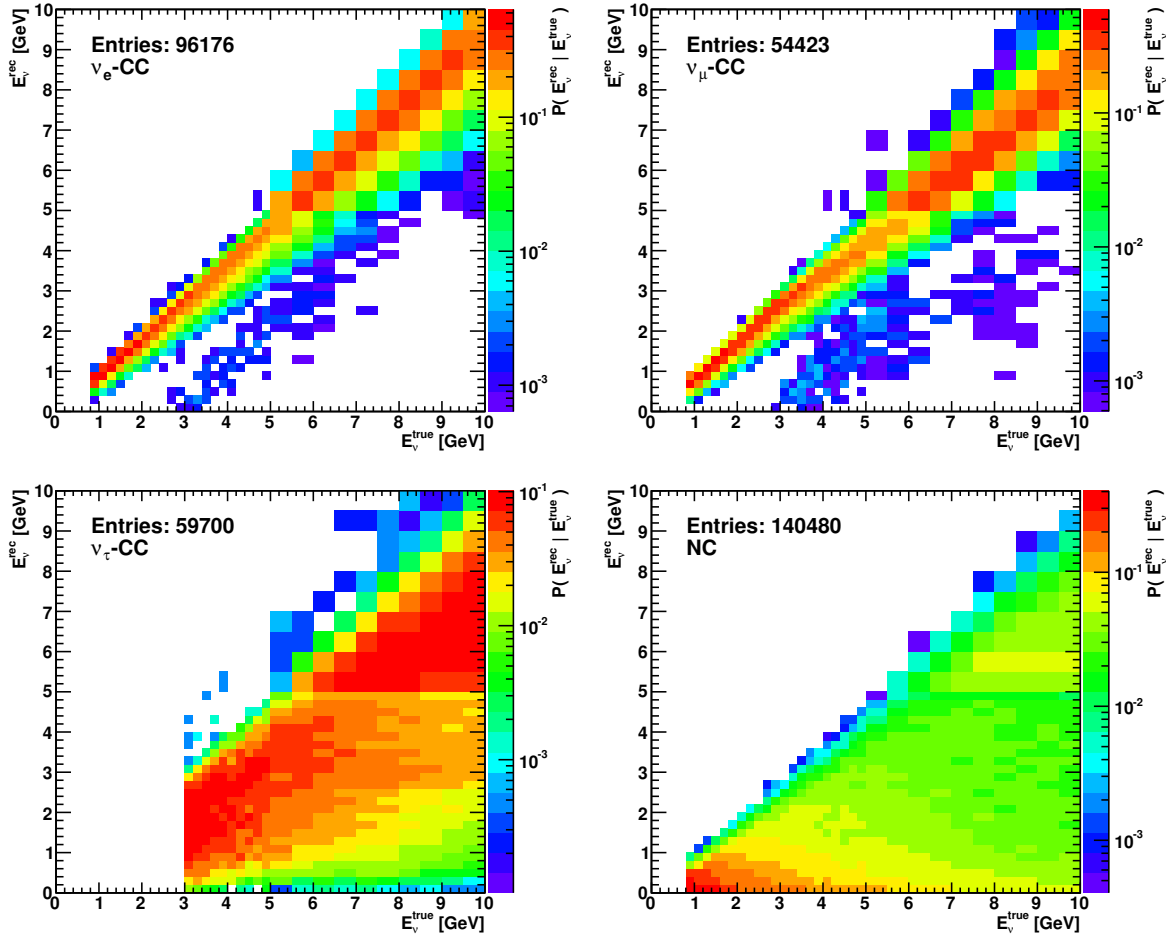


Figure 5.7: Energy migration matrices for LENA from [66]. They are obtained from the simulation of fully contained events.

Energy migration matrices for JUNO The energy migration matrices for JUNO, shown in Figure 5.8 are obtained from a detector simulation presented in [67].

They do not consider the containment of the neutrino events in the detector so no pre-smearing efficiencies were applied. As for the migration matrices for LENA, the binning is not uniform but roughly follows the deterioration of the energy resolution with increasing energy: the bin width is 25MeV for $E_{\text{true}} \leq 1\text{GeV}$, 50MeV for $1\text{GeV} < E_{\text{true}} \leq 2\text{GeV}$, 150MeV for $2\text{GeV} < E_{\text{true}} \leq 5\text{GeV}$ and finally 250MeV for $E_{\text{true}} > 5\text{GeV}$.

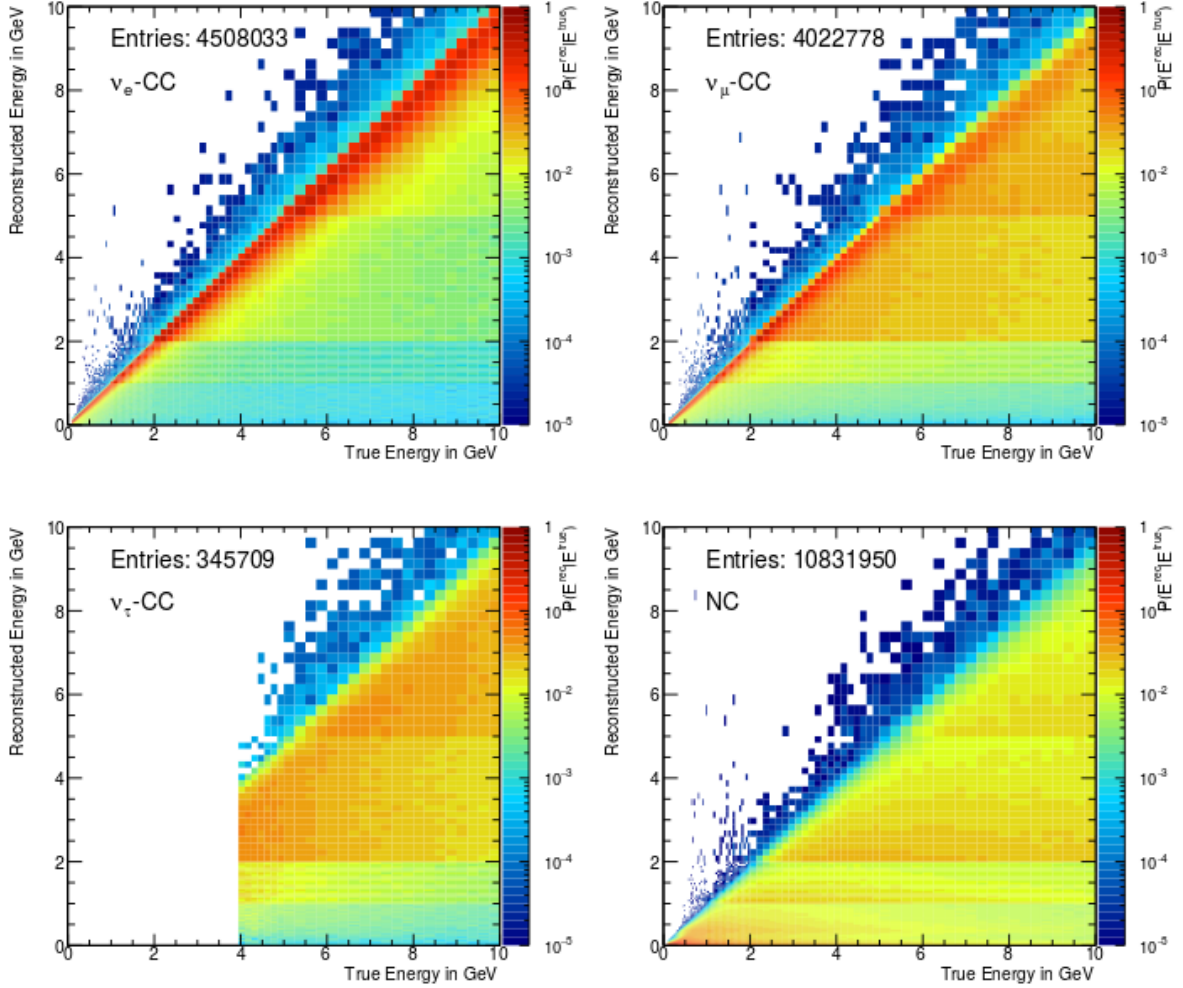


Figure 5.8: Energy migration matrices for JUNO adapted from [67].

The analysis energy windows were set to $[0.01-7]\text{GeV}$ for LENA and $[0.1-5]\text{GeV}$ for JUNO.

5.2.6 Signal and background channels and efficiencies

As explained in chapter 2, CP violation is investigated through the *appearance search* of ν_e ($\bar{\nu}_e$) in the oscillation $\nu_\mu \rightarrow \nu_e$ ($\bar{\nu}_\mu \rightarrow \bar{\nu}_e$) of muon (anti-)neutrinos from a conventional neutrino beam.

The appearance of ν_e ($\bar{\nu}_e$) and the *disappearance* of ν_μ ($\bar{\nu}_\mu$), which allows to constrain the oscillation parameters in the fit, are called **rules** in the GLOBES AEDL language; the signal and background contributions to these rules are called **channels**.

For each channel a *selection efficiency* ϵ is defined as the fraction of events that enter the oscillation analysis. The same values are used in this work for the selection efficiencies of LENA and JUNO; they follow the assumptions and investigations in [60] for the LENA detector and could improve with the improvement of topological reconstruction techniques. The present analysis considers only beam-related backgrounds and takes into account the detector's inability to distinguish a lepton from its corresponding antilepton.

ν_e ($\bar{\nu}_e$) appearance The wanted signal for this rule is a so-called *e-like* event, defined by the electromagnetic shower generated by the outgoing $e^-(e^+)$ in a ν_e ($\bar{\nu}_e$) charged current interaction.

The backgrounds for this channel, which produce a similar signature, are:

- $\nu_e \rightarrow \nu_e$, $\bar{\nu}_e \rightarrow \bar{\nu}_e$: intrinsic beam contamination with electron neutrinos and electron antineutrinos.
- Neutrino and antineutrino neutral-current interactions: they can mimic an e-like event, for example with the production of a π^0 .
- $\bar{\nu}_e$ (ν_e) events from oscillation during PF (NF) beam mode.
- Misidentified muons.
- ν_τ and $\bar{\nu}_\tau$ charged-current interactions with τ^\pm decay into e^\pm or hadrons.

We have from [3]:

$\tau^- \rightarrow e^- + \bar{\nu}_e + \nu_\tau$ ($\tau^- \rightarrow e^+ + \nu_e + \bar{\nu}_\tau$) (electronic decay): *branching ratio* (BR) $\sim 17.8\%$

$\tau^- \rightarrow \nu_\tau + \text{hadrons}$ ($\tau^+ \rightarrow \bar{\nu}_\tau + \text{hadrons}$) (hadronic decay): BR $\sim 64.8\%$.

It is assumed here that electronic decays produce e-like events and hadronic decays produce NC-like events.

ν_μ ($\bar{\nu}_\mu$) disappearance The signal signature for this rule is given by the long track of a muon or antimuon produced by a ν_μ ($\bar{\nu}_\mu$) charged-current interaction (*μ -like* event).

The events that constitute background for this disappearance search are:

- Neutrino and antineutrino neutral-current interactions that can mimic a μ -like event.
- $\bar{\nu}_\mu$ (ν_μ) from beam contamination in PF (NF) mode.
- ν_τ and $\bar{\nu}_\tau$ charged-current interactions with production of μ^\pm (branching ratio $\sim 17.4\%$, assumed to produce μ -like signatures) or hadrons.

Table 5.6 summarizes the channels involved in this oscillation analysis and the corresponding values of the selection efficiencies (multiplied by the branching ratios for the tau decays).

Rule	Channel		Selection efficiency	
ν_e appearance	signal	$\nu_\mu \rightarrow \nu_e$	$\epsilon_{CC}^{\text{app}}$	0.27
	background	beam contamination	$\epsilon_{CC}^{\text{app}}$	0.27
		$\bar{\nu}_\mu \rightarrow \bar{\nu}_e$	$\epsilon_{CC}^{\text{app}}$	0.27
		neutral current	$\epsilon_{NC}^{\text{app}}$	0.11
		hadronic τ decay	$0.648 \times \epsilon_{NC}^{\text{app}}$	0.07
		electronic τ decay	$0.178 \times \epsilon_{CC}^{\text{app}}$	0.05
	misidentified μ -like events	$\epsilon_\mu^{\text{app}}$	0.01	
ν_μ disappearance	signal	$\nu_\mu \rightarrow \nu_\mu$	$\epsilon_{CC}^{\text{dis}}$	0.90
	background	$\bar{\nu}_\mu \rightarrow \bar{\nu}_\mu$	$\epsilon_{CC}^{\text{app}}$	0.90
		neutral current	$\epsilon_{NC}^{\text{dis}}$	0.10
		hadronic τ decay	$0.648 \times \epsilon_{NC}^{\text{dis}}$	0.06
		muonic τ decay	$0.178 \times \epsilon_{CC}^{\text{dis}}$	0.16

Table 5.6: Selection efficiencies for the ν_e appearance and ν_μ disappearance channels and backgrounds from [60]. Efficiencies for $\bar{\nu}_e$ appearance and $\bar{\nu}_\mu$ disappearance are obtained by interchanging neutrinos and antineutrinos.

Chapter 6

Genetic Algorithm

6.1 Introduction

Genetic algorithms (GA) are methods used to solve optimization problems by mimicking the processes leading to biological evolution, namely *natural selection*, *mutation* and *recombination of the genes*.

The main principles of genetic algorithms were first described by Holland in 1975 [68] but the techniques and operators used to implement them are still subject of ongoing research and there is no universal consensus over the best and most effective practices [69].

In this study an implementation of genetic algorithm has been used to find the beam setup leading to the highest sensitivity of the LENA and JUNO detectors to CP violation. This algorithm was chosen for this study because of the multitude of optimization parameters and their manifold correlations.

Each candidate solution to the problem represents an *individual* and has a unique string of values (*chromosome*) for the considered parameters (*genes*); the *fitness* of the individuals is the value to be optimized and is evaluated simultaneously for a *population* of N individuals.

The first *generation* is composed of randomly generated individuals; their fitness is evaluated and three main operators are applied to produce *offspring* and obtain a new generation:

selection: the individuals that will pass their genes to the next generation are selected, with a probability proportional to their fitness;

crossover: it is the operator corresponding to the natural recombination of genes from *parents* in reproduction;

mutation: casual alteration of one of more genes in the offspring individuals within their range of variation.

By iterating this procedure, illustrated in Fig. 6.1, the population of individuals should be able to evolve generation by generation towards the optimal fitness: the algorithm is said to converge when the maximum fitness does not improve anymore (or improves very slowly).

The key to a successful implementation of the genetic algorithm lies in the balance between the *exploration* of the parameters space and the *exploitation* of the fittest individuals [70].

The next paragraphs will describe the definitions and the operators used in this study for the implementation of the genetic algorithm.

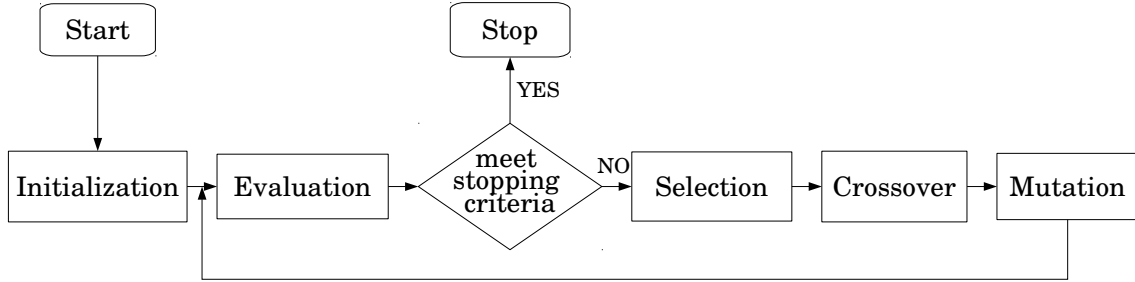


Figure 6.1: Flow chart of the genetic algorithm.

6.2 Definition of individuals

Each individual was defined by the properties described in table 6.1. For proton energy and beam power the top value refers to the algorithm applied to the LENA detector, while the bottom value refers to the GA applied to JUNO. The table 6.2 shows an example of a string representing an individual.

Parameter	Unit	Range	Step
Proton energy	$E(GeV)$	1-70	1
		0.5-20	0.1
Beam power	$P(MW)$	0.2-5	0.1
Target material	Mat_{tar}	Aluminium, Beryllium, Graphite, Iron, Mercury, Molybdenum, Tungsten, Zirconium	
Target diameter	$D_{tar}(mm)$	1-10	0.5
Target length	$L_{tar}(cm)$	20-200	1
Target position	$Pos_{tar}(cm)$	-50/+50	1
Current Horn 1	$I_1(kA)$	100-350 0-350	10
Current Horn 2	$I_2(kA)$	100-350 0-350	10
Decay tunnel radius	$R_{tun}(cm)$	50-500	10
Decay tunnel length	$L_{tun}(m)$	10-500	10
Positive focussing time	$PHF(y)$	1-9	1

Table 6.1: Parameters defining the individuals and their range of variation for LENA and JUNO

ID	Gen	E	P	Mat_{tar}	D_{tar}	L_{tar}	Pos_{tar}	I_1	I_2	R_{tun}	L_{tun}	PHF	$fitness$
3334395	3	25	4.4	Zirconium	5.5	100	1	130	230	390	360	9	0.0097

Table 6.2: Example of an individual's representation. The elements to the right of the double line are called the *genes* and constitute the *chromosome* of the individual.

Each generation was populated with 50 individuals; the first generation was created by picking for each *gene* a random value within the intervals shown in 6.1.

6.3 Fitness evaluation

To evaluate the fitness of an individual, its genes are used as parameters of a beam setup in a Monte Carlo simulation performed with the package **Geant4**. The obtained fluxes for electron- and muon- neutrinos and antineutrinos are then used as inputs in the calculation of the sensitivity to CP violation performed with **GLOBES** (see. chapter 5).

The value of the individuals' fitness function is directly depending on the $\Delta\chi^2$ as defined in chapter 5. For the optimization of the beam for LENA the definition of fitness is given by Equation 6.2.

$$T(\delta_{CP}, \Delta\chi_T^2) = \begin{cases} 1, & \text{if } \Delta\chi^2(\delta_{CP}) > \Delta\chi_T^2 \\ 0, & \text{else} \end{cases} \quad (6.1)$$

$$f(n\sigma) = f(n^2) = \frac{1}{2\pi} \int_0^{2\pi} T(\delta_{CP}, n^2) d\delta_{CP}. \quad (6.2)$$

$f(n\sigma)$ is here defined as the fraction of δ_{CP} values for which the no-CP-violation hypothesis can be excluded with a $n\sigma$ confidence level. An example of $T(\delta_{CP}, \Delta\chi_T^2)$ with $\chi_T^2 = 9$ is illustrated in Figure 6.2.

The exclusion fraction at 3σ , i.e. $f(3\sigma)$ is applied to the fitness definition for the LENA beam optimization.

Using $f(3\sigma)$ as an individual's fitness value would give a direct connection to the relevant goal of the study but would not allow to distinguish between individuals for which $f(3\sigma)$ is very small: for this reason, $f(3\sigma)$ is used as the fitness value for an individual only if it is $f(3\sigma) > 0.1$; otherwise the fitness value is defined as the maximum $\Delta\chi^2$ multiplied by 0.01, as in 6.3:

$$\text{fitness} = \mathcal{F} = \begin{cases} f(3\sigma), & \text{if } f(3\sigma) > 0.1 \\ 0.01 \cdot \Delta\chi_{\max}^2, & \text{else} \end{cases} \quad (6.3)$$

6.4 Selection method

The step following the fitness evaluation for a generation n is the selection of the individuals for reproduction, so that a new generation $n + 1$ of individuals can be created.

The selection method adopted in this work is a combination of the classical methods *truncation selection* [71] and *proportional selection* method, also known as *roulette wheel selection* [72]: all the individuals are sorted according to their fitness value; a number of individuals is then selected to generate the next population, so that their fitness values add up to 90% of the total fitness of the population (as in the truncation selection method). The reproduction rate for each selected individual is proportional to the ratio between the individual's fitness and the total fitness of the selected individuals (as in the roulette wheel selection).

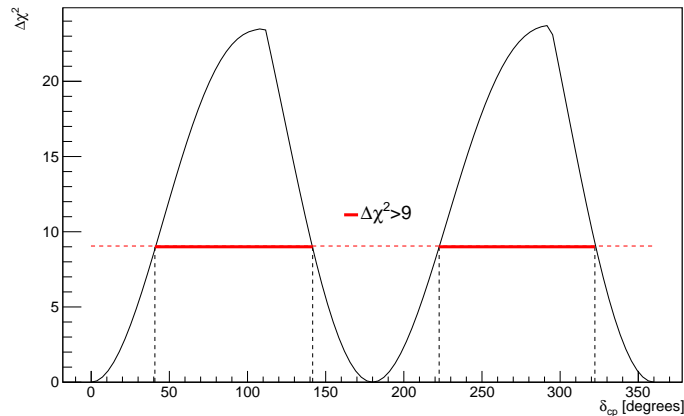


Figure 6.2: Definition of $f(3\sigma)$. The red line represents $T(\delta_{CP}, \Delta\chi_T^2)$ with $\Delta\chi_T^2 = 9$.

This selection method is illustrated in Fig. 6.3.

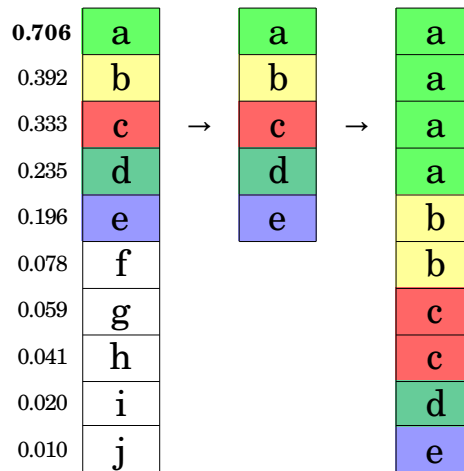


Figure 6.3: Example of selection from a 10 individuals population: individuals (letters) are sorted by fitness (numbers) and selected up to 90% of total fitness. The number of copies for each selected individuals is proportional to their weighted fitness.

In the selection process the principle of *elitism* was applied to accomplish survival of the fittest i.e. exploitation of the best individual: in each iteration the best individual of its generation was kept unchanged once in the next generation, not undergoing either crossover or mutation.

6.5 Crossover

Crossover is the operator that recombines the parents' genes to generate the offspring. In the traditional *single point crossover* two individuals are chosen as a couple of parents; a crossover point in their string of genes is chosen and their genes are swapped in the offspring from that point (see Fig. 6.4)

In this work a different approach was used: for each gene in the chromosome, the values for all

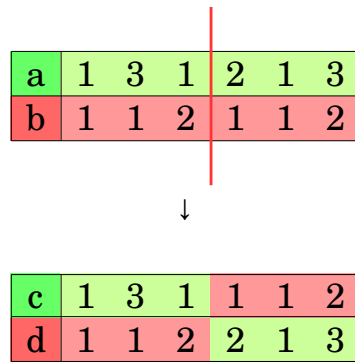


Figure 6.4: Principle of single point crossover: the individuals "a" and "b" are selected as a pair of individuals and a crossover point is chosen; the offspring individuals "c" and "d" will inherit part of their chromosome from parent "a" and the other from parent "b".

of the individuals were part of a *gene pool*, where they were shuffled and randomly reassigned to the individuals in the population (see Fig. 6.5). With increasing generation number the gene pool is more and more closely related to the most successful individuals, abiding by the exploitation principle.

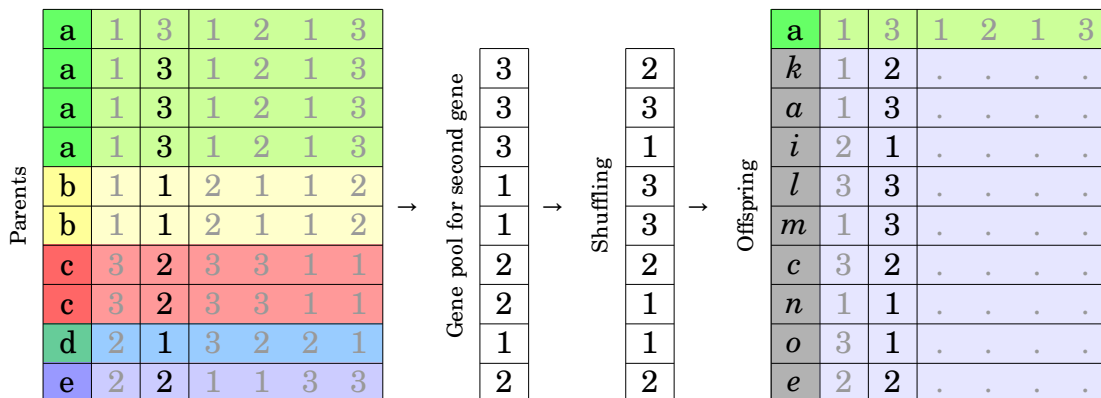


Figure 6.5: Principle of shuffling crossover. In agreement with the *elitism* principle the individual "a" is not subject to crossover. The individuals identified by an italic letter are temporary and will change with crossover and mutation.

6.6 Mutation

The *mutation* operator is used to enable exploration of the parameter space and ensure diversity in the population.

At least ten individuals in each generation were subject to the mutation of three genes.

After the crossover operation it is still possible to have some number of identical individuals in the population, from the initial replication of the best individuals of the previous generation;

in this study all the identical individuals (but one copy of the fittest, according to *elitism*) were subject to mutation; if there were less than $i < 10$ identical individuals from crossover, $10 - i$ more individuals were chosen for mutation.

All the non-identical individual to be mutated, the three mutated genes and the new values assigned to them were randomly chosen. The process of mutation is illustrated in Fig. 6.6

a	1	3	1	2	1	3
<i>k</i>	1	2	1	2	1	3
a	1	3	1	2	1	3
<i>i</i>	2	1	1	3	1	1
<i>l</i>	3	3	2	1	2	1
<i>m</i>	1	3	2	3	1	3
<i>q</i>	3	2	3	2	1	2
<i>n</i>	1	1	3	1	3	1
<i>o</i>	3	1	1	2	1	3
<i>r</i>	2	2	3	1	1	2

→

a	1	3	1	2	1	3
k	1	2	1	2	1	3
s	2	3	1	2	3	3
i	2	1	1	3	1	1
l	3	3	2	1	2	1
t	1	3	3	2	1	3
q	3	2	3	2	1	2
u	1	1	2	1	2	1
v	3	3	1	2	1	1
r	2	2	3	1	1	2

Figure 6.6: Example of mutation: The individual *a* is mutated because identical to "a". Two random genes are mutated from *a* and from the randomly chosen individuals *m*, *n*, *o*.

In the end of an iteration of the algorithm a new population was generated which, if the algorithm was successful, had a better average fitness than the previous generation, as in Figure 6.7.

	Gen n		Gen n+1	
0.706	a		u	0.799
0.392	b		t	0.750
0.333	c		a	0.704
0.235	d		l	0.427
0.196	e		k	0.383
0.078	f	→	s	0.339
0.059	g		v	0.251
0.041	h		i	0.216
0.020	i		r	0.121
0.010	j		q	0.061

Figure 6.7: A comparison is shown between the generation *n* and the generation *n+1*, obtained after one complete iteration of the algorithm through the steps shown in Figg. 6.3, 6.5, 6.6.

6.7 Behaviour of the algorithm

6.7.1 Effects of statistical fluctuations

Statistical fluctuations of the simulations conflict sometimes with the *elitism* principle: re-evaluation of the fittest individual of the previous generation could result in a worse fitness - this explains occasional setbacks in the maximum population fitness.

Figure 6.8 shows two examples of runs of GA on simulations whose outcomes have different standard deviations of the fitness (deriving for example from a different number of simulated events).

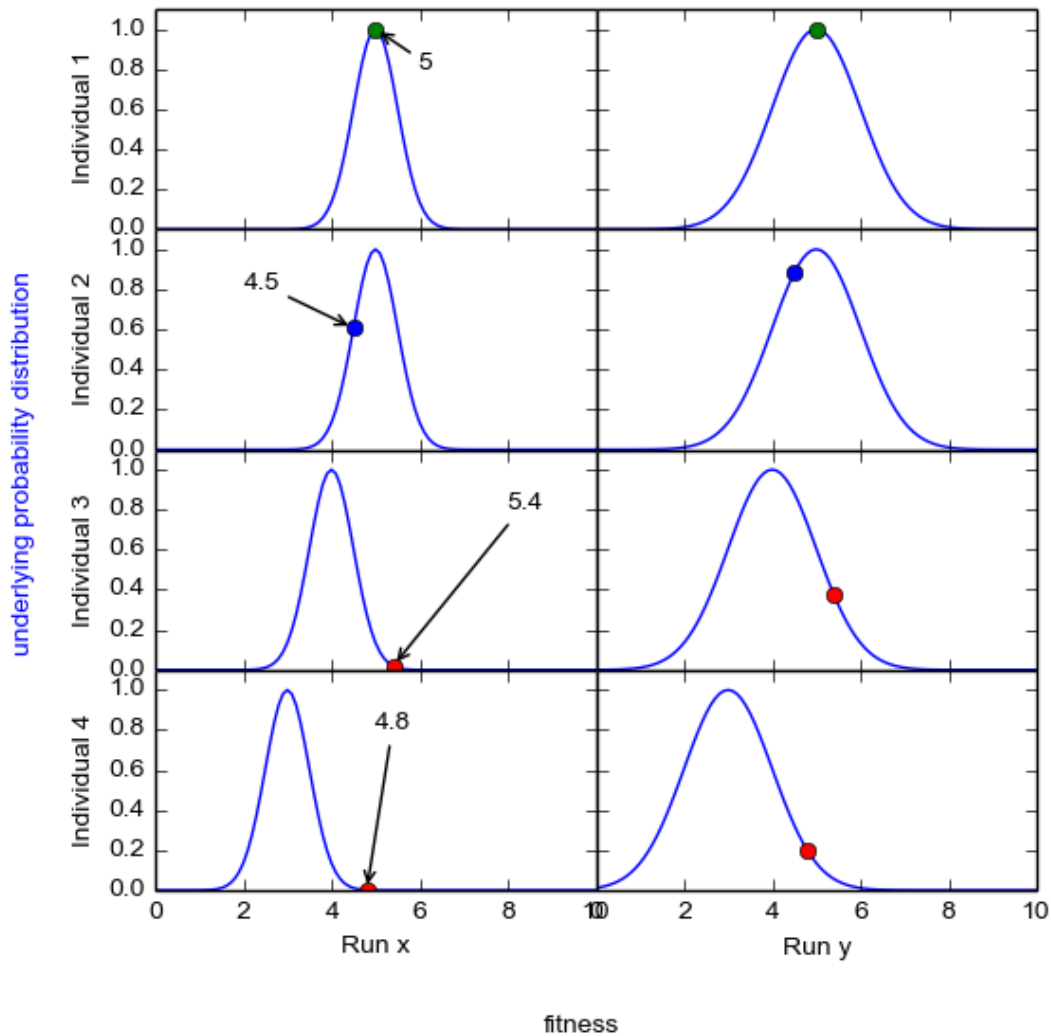


Figure 6.8: Examples of GA runs with small (Run x) and large (Run y) statistical fluctuations of the fitness.

For each run four individuals of the same generation are shown, with their actual fitness drawn from the respective probability distribution. In the Run x example, considering the mean values of the distributions, the fitness ranking would be 1 ($\langle \mathcal{F} \rangle = 5$), 2 ($\langle \mathcal{F} \rangle = 5$), 3 ($\langle \mathcal{F} \rangle = 4$), 4 ($\langle \mathcal{F} \rangle = 3$); the values drawn by the simulations, represented in the picture by the dots, lead

to the ranking 3 ($\mathcal{F} = 5.4$), 1 ($\mathcal{F} = 5.0$), 4 ($\mathcal{F} = 4.8$), 2 ($\mathcal{F} = 4.5$). In the next generation the winner, Individual 3, would be reevaluated, with a high probability of performing worse and yielding a fitness $\mathcal{F} < 5.4$.

The individuals from Run y have wider underlying fitness distributions, making larger fluctuations more probable; this causes a decrease in the algorithm's sensitivity to small fitness differences.

Since the algorithm is set to favour the highest fitness values, overperforming individuals (delivering a fitness $\mathcal{F} > \langle \mathcal{F} \rangle$) are more likely to be selected for the next generation, making GA less efficient.

Moreover, the selection of overperforming individuals leads to a bias in the winner fitness values correlated with the width of the probability distribution (see chapter 7).

6.7.2 Local optimization maxima

Despite GA being a generally effective algorithm, there is no guarantee for it to reach the true global fitness maximum: given the complexity of the parameter landscape it is not surprising for a run to dwell around a local fitness maximum, as it is not surprising for it to suddenly proceed towards the global best as a consequence of a fortunate mutation (see Figure 6.9 for an example).

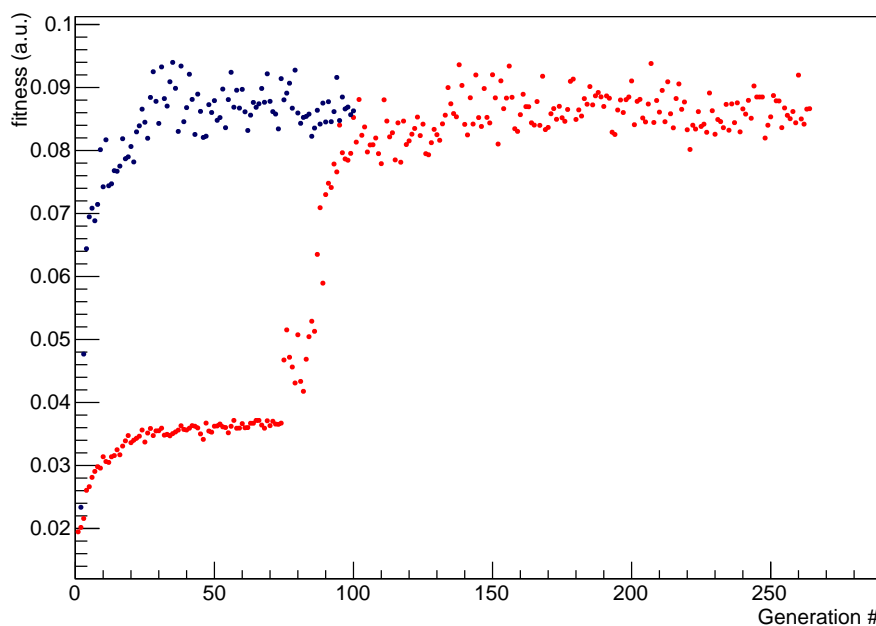


Figure 6.9: Example of GA iteration running into a local maximum: the black markers indicate the evolution of a run normally reaching the maximum fitness; the red markers belong to a run dwelling in a local maximum until a sudden mutation leads it to the best configuration.

6.8 Implementation

The simulation of the neutrino fluxes and the calculation of the sensitivity to CP violation were performed as a single process of fitness evaluation, lead simultaneously for all the individuals in a generation with parallel computing in the *Condor* [73] cluster of RWTH Physics Institute. Each individual is identified by a number obtained as the *md5* hash of the parameter string (see Table 6.2).

In order to avoid heavy slowing down of the algorithm performance due to computing time fluctuations (e.g. suspended cluster jobs), the population size was set to 50 individuals and the selection process was allowed to start when at least 48 of the individuals' fitnesses were evaluated. In this way the slowest individuals were discarded in the process, in spite of the possibility for them to be the fittest individuals in the generation.

Due to limitations of the computing time, each run of the algorithm was set to end after Generation 100; this number seemed to be sufficient in most cases to reach convergence to the maximum fitness.

Chapter 7

Results

This chapter describes the results of the search for the best neutrino beam setup configurations for CP violation studies with LENA and JUNO at the considered baselines.

7.1 Optimization of the ESS-LENA neutrino beam

The initial idea for this work was to assess LENA's sensitivity to CP violation using a neutrino beam from the ESS proton accelerator, optimizing all the parameters but proton energy and beam power, fixed by ESS design to $E_p = 2\text{GeV}$, $P = 5\text{MW}$.

The results of this optimization are shown in Figure 7.1 for two iterations of genetic algorithm.

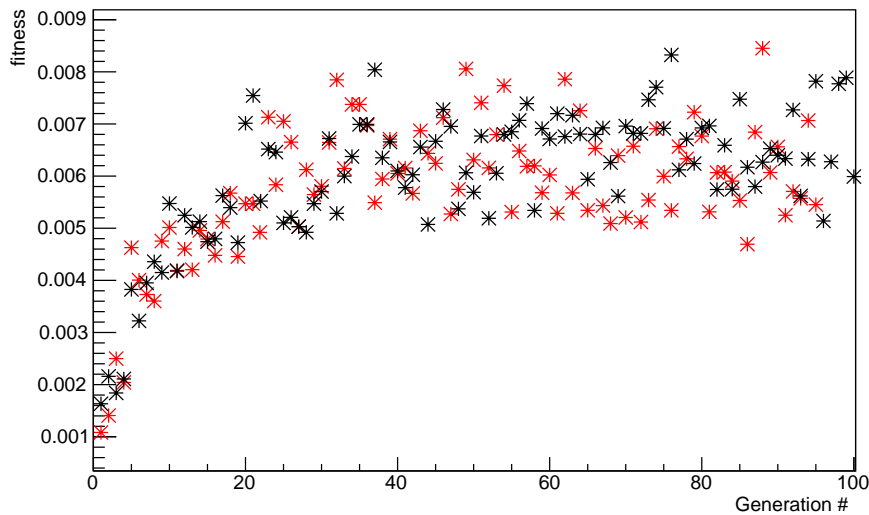


Figure 7.1: Fitness of each generation's best individual (beam configuration) for two runs of genetic algorithm for the optimization of a neutrino beam for LENA from ESS; $E_p = 2\text{GeV}$, $P = 5\text{MW}$.

The definition of fitness in this case is not the definition given in section 6.3 but it is simply given by the maximum of the test statistics: $\mathcal{F} = \max(\Delta\chi^2)$.

The extremely small values of f reached by the simulations indicate that LENA would have no

sensitivity to CP violation with a neutrino beam as the one obtained with the proton energy and beam power set by the ESS design, independently of the optimization of the other beam parameters. For this reason we have in the next step discarded the ESS beam design and tried to estimate the sensitivity to CP violation with an optimization of all the parameters, including proton energy and beam power, for the same baseline ESS-LENA (Lund-Pyhäsalmi).

7.2 Beam optimization for the LENA detector

Since genetic algorithm is not always able to find the best solution(s) but may converge on a local maximum of fitness (see chapter 6), ten iterations (runs) of the algorithm were performed, each evolving for 100 generations.

Because of limitations on computing time, the number N_{sim} of simulated events was not the same for all the runs but went from $2 \cdot 10^3$ to $2 \cdot 10^4$, as described in Table 7.1.

Run	1, 2, 3	4, 5, 6	7, 8	9, 10
N_{sim}	2000	5000	10000	20000

Table 7.1: Number of simulated events for each iteration (run) of genetic algorithm for LENA.

Figure 7.2 Shows the evolution of the beam optimization with increasing fitness values for the ten runs, while Figure 7.3 focuses on the last 30 generations of each run; the lines indicate the three runs with the lowest and the two runs with the highest number of simulated events.

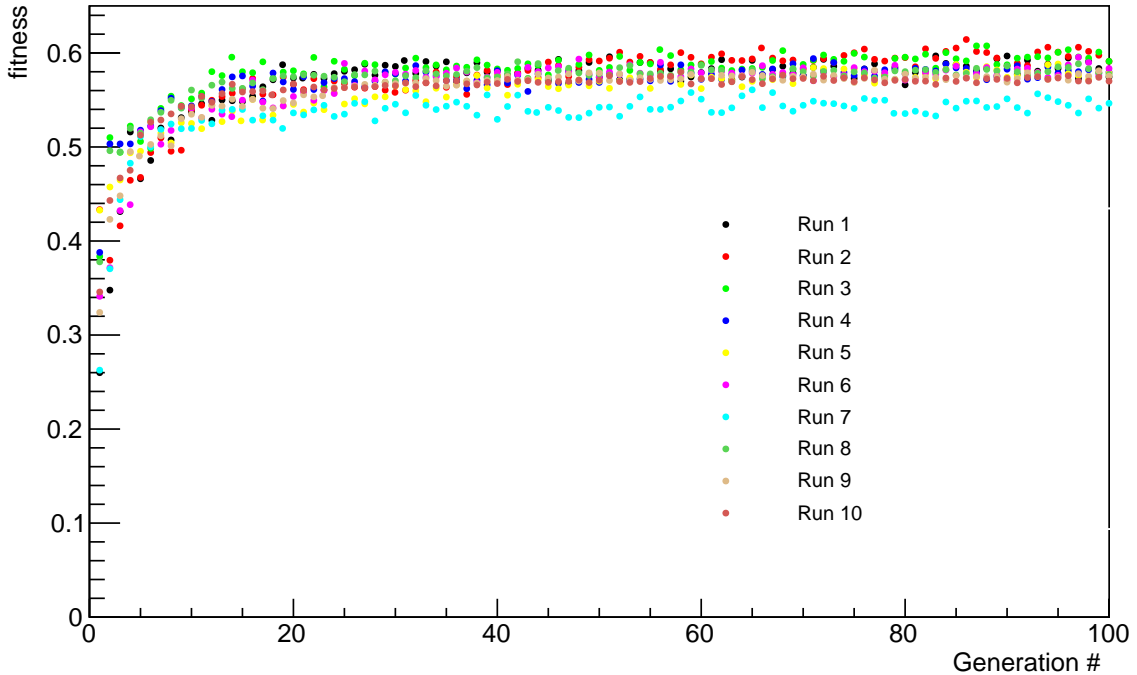


Figure 7.2: Fitness of each generation's best individual (beam configuration) for ten runs of genetic algorithm for the optimization of a neutrino beam for LENA. Fitness here is defined as in Equation 6.3.

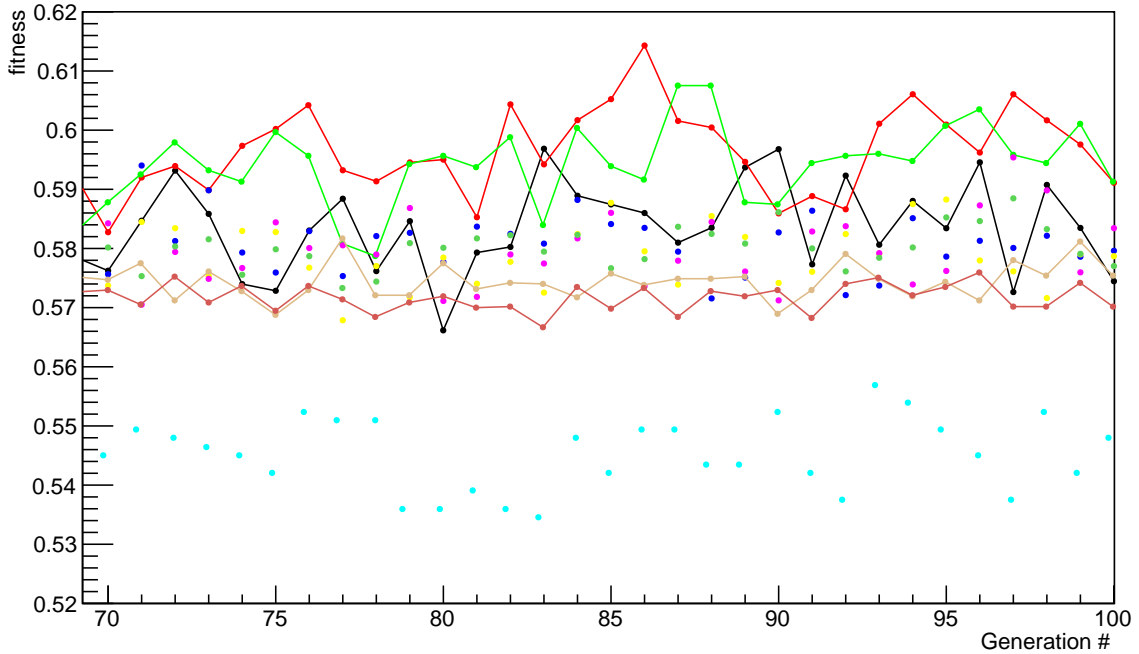


Figure 7.3: Zoom of Figure 7.2 for the last 30 generations of each run of the optimization for LENA. The lines indicate the runs with the lowest and the highest number of simulated events. The colours here correspond to the colour scheme in Figure 7.2

It can be seen from the figures that all the runs except for Run 7 converge on similar values for the maximum exclusion fraction at 3σ .

Figure 7.3 also shows that runs with the lower N_{sim} have wider fluctuations, as expected according to the mechanism explained in section 6.7.

The average fitness (sensitivity) value reached by the best individuals (winners) in generations 71 to 100 are summarized by the blue markers in Figure 7.4, with the error bars indicating the corresponding standard deviation. The red markers indicate the average fitness out of 10 simulations of the fittest individual (same beam setup configuration) of generation 100 (corresponding to the last point on the right in Figure 7.2) and the relative standard deviation in the error bars; the error for these measurements goes from $\sim 4\%$ for Runs 1, 2, 3, with 2000 simulated events, to $\sim 1\%$ for Runs 9, 10, with 20000 simulated events.

The algorithm's behaviour in section 6.7 can also explain why the blue markers look higher than the red markers: the genetic algorithm pushes by nature towards high values of the fitness figure, whether they come from a real goodness of the configuration or from a casual fluctuation towards the high end of the fitness distribution; blue markers are given by an average of "winners" (of real or "fictitious" good beam configurations), that are always pushed towards the upper limits of the distribution given by the red markers. This also causes the high-statistics runs to have lower average fitnesses in the blue graph, since for them the individuals' fitness distribution is narrower (smaller error bars in the red graph).

For this reason, in order to have a true more reliable estimate of the maximum sensitivity, it was chosen to consider individuals in the last generations of Runs 9, 10.

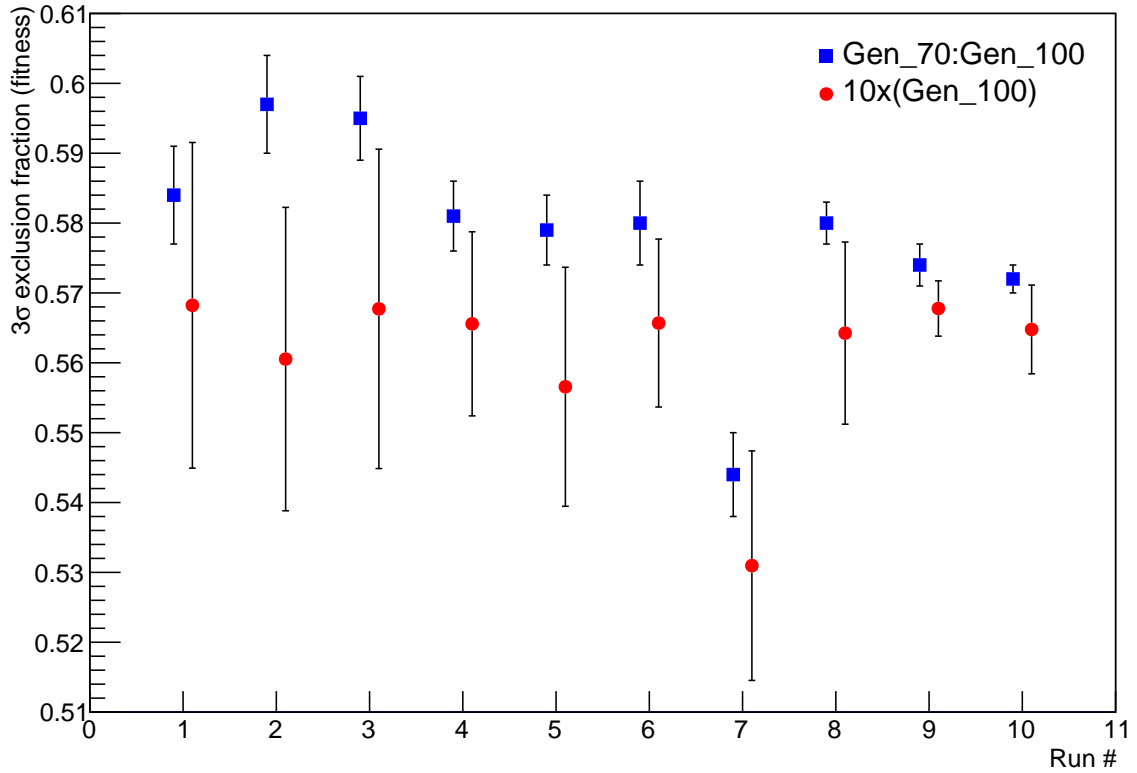


Figure 7.4: The blue markers indicate the average fitness and standard deviation of the best individuals (configurations) in the generations from 71 to 100. The red markers indicate the average fitness and standard deviation of ten simulations of the best individual in Generation 100.

7.2.1 Best beam setup configurations for LENA

The histograms in Figure 7.5 and Figure 7.6 show the distribution of the LENA beam configuration parameters for the winner individuals in Generation 100 for every run. See Appendix A for the same histograms for Generation 71 to Generation 100. The colour scheme is the same as in Figure 7.2.

It can be noted that the histograms relative to Run 7 are for many parameters (proton energy, target material and target diameter) quite displaced from the bulk of the distributions for the other runs: this is consistent with the generally worse sensitivity resulting from this run (see Figure 7.2).

The most favourable solutions also have a very large tunnel, both in length and radius: to verify the impact of these parameters one might perform a scan on them leaving the other parameters unchanged to determine the resulting variation of fitness.

The most favourable values for the proton energy and the beam power are close to the upper limits of the allowed ranges, with mean values around 50GeV and 4.9MW respectively.

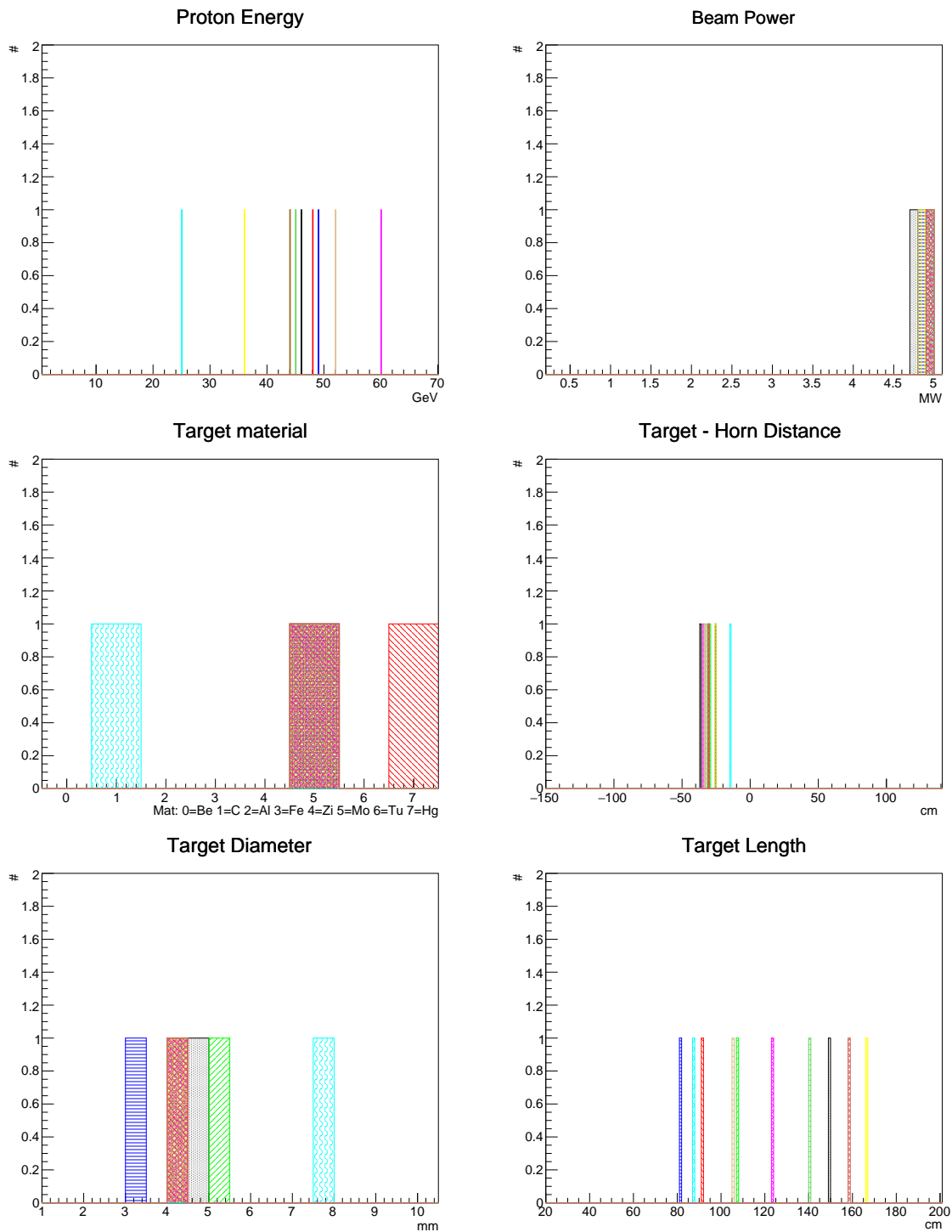


Figure 7.5: Distribution of the LENA beam configuration parameters for the winner individuals in generation 100 for each run (see also Figure 7.6). Here the distribution of proton energy, beam power and target-related parameters is illustrated.

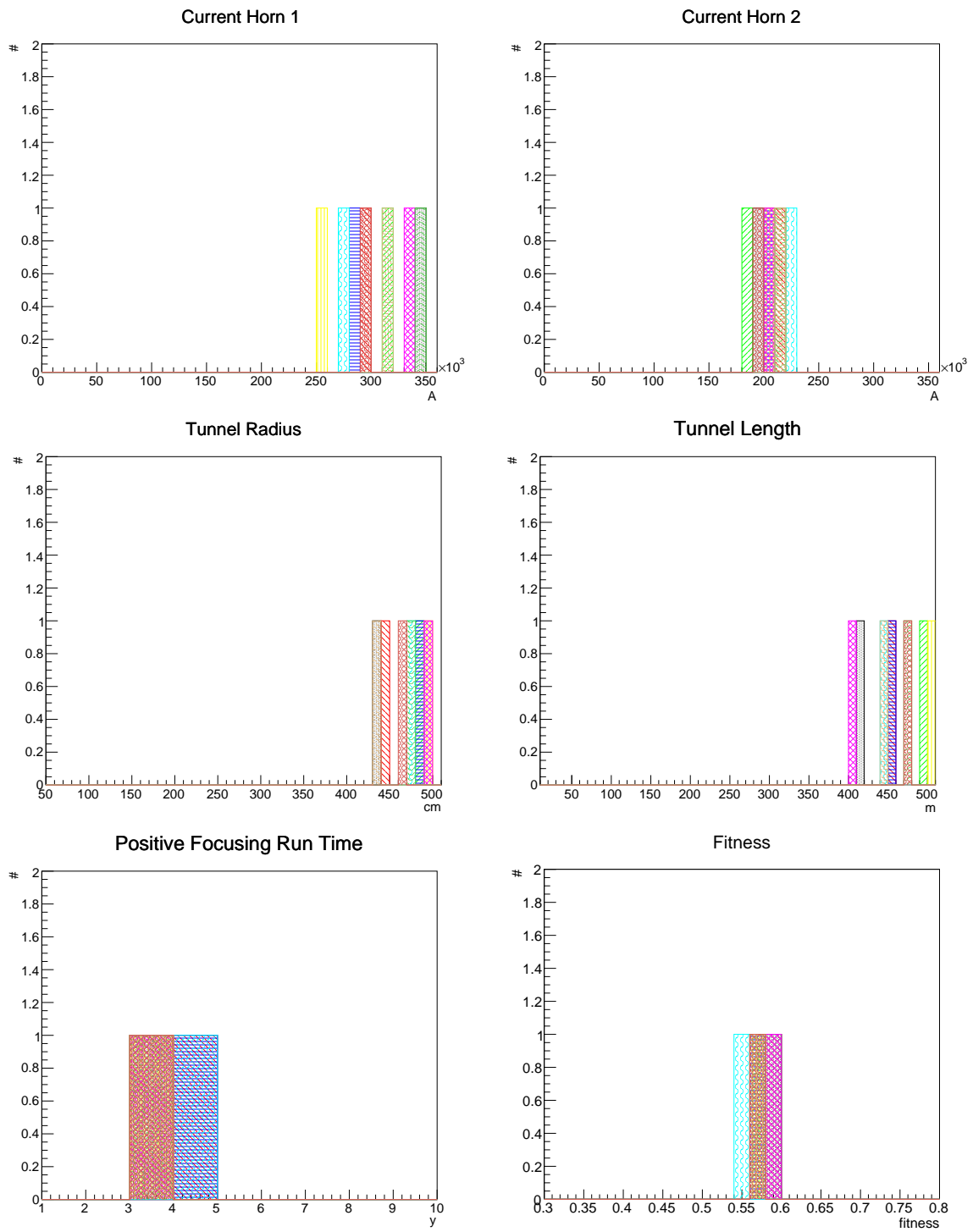


Figure 7.6: Distribution of the LENA beam configuration parameters for the winner individuals in generation 100 for each run. Here the distribution of horn currents, tunnel-related parameters, positive focusing time and resulting fitnesses values is illustrated.

The favourite target material seems to be Molybdenum, not a low-Z element, with a diameter of about 4mm; the target's distance to the first horn is distributed from -40cm to -20cm: the negative distance indicates that the target should be inside the first horn.

The first horn would require a current of about 300kA to perform an effective focusing, together with a ~ 200 kA current circulating in the reflector.

The recommended size of the decay tunnel according to this optimization would be quite large both in radius (4.5m) and in length (450m).

With a running time distribution of 4y for PF mode and 6y for the NF mode, sensitivity to CP violation at 3σ level would be reached by the optimization here presented for 57% of the δ_{CP} range.

7.2.2 A good beam setup: an example

The best setup from Generation 100 of Run 10 can be taken as an example of good configuration; its parameters are shown in Table 7.2.

ID	Gen	E	P	Mat_{tar}	D_{tar}	L_{tar}	Pos_{tar}	I_1	I_2	R_{tun}	L_{tun}	PF	$fitness$
		GeV	MW		mm	cm	cm	kA	kA	cm	m	y	$f(3\sigma)$
1694905	100	44.0	4.9	Molybdenum	4.0	158.0	-31.0	290	190	460	470	3	0.570592

Table 7.2: Example of a good configuration for the LENA beam.

A peculiarity of this setup configuration is a very long Mo target (158cm), positioned deeply inside the horn.

The beam neutrino spectra produced with this setup are shown in Figure 7.7, while Table 7.3 gives the total number of neutrinos produced by the setup configuration #1694905, with $6.95077 \cdot 10^{21}$ p.o.t./y. The flux is normalized to 1MeV binning on a 100m^2 surface at a distance of 100km.

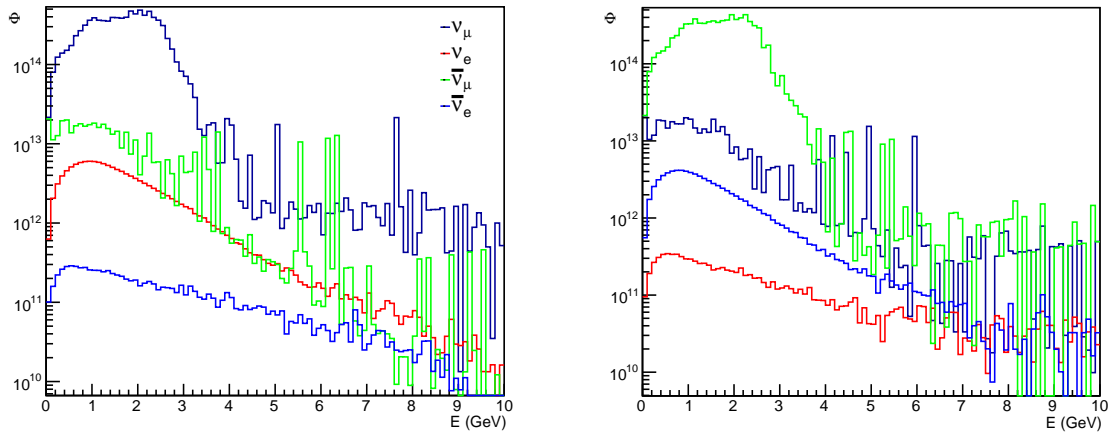


Figure 7.7: Spectra of the neutrinos produced in the beam configuration #1694905 in positive focusing mode (left) and negative focusing mode (right). The flux is normalized to 1MeV binning on a 100m^2 surface at a distance of 100km.

	PF		NF	
ν_μ	$9.19314e+15$	93.8372%	$4.44964e+14$	5.03408%
$\bar{\nu}_\mu$	$4.5714e+14$	4.66617%	$8.29717e+15$	93.8697%
ν_e	$1.36765e+14$	1.39601%	$1.06481e+13$	0.120467%
$\bar{\nu}_e$	$9.85528e+12$	0.100596%	$8.62434e+13$	0.975711%

Table 7.3: Total number of ν produced in the beam configuration #1694905.

Figure 7.8 shows the reconstructed energy spectra for the selected configuration for the ν_e appearance search in the positive focusing mode and for the $\bar{\nu}_e$ appearance in the negative focusing mode.

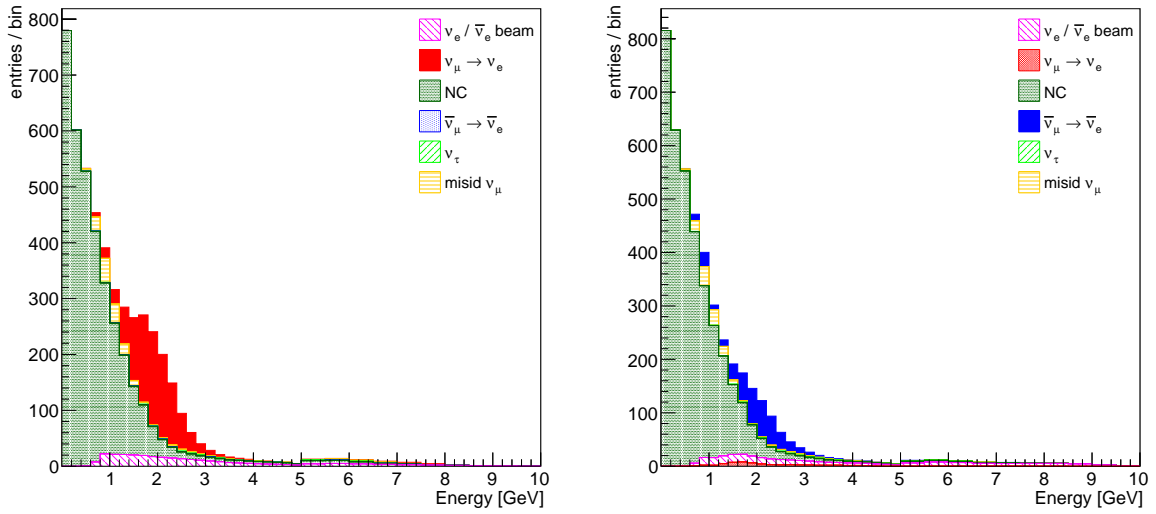


Figure 7.8: Reconstructed energy spectra for the ν_e appearance search (PF mode, left) and for the $\bar{\nu}_e$ appearance (NF mode right). The bin width corresponds to the bin width in the energy migration matrices.

7.2.3 Effect of beam contamination

In order to test the influence of the focusing system on the total sensitivity, a test was performed by artificially removing the $\bar{\nu}_\mu$ (ν_μ), ν_e $\bar{\nu}_e$ background components from the neutrino fluxes obtained from the simulation of configuration #1694905.

The results of this test are shown in Figure 7.9 and Figure 7.10: the former illustrates the test statistics $\Delta\chi^2$ for each possible true δ_{CP} , while the latter shows the Fraction of the δ_{CP} interval that would exclude CP violation as a function of the confidence level for the exclusion of the no-violation hypothesis.

It can be seen from that Figure 7.9 that in the case of a pure $\nu_\mu/\bar{\nu}_\mu$ flux the peak value for $\Delta\chi^2$ would have a 20% increase relative to the default configuration with normal backgrounds. Consequently, the δ_{CP} exclusion fraction at 3σ level would increase from 57% to almost 62% with the pure beam.

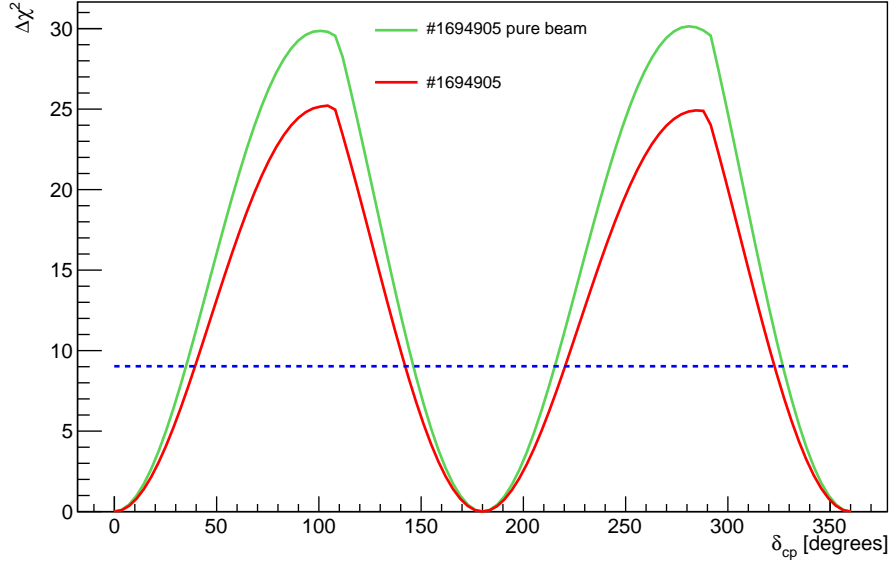


Figure 7.9: Value of the test statistics $\Delta\chi^2$ for each possible true δ_{CP} for the configuration #1694905 (see Table 7.2) from Run 10, generation 100 of the LENA beam optimization. The red curve refers to the configuration as simulated in the run, while the green curve refers to the ideal scenario of a pure ν_μ beam ($\bar{\nu}_\mu$ in NF mode).

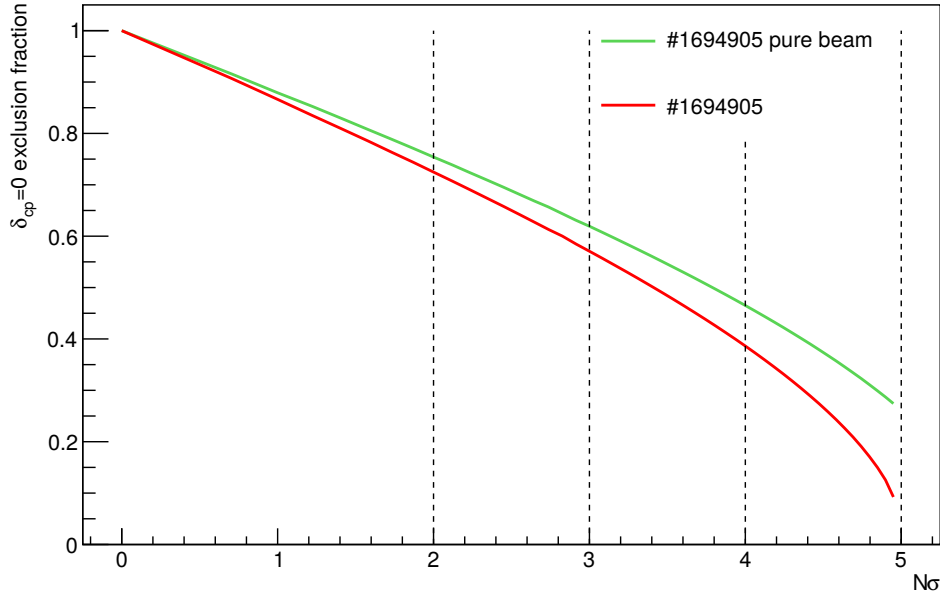


Figure 7.10: Fraction of the δ_{CP} interval that would exclude CP violation as a function of the confidence level for the exclusion of the no-violation hypothesis. The red curve refers to the configuration #1694905 as simulated in the run, while the green curve represents the ideal case of a pure $\nu_\mu/\bar{\nu}_\mu$ beam.

7.3 Beam optimization for the JUNO detector

The optimization of the beam to JUNO was performed by taking 11 runs of the genetic algorithm, here too evolving for 100 generations (see Figure 7.11).

Since the sensitivity to CP violation reached in this optimization was so small, the fitness value was not defined according to the definition in chapter 6 but was set to coincide with the peak value of the test statistics: $\mathcal{F} \equiv \max(\Delta\chi^2)$.

In the case of the optimization for JUNO, Run 10 was not able to perform to the best fitness in the given number of generations, while Run 4 and Run 6 exhibit a sudden "jump" from a local maximum to the global maximum.

In this case the number of simulated events was set to $N_{\text{sim}} = 2 \cdot 10^4$ for every run; this causes the fluctuations of the fitness values to be more homogeneous across the runs, as can be seen in Figure 7.12. Figure 7.13 shows that $\frac{\sigma_{\mathcal{F}}}{\mathcal{F}} \sim 4\%$ for the JUNO beam with $N_{\text{sim}} = 2 \cdot 10^4$.

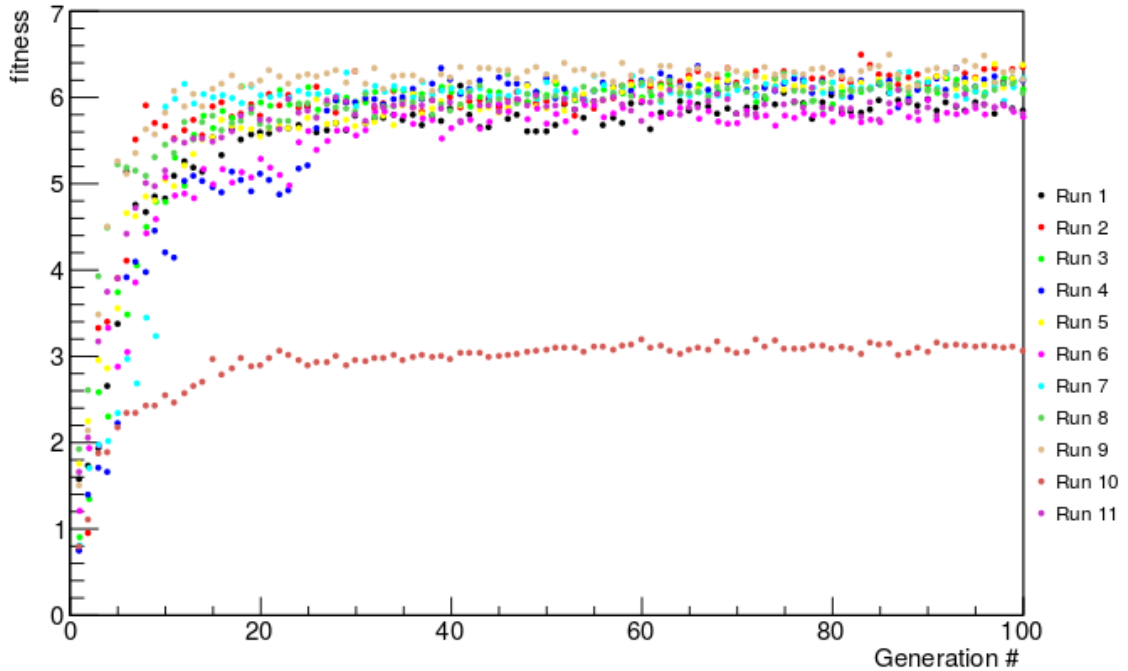


Figure 7.11: Fitness of each generation's best individual (beam configuration) for 11 runs of genetic algorithm for the optimization of a neutrino beam for JUNO. Fitness is here defined as $\mathcal{F} \equiv \max(\Delta\chi^2)$.

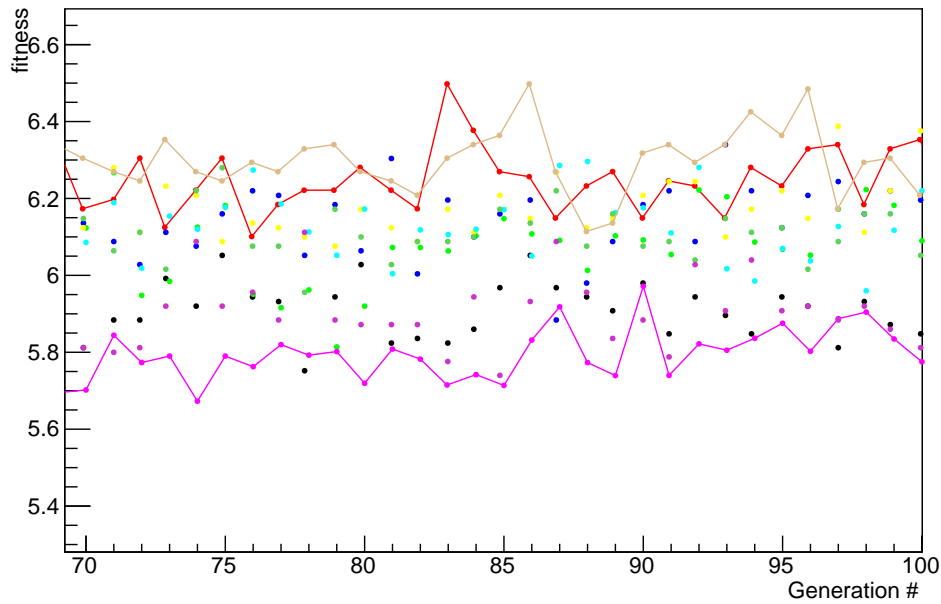


Figure 7.12: Zoom of Figure 7.11 for the last 30 generations of each run. The lines indicate here the runs with the lowest and the highest average fitness values.

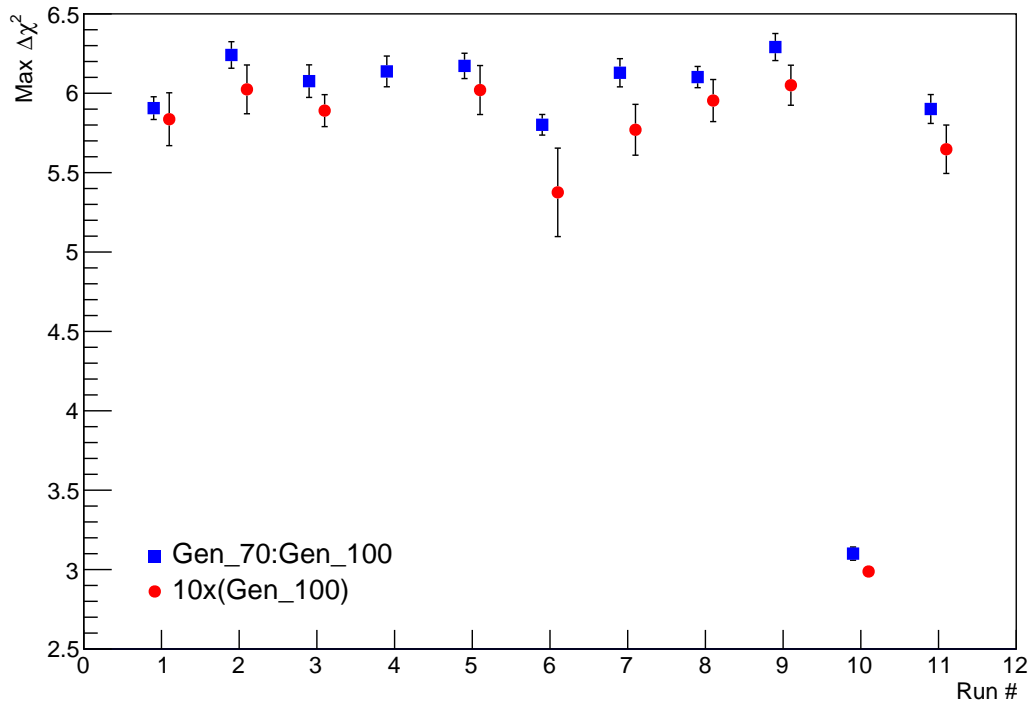


Figure 7.13: The blue markers indicate the average fitness and standard deviation of the best individuals (configurations) in the generations from 71 to 100. The red markers indicate the average fitness and standard deviation of ten simulations of the best individual in Generation 100.

7.3.1 Best beam setup configurations for JUNO

The histograms in Figure 7.14 and Figure 7.15 show the distribution of the JUNO beam configuration parameters for the winner individuals in Generation 100 for all the runs. See Appendix A for the same histograms for Generation 71 to Generation 100.

In this case, too, the non-effective GA run, Run 10, differs from the higher-fitness runs in almost all of the parameters: its proton energy at 11GeV is one order of magnitude higher than the most favourable 1GeV.

The beam power is pushed to the border of the optimization interval, indicating that an ever bigger power would maybe lead to better results; the same can be noted for the current in the first horn.

The most favourable target material for this low-energy beam is graphite and the distance between the target and the first horn is negative, indicating that the target is at least partially inside the horn.

The running time is 9y (out of 10y total) in the positive focusing mode, indicating a preference for the ν_μ beam.

7.3.2 A “good” beam setup: an example

The best setup from Generation 100 of Run 3 can be taken as an example of good configuration; its parameters are shown in Table 7.4.

ID	Gen	E	P	Mat_{tar}	D_{tar}	L_{tar}	Pos_{tar}	I_1	I_2	R_{tun}	L_{tun}	PF	$fitness$
		GeV	MW		mm	cm	cm	kA	kA	cm	m	y	$\max(\Delta\chi^2)$
12838477	100	1.2	4.9	Graphite	8.5	159.0	-40.5	340	120	360	240	9	6.06883

Table 7.4: Example of a good configuration for the JUNO beam.

Figure 7.16 and Table 7.5 illustrate the neutrino spectra produced from CSNS in the simulation with the beam setup #12838477 and the integrals of the neutrino fluxes, respectively.

	PF		NF	
ν_μ	$4.27641e + 14$	95.3454%	$2.0943e + 13$	28.8894%
$\bar{\nu}_\mu$	$1.15574e + 13$	2.57681%	$5.06908e + 13$	69.9242%
ν_e	$9.29506e + 12$	2.07239%	$1.59976e + 11$	0.220676%
$\bar{\nu}_e$	$2.42693e + 10$	0.005411%	$7.00145e + 11$	0.965799%

Table 7.5: Total number of ν produced in the beam configuration #12838477.

Figure 7.17 shows the reconstructed energy spectra for the selected configuration for the ν_e appearance search in the positive focusing mode and for the $\bar{\nu}_e$ appearance in the negative focusing mode.

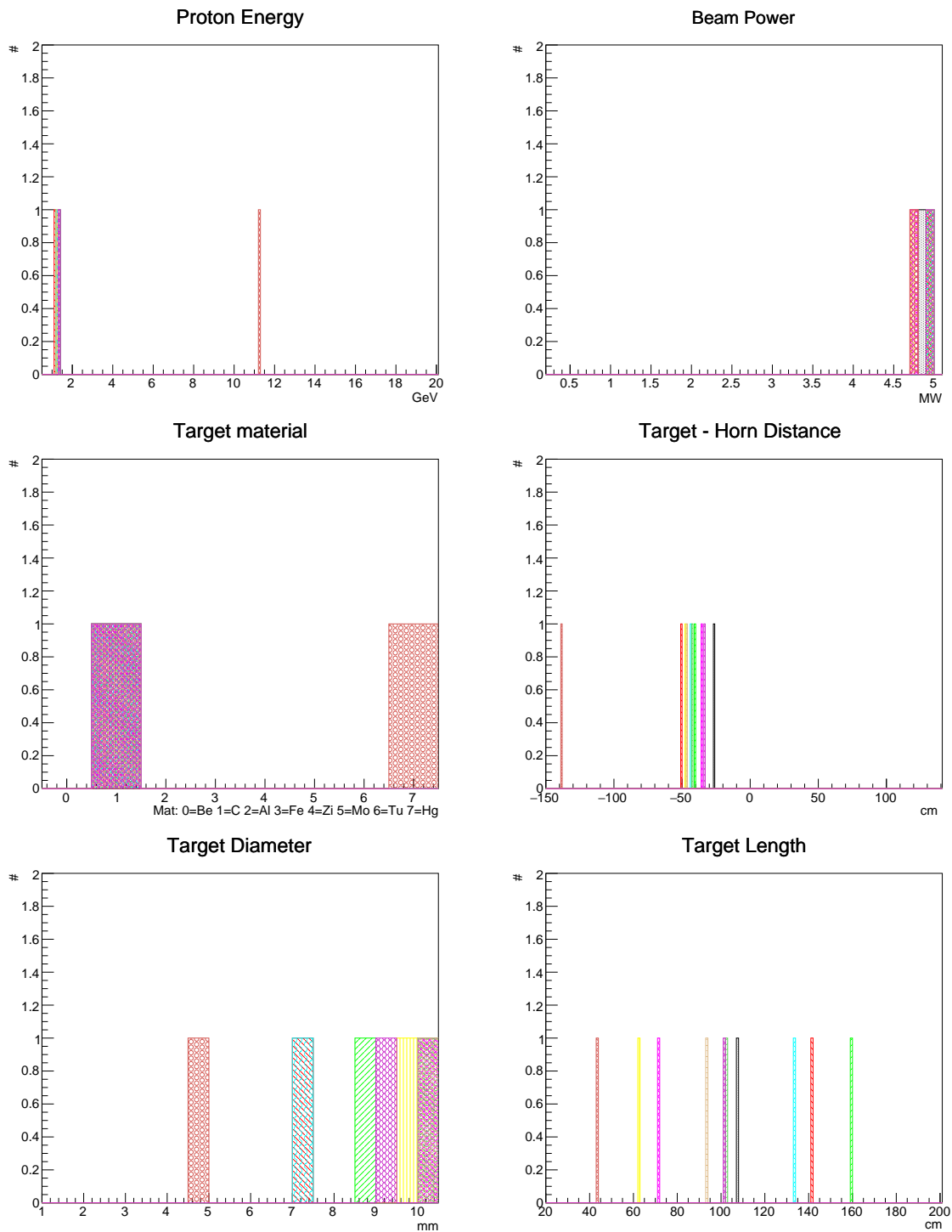


Figure 7.14: Distribution of the JUNO beam configuration parameters for the winner individuals in generation 100 for each run (see also Figure 7.15). Here the distribution of proton energy, beam power and target-related parameters is illustrated.

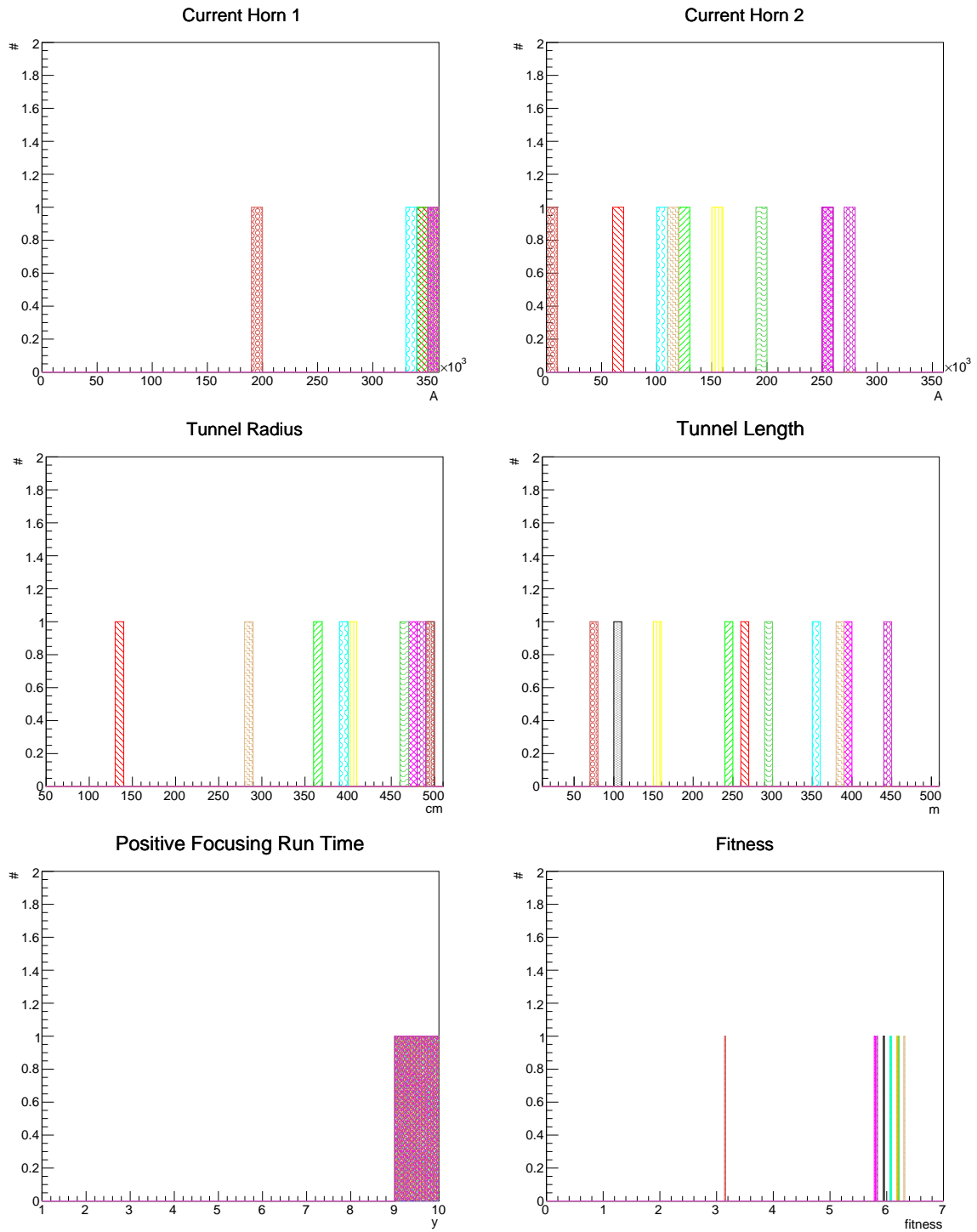


Figure 7.15: Distribution of the JUNO beam configuration parameters for the winner individuals in generation 100 for each run. Here the distribution of horn currents, tunnel-related parameters, positive focusing time and resulting fitnesses values is illustrated.

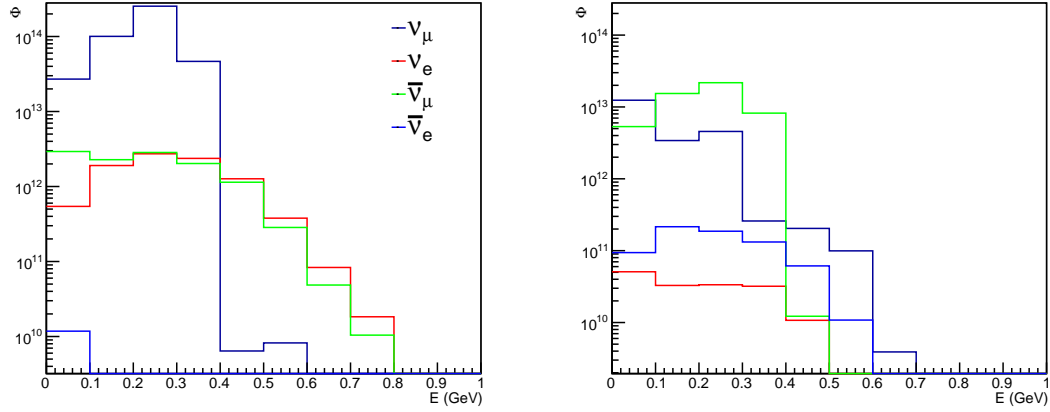


Figure 7.16: Spectra of the neutrinos produced in the beam configuration #12838477 in positive focusing mode (left) and negative focusing mode (right). The flux is normalized to 1MeV binning on a 100m^2 surface at a distance of 100km.

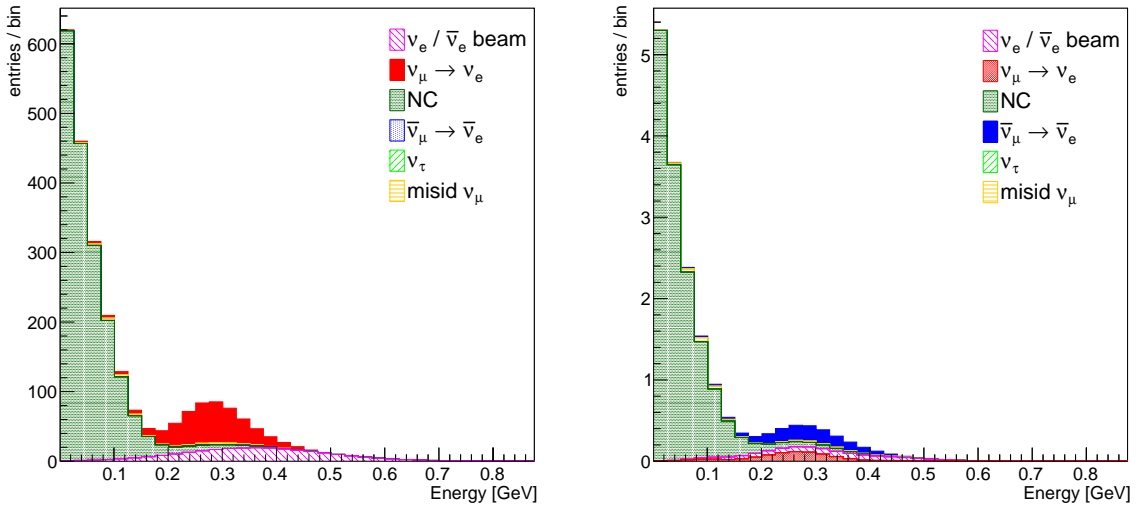


Figure 7.17: Reconstructed energy spectra for the ν_e appearance search (PF mode, left) and for the $\bar{\nu}_e$ appearance (NF mode right). The bin width corresponds to the bin width in the energy migration matrices.

7.3.3 Effect of beam contamination

The results of this test are shown in Figure 7.18 and Figure 7.19: as in subsection 7.2.3, the former illustrates the test statistics $\Delta\chi^2$ for each possible true δ_{CP} , while the latter shows the fraction of the δ_{CP} interval that would exclude CP violation as a function of the confidence level for the exclusion of the no-violation hypothesis. It can be seen from that Figure 7.18 that in the case of a pure $\nu_\mu/\bar{\nu}_\mu$ flux the peak value for $\Delta\chi^2$ would have a 20% increase relative to the default configuration with normal backgrounds. Consequently, the δ_{CP} exclusion fraction at 2σ level would increase from 30% to almost 37% with the pure beam.

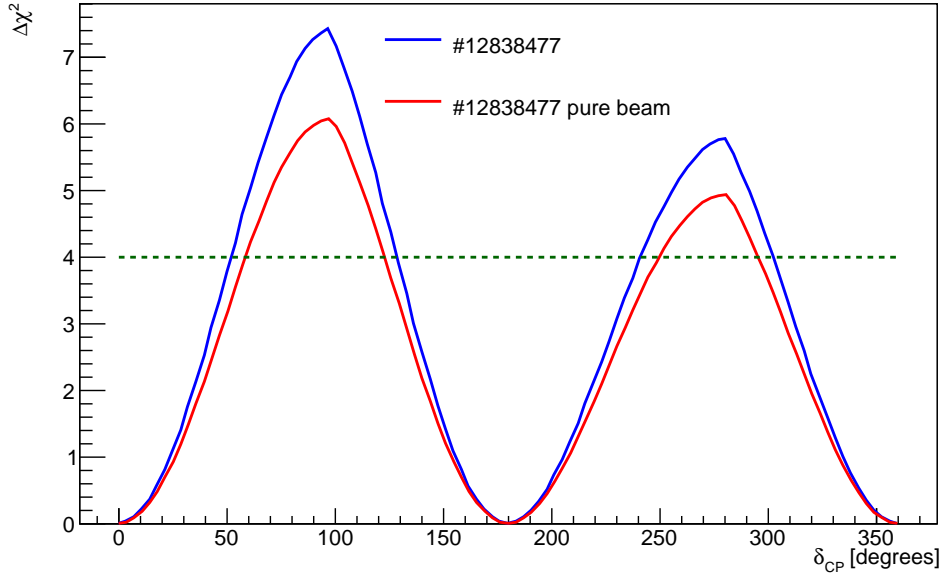


Figure 7.18: Value of the test statistics $\Delta\chi^2$ for each possible true δ_{CP} for the configuration #112838477 (see Table 7.4) from Run 3, generation 100 of the JUNO beam optimization. The red curve refers to the configuration as simulated in the run, while the blue curve refers to the ideal scenario of a pure ν_μ beam ($\bar{\nu}_\mu$ in NF mode).

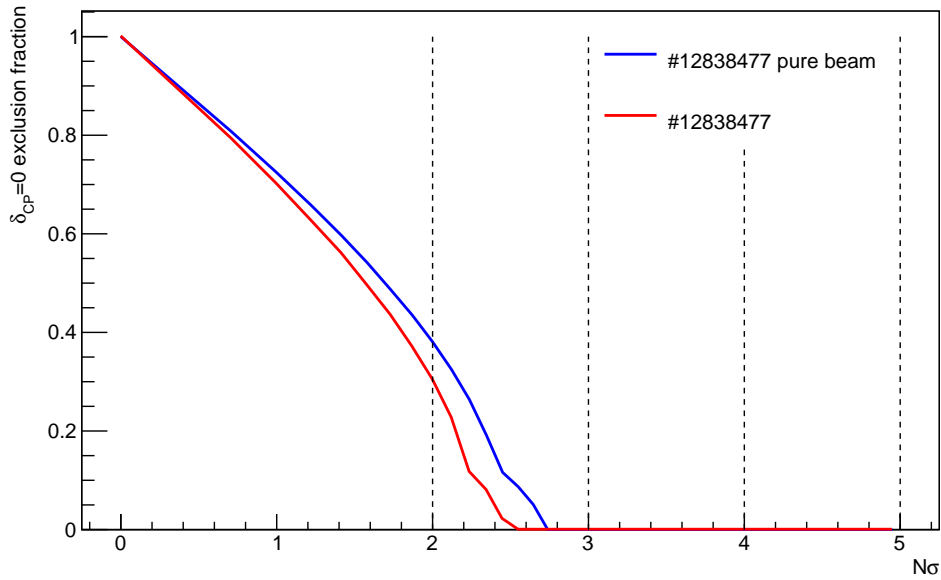


Figure 7.19: Fraction of the δ_{CP} interval that would exclude CP violation as a function of the confidence level for the exclusion of the no-violation hypothesis. The red curve refers to the configuration #12838477 as simulated in the run, while the green curve represents the ideal case of a pure $\nu_\mu/\bar{\nu}_\mu$ beam.

Chapter 8

Conclusions

Neutrino physics is an important topic in present research because of the great interest in both the intrinsic properties of these elementary particles and in their role as messengers from terrestrial and extraterrestrial sources.

Among the intrinsic properties of neutrinos the phenomenon of flavour oscillation is the subject of many experimental investigations that try to perform precise measurements of its many parameters: among them, the value of the CP-violating phase δ_{CP} and the neutrino mass hierarchy are still unknown.

This thesis focused on the determination of CP violation in neutrino oscillation with the use of neutrino beams to the liquid-scintillator neutrino detectors LENA (50kt detector in Pyhäsalmi, Finland) and JUNO (20 kt detector in Jiangmen, China).

In the first part a simulation of a neutrino beam was built and the sensitivity to CP violation evaluated for a given beam configuration on the basis of the detectors' properties. The beam simulation was tested by the reproduction of neutrino fluxes from *Institute of High Energy Physics (IHEP)* (Protvino, Russia); the comparison of the results with previously published simulation results of the same beam setup configuration [57] confirmed the reliability of the simulation tools used in this work.

In the second part of the thesis a genetic algorithm was implemented in order to optimize the beam configuration so to reach the highest sensitivity to CP violation for LENA and JUNO at the chosen baselines. The optimization parameters were the proton energy and beam power, the target material and size, the current circulating in the focusing elements, the decay tunnel size and the time of operation in the positive focusing mode (producing a ν_μ beam) on a total of 10y running time. The geometry of the focusing system was not considered for optimization. Due to statistical fluctuations and the (unknown) intrinsic topology of the parameter space, the optimization algorithm cannot pinpoint ONE optimal configuration of the beam setup but can only suggest more or less narrow ranges for each parameter.

The results of the simulations indicate that:

- a neutrino beam from the designed *European Spallation Source* (ESS, in Lund, Sweden) proton accelerator (with 2GeV proton energy, 5MW beam power) to the LENA detector

would give as a limit value for the test statistics $\max(\Delta\chi^2) \leq 0.009$, meaning no significant sensitivity to CP violation.

- A neutrino beam to LENA from the same distance as ESS (1134km) would reject the no-CP-violation values of δ_{CP} at a 3σ level for $\sim 57\%$ of the range if produced by protons with an energy of $\sim 50\text{GeV}$ and a beam power close to 5MW. The total 10y running time of the experiment should be distributed in 3y in the positive focusing mode (main ν_μ beam) and 7y in the negative focusing mode (main $\bar{\nu}_\mu$ beam). The preferred target material among the examined choices was shown to be molybdenum ($Z = 42, a = 95.95\text{g/mol}$).
- A 150km accelerator-detector baseline was investigated for a beam to the JUNO detector, equal to the distance from the *China Spallation Neutron Source* (CSNS in Dongguan, China) to Jiangmen. A neutrino beam to JUNO optimized for this distance would yield a peak value for the test statistics $\max(\Delta\chi^2) \sim 6$, giving a 2σ rejection of the no-CP hypothesis for 30% of the whole δ_{CP} interval.

In this case the most favourable proton energy indicated by the algorithm is 1GeV and the best target material is graphite.

The effect of beam contamination from background neutrino flavours was explored for both the LENA and JUNO cases by considering a beam configuration indicated by the optimization as one of the most favourable for the experiment's sensitivity and artificially setting to zero the background components of the beam, i.e. using the pure ν_μ flux ($\bar{\nu}_\mu$ in negative focusing mode); the 3σ exclusion fraction for LENA would increase from 57% to almost 62%, while the 2σ exclusion fraction for JUNO would increase from 30% to $\sim 37\%$.

Outlook

In the light of the improvements in sensitivity shown by the "pure-beam scenario" investigation, a new and more detailed optimization of the neutrino beam setup should include the geometry of the focusing system, in order to achieve an actual sensitivity closer to the aforementioned values.

More possibilities for the target material shape could be explored, including different configurations for segmented targets. Technical limitations and cost/effectiveness ratios should be considered in a realistic feasibility study; the algorithm employed in the optimization could be implemented so as to take these factors into account in the search for the real best beam setup.

New optimizations and studies of LENA and JUNO as far detectors for long baseline neutrino experiments could be performed in the future in the light of new event reconstruction algorithms currently being elaborated, that could significantly improve the performance of liquid-scintillator neutrino detectors in the GeV energy domain.

Appendix A

Beam parameters distributions for 30 generations

Figure A.1 and Figure A.2 show the distribution of the LENA beam configuration parameters for the winner individuals in generations 71 to 100 for each run.

Figure A.3 and Figure A.4 show the distribution of the JUNO beam configuration parameters for the winner individuals in generations 71 to 100 for each run.

The colour scheme is the same as in Figure 7.2.

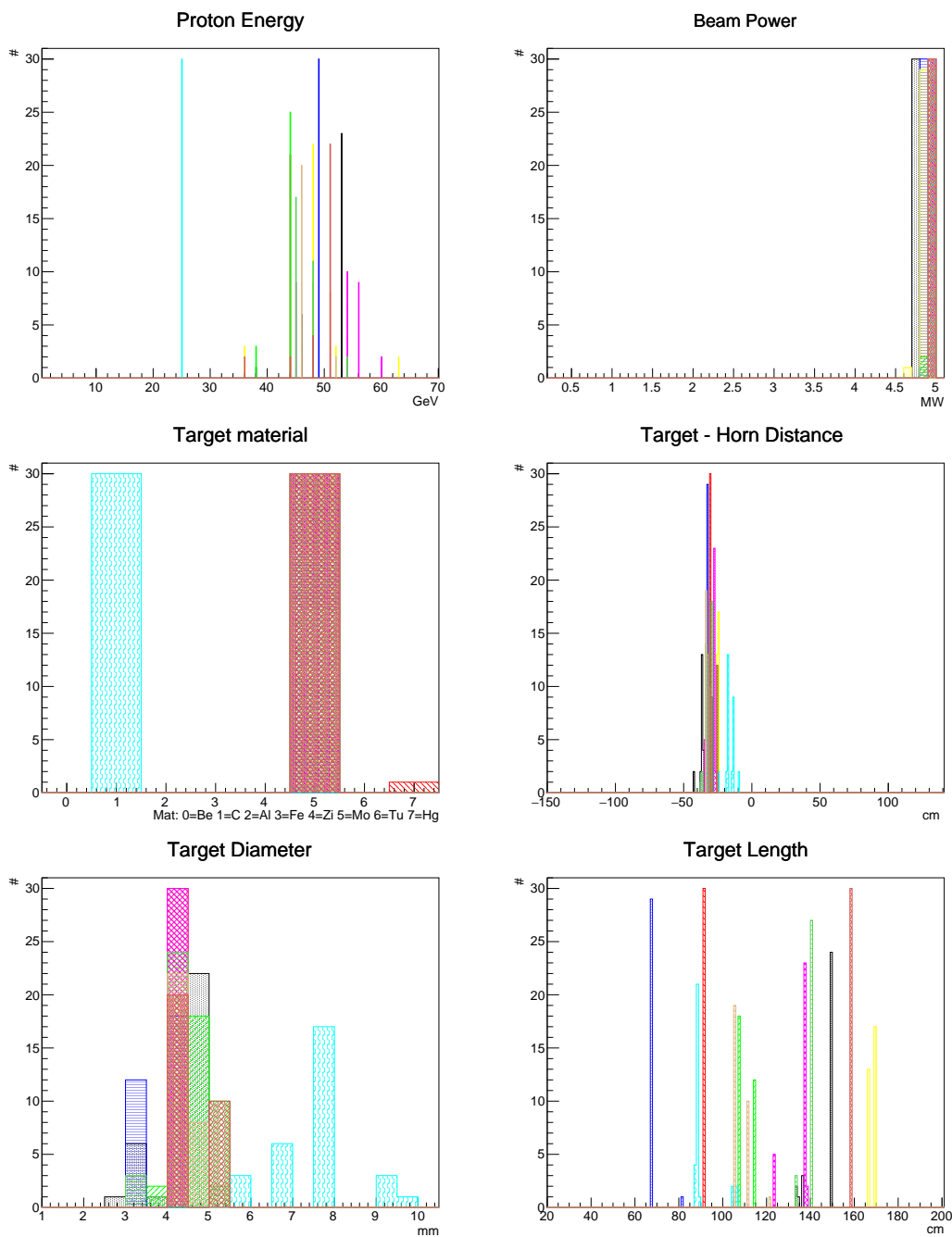


Figure A.1: Distribution of the LENA beam configuration parameters for the winner individuals in generations 70 to 100 for each run (see also Figure 7.6). Here the distribution of proton energy, beam power and target-related parameters is illustrated.

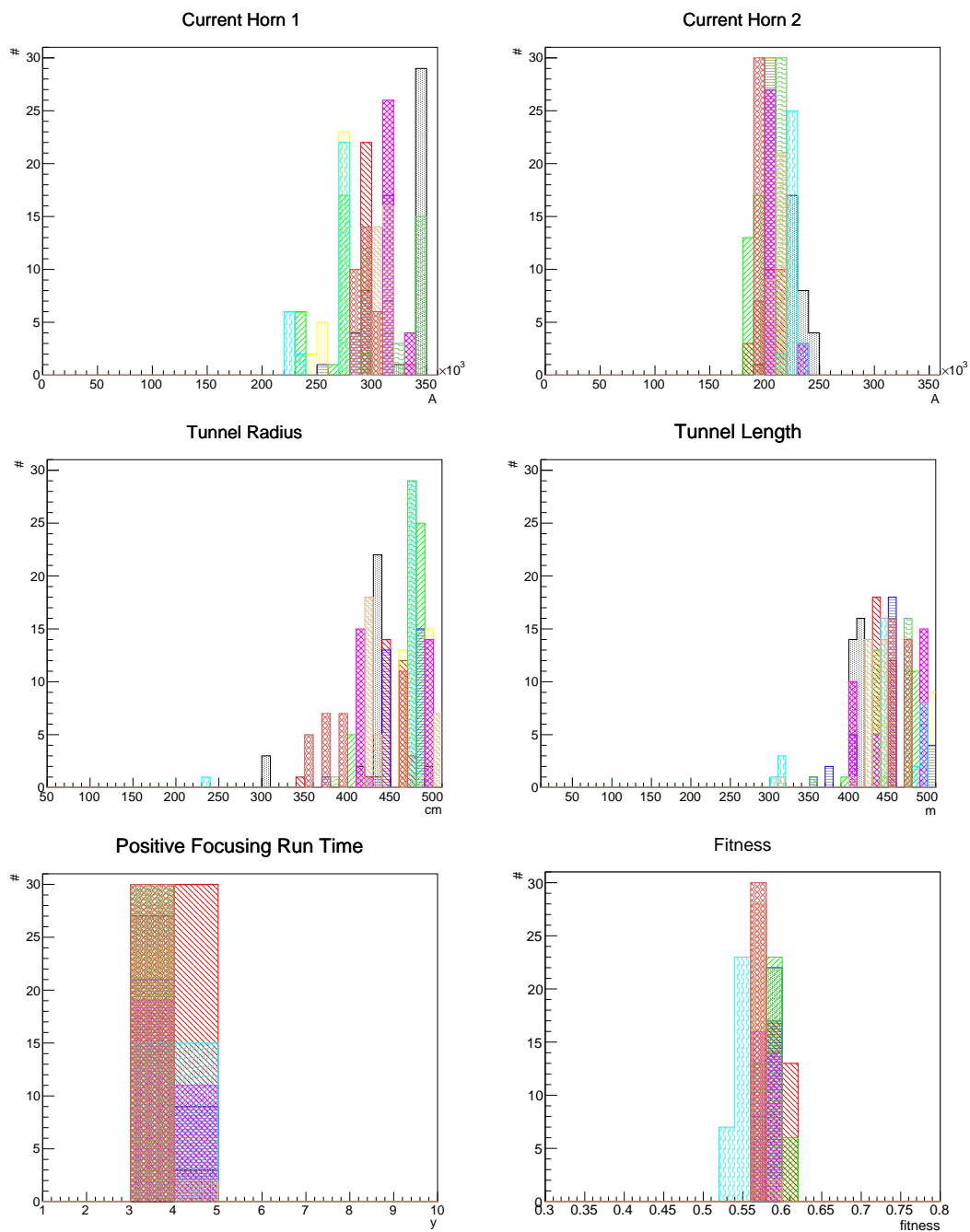


Figure A.2: Distribution of the LENA beam configuration parameters for the winner individuals in generations 70 to 100 for each run (see also). Here the distribution of horn currents, tunnel-related parameters, positive focusing time and resulting fitnesses values is illustrated.

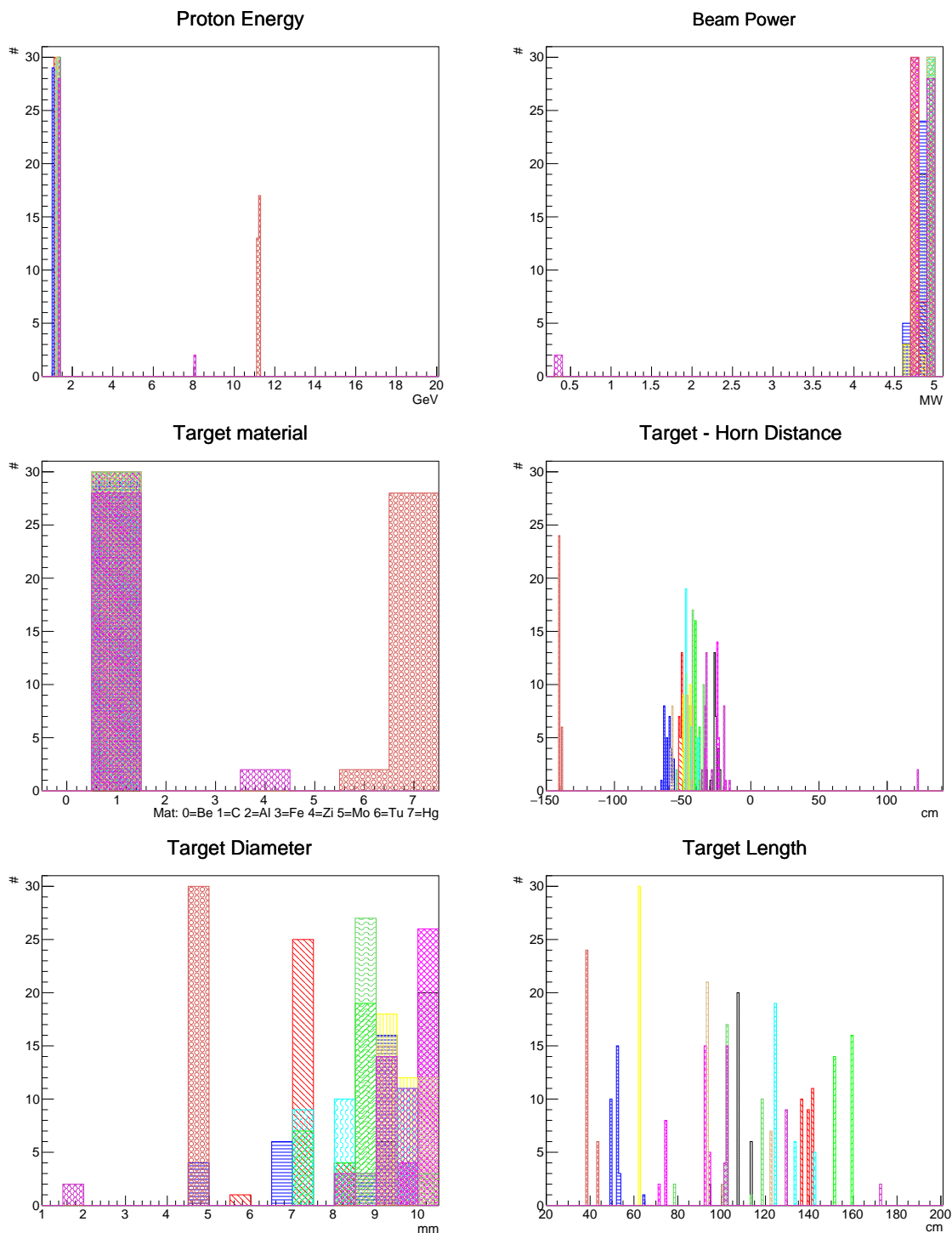


Figure A.3: Distribution of the JUNO beam configuration parameters for the winner individuals in generations 70 to 100 for each run (see also Figure 7.6). Here the distribution of proton energy, beam power and target-related parameters is illustrated.

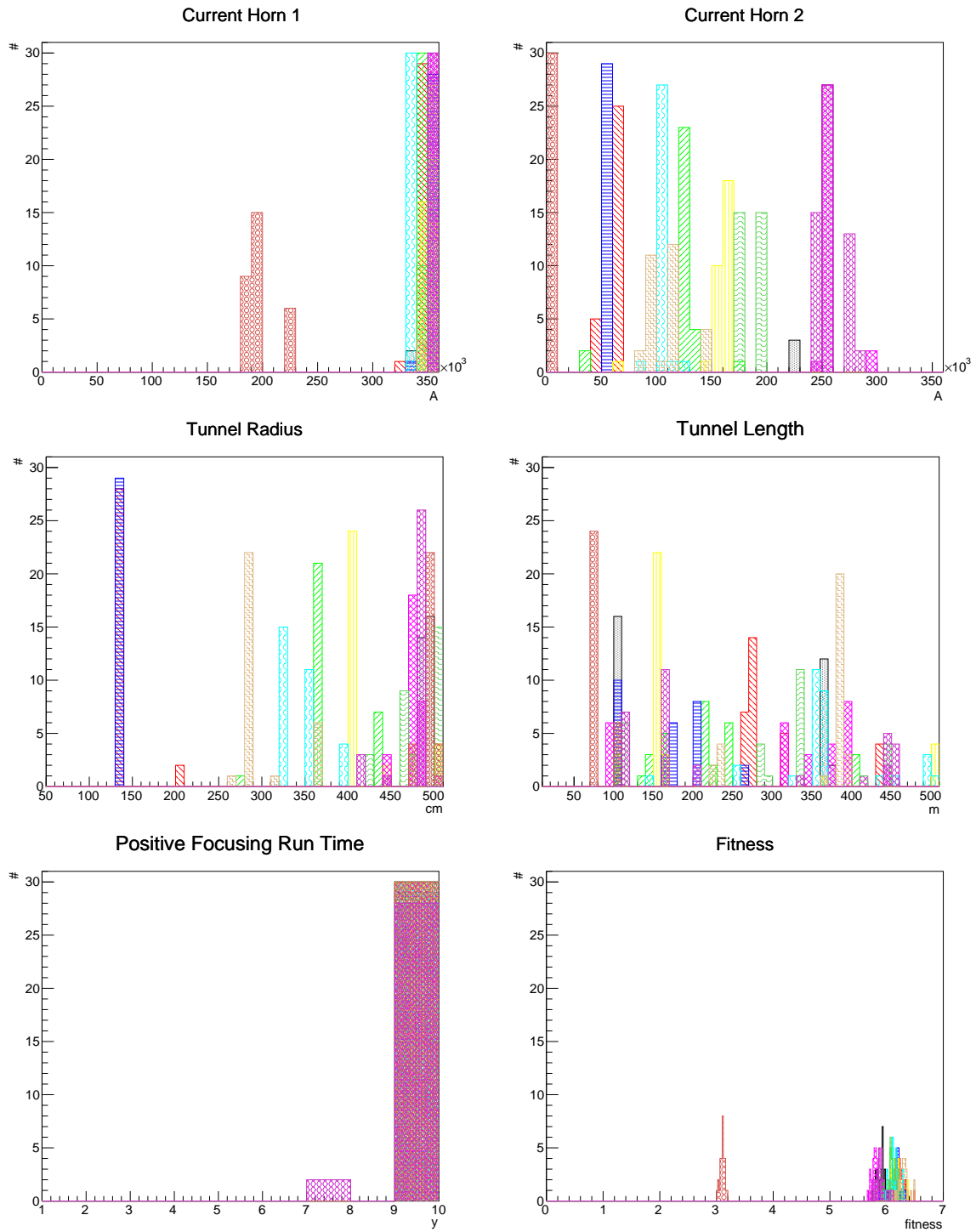


Figure A.4: Distribution of the JUNO beam configuration parameters for the winner individuals in generations 70 to 100 for each run (see also). Here the distribution of horn currents, tunnel-related parameters, positive focusing time and resulting fitnesses values is illustrated.

Acknowledgements

I am so lucky to have a long list of people to thank at the end of this work:

- my supervisor, Prof. Achim Stahl, for giving me the opportunity to work on this interesting project and his support during my time as a PhD student.
- Prof. Livia Ludhova for her help in the last agitated stages of this journey.
- Regione Sardegna for providing the scholarship that allowed me to undertake this PhD (special thanks to Daniela Derosas from Ufficio Rendicontazione for her infinite kindness).
- Prof. Christopher Wiebusch for the interest he has shown in my work and the constant inputs during the weekly group meetings and more in general to the whole Double Chooz/Juno working group.
- The core of the group Michi, Ilja, Stefan, Denise and the two Philipps (Alpha and Bravo), who proved to be the best of colleagues and good friends and provided a great working environment.
- Andrea Longhin and especially Sebastian Lorenz, always willing to help and open for discussion, for their big contribution to this work.
- The whole IIIB Institute, full of friendly and helpful people who have always made me feel welcome.
- Max, Leila (so supportive when I was panicking!), Adriana, Debbie, Matthias for adding to the general niceness of life in Aachen.
- Ronja, Jan, Claudia and Dennis for cookies, pizza, movies, trips and the many more joyful moments that I hope we will keep on having together.
- My parents, for their support, patience and closeness even from a distance.
- ILJA again and again, for being always on my side.

Bibliography

- [1] W. PAULI, *Letter to Tübingen conference participants*, Dec. 1930.
- [2] C. L. COWAN JR. *et al.*, *Detection of the free neutrino: a confirmation*, SCIENCE, 124 (1956), p. 103.
- [3] (PARTICLE DATA GROUP) K.A. OLIVE *et al.*, *Review of Particle Physics*, Chin. Phys. C, 38 (2014), p. 090001. URL: <http://pdg.lbl.gov>.
- [4] G. DANBY *et al.*, *Observation of high-energy neutrino reactions and the existence of two kinds of neutrinos*, Physical Review Letters, 9 (1962), p. 36.
- [5] DONUT Collaboration, K. KODAMA *et al.*, *Observation of tau neutrino interactions*, Physics Letters B, 504 (2001), p. 218.
- [6] C. GIUNTI AND C. W. KIM, *Fundamentals of neutrino physics and astrophysics*, Oxford University Press, 2007.
- [7] J. A. FORMAGGIO AND G. P. ZELLER, *From eV to EeV: Neutrino Cross Sections Across Energy Scales*, Reviews of Modern Physics, 84 (2012), p. 1307.
- [8] LSND Collaboration, A. AGUILAR *et al.*, *Evidence for neutrino oscillations from the observation of $\bar{\nu}_e$ appearance in a $\bar{\nu}_\mu$ beam*, Phys. Rev. D, 64 (2001), p. 112007.
- [9] MiniBooNE Collaboration, A. A. AGUILAR-AREVALO *et al.*, *Improved Search for $\bar{\nu}_\mu \rightarrow \bar{\nu}_e$ Oscillations in the MiniBooNE Experiment*, Phys. Rev. Lett., 110 (2013), p. 161801.
- [10] B. PONTECORVO, *Neutrino experiments and the problem of conservation of leptonic charge*, Soviet Physics JETP, 26 (1968), p. 984.
- [11] Super-Kamiokande Collaboration, Y. FUKUDA *et al.*, *Evidence for oscillation of atmospheric neutrinos*, Physical Review Letters, 81 (1998), p. 1562.
- [12] SNO Collaboration, Q. R. AHMAD *et al.*, *Direct evidence for neutrino flavor transformation from neutral-current interactions in the sudbury neutrino observatory*, Physical Review Letters, 89 (2002), p. 011301.
- [13] MACRO Collaboration, M. AMBROSIO *et al.*, *Measurement of the atmospheric neutrino-induced upgoing muon flux using macro*, Physics Letters B, 434 (1998), p. 451.
- [14] M. SANCHEZ *et al.*, *Measurement of the L/E distributions of atmospheric ν in Soudan 2 and their interpretation as neutrino oscillations*, Physical Review D, 68 (2003), p. 113004.

- [15] K2K Collaboration, M.H. AHN *et al.*, *Measurement of neutrino oscillation by the K2K experiment*, Physical Review D, 74 (2006), p. 072003.
- [16] MINOS Collaboration, D. MICHAELS *et al.*, *Observation of muon neutrino disappearance with the minos detectors and the numi neutrino beam*, Physical Review Letters, 97 (2006), p. 191801.
- [17] T2K Collaboration, K. ABE *et al.*, *First muon-neutrino disappearance study with an off-axis beam*, Physical Review D, 85 (2012), p. 031103.
- [18] ANTARES Collaboration, S. ADRIÁN-MARTÍNEZ *et al.*, *Measurement of atmospheric neutrino oscillations with the antares neutrino telescope*, Physics Letters B, 714 (2012), p. 224.
- [19] IceCube Collaboration, M. G. AARTSEN *et al.*, *Determining neutrino oscillation parameters from atmospheric muon neutrino disappearance with three years of icecube deepcore data*, Physical Review D, 91 (2015), p. 072004.
- [20] OPERA Collaboration, N. AGAFONOVA *et al.*, *Discovery of tau neutrino appearance in the cngs neutrino beam with the opera experiment*, Physical Review Letters, 115 (2015), p. 121802.
- [21] R. DAVIS JR., D. HARMER, AND K. HOFFMAN, *Search for neutrinos from the sun*, Physical Review Letters, 20 (1968), p. 1205.
- [22] K. ZUBER, *Neutrino physics*, CRC Press, Taylor and Francis Group, 2 ed., 2012.
- [23] KamLAND Collaboration, S. ABE *et al.*, *Precision measurement of neutrino oscillation parameters with kamland*, Physical Review Letters, 100 (2008), p. 221803.
- [24] Daya Bay Collaboration, F. P. AN *et al.*, *Observation of electron-antineutrino disappearance at daya bay*, Physical Review Letters, 108 (2012), p. 171803.
- [25] S. J. PARKE, *CP violation in the neutrino sector*, 2008. Flavor physics and CP violation conference, Taipei.
- [26] AY SMIRNOV, *The MSW Effect and Matter Effects in Neutrino Oscillations*, Physica Scripta, T121 (2005), pp. 57–64.
- [27] P. HUBER, M. LINDNER, AND W. WINTER, *Simulation of long-baseline neutrino oscillation experiments with GLOBES (General Long Baseline Experiment Simulator)*, Computer Physics Communications, 167 (2005), p. 195.
- [28] H. NUNOKAWA *et al.*, *CP violation and neutrino oscillations*, Progress in particle and nuclear physics, 60 (2008), pp. 338–402.
- [29] NO ν A Collaboration, P. ADAMSON *et al.*, *First measurement of electron neutrino appearance in NO ν A*, Phys. Rev. Lett., 116 (2016), p. 151806.
- [30] MINER ν A Collaboration, K.S. MCFARLAND, *MINER ν A: a dedicated neutrino scattering experiment at NuMI*, Nuclear Physics B - Proceedings Supplements, 159 (2006), pp. 107 – 112.

-
- [31] T. MICELI, *Exploring Neutrino Interactions with MicroBooNE*, in 34th International Symposium on Physics in Collision (PIC 2014) Bloomington, Indiana, United States, September 16-20, 2014, 2014.
- [32] A. ANOKHINA *et al.*, *Prospects for the measurement of muon-neutrino disappearance at the FNAL-Booster*, (2014).
- [33] G. SIRRI, *The cngs neutrino beam*, Nuclear Physics B - Proceedings Supplements, 172 (2007), pp. 149 – 151.
- [34] D. HARRIS, *Conventional Beams*. Neutrino Physics Summer School Fermilab, 2007.
- [35] *The European Spallation Source*. <https://www.europeanspallationsource.se/>. ESS Technical Design Report, release 1.0, Nov. 2012.
- [36] A. LONGHIN, *A new design for the cern-fréjus neutrino super-beam*, The European Physical Journal C, 71 (2011), pp. 1–12.
- [37] S. E. KOPP, *Accelerator Neutrino Beams*, Physics Reports, 439 (2007), pp. 101–159.
- [38] S. VAN DER MEER, *A directive device for charged particles and its use in an enhanced neutrino beam*, CERN, Geneva, 1961.
- [39] R.B. PALMER, *Magnetic fingers*, (1965).
- [40] A. STAHL *et al.*, *Expression of Interest for a very long baseline neutrino oscillation experiment (LBNO)*, (2012).
- [41] Borexino Collaboration, G. BELLINI *et al.*, *Neutrinos from the primary proton-proton fusion process in the Sun*, Nature, 512 (2014), p. 383.
- [42] Borexino Collaboration, M. AGOSTINI *et al.*, *Spectroscopy of geoneutrinos from 2056 days of Borexino data*, Physical Review D, 92 (2015), p. 031101.
- [43] Double Chooz Collaboration, Y. ABE *et al.*, *Improved measurements of the neutrino mixing angle θ_{13} with the Double Chooz detector*, JHEP, 10 (2014), p. 086. [Erratum: JHEP02,074(2015)].
- [44] S.-B. KIM, *New results from RENO and prospects with RENO-50*, Nucl. Part. Phys. Proc., 265-266 (2015), pp. 93–98.
- [45] W. R. LEO, *Techniques for nuclear and particle physics experiments: a how-to approach*, Springer, 1992.
- [46] J. G. LEARNED, *High Energy Neutrino Physics with Liquid Scintillation Detectors*, (2009).
- [47] M. WURM *et al.*, *Optical Scattering Lengths in Large Liquid-Scintillator Neutrino Detectors*, Review of Scientific Instruments, 81 (2010), p. 053301.
- [48] A. B. BALANTEKIN *et al.*, *Neutrino mass hierarchy determination and other physics potential of medium-baseline reactor neutrino oscillation experiments*, in Proceedings, Community Summer Study 2013: Snowmass on the Mississippi (CSS2013): Minneapolis, MN, USA, July 29-August 6, 2013, 2013.
-

- [49] LAGUNA-LBNO Collaboration, T. PATZAK *et al.*, *LAGUNA-LBNO: Large Apparatus studying Grand Unification and Neutrino Astrophysics and Long Baseline Neutrino Oscillations*, Journal of Physics: Conference Series, 375 (2012), p. 042056.
- [50] M. WURM *et al.*, *The next-generation liquid-scintillator neutrino observatory LENA*, Astroparticle Physics, 35 (2012), pp. 685–732.
- [51] JUNO Collaboration, F. AN *et al.*, *Neutrino Physics with JUNO*, J. Phys., G43 (2016), p. 030401.
- [52] JUNO Collaboration, Z. DJURCIC *et al.*, *JUNO Conceptual Design Report*, (2015).
- [53] S. AGOSTINELLI *et al.*, *Geant4 - a simulation toolkit*, Nuclear Instruments and Methods in Physics Research Section A: Accelerators, Spectrometers, Detectors and Associated Equipment, 506 (2003), pp. 250 – 303.
- [54] J. ALLISON *et al.*, *Geant4 developments and applications*, IEEE Transactions on Nuclear Science, 53 (2006), pp. 270–278.
- [55] R. BRUN AND F. RADEMAKERS, *ROOT - An Object Oriented Data Analysis Framework*, Nuclear Instruments and Methods in Physics Research Section A: Accelerators, Spectrometers, Detectors and Associated Equipment, 389 (1997), pp. 81–86.
- [56] *The Periodic Table by WebElements*. <https://www.webelements.com/>. Accessed: 02.10.2016.
- [57] LAGUNA-LBNO Collaboration, S. K. AGARWALLA *et al.*, *The LBNO long-baseline oscillation sensitivities with two conventional neutrino beams at different baselines*, (2014).
- [58] P. HUBER, M. LINDNER, AND W. WINTER, *Simulation of long-baseline neutrino oscillation experiments with GLOBES (General Long Baseline Experiment Simulator)*, Comput. Phys. Commun., 167 (2005), p. 195.
- [59] P. HUBER AND J. KOPP AND M. LINDNER AND M. ROLINEC AND W. WINTER, *New features in the simulation of neutrino oscillation experiments with GLOBES 3.0: General Long Baseline Experiment Simulator*, Comput. Phys. Commun., 177 (2007), pp. 432–438.
- [60] S. LORENZ, *Topological track reconstruction in liquid scintillator and LENA as a far-detector in an LBNO experiment*. PhD Thesis.
- [61] M. BLENNOW AND P. COLOMA AND E. FERNANDEZ-MARTINEZ, *Reassessing the sensitivity to leptonic CP violation*, JHEP, 03 (2015), p. 005.
- [62] A. M. DZIEWONSKI AND D. L. ANDERSON, *Preliminary reference Earth model*, Physics of the Earth and Planetary Interiors, 25 (1981), p. 297–356.
- [63] F. D. STACEY, *Physics of the earth*, Wiley, 2 ed., 1977.
- [64] *China Spallation Neutron Source*. <http://csns.ihep.ac.cn/>.

- [65] J. WEI *et al.*, *China Spallation Neutron Source: Design, R&D, and outlook*, Nuclear Instruments and Methods in Physics Research Section A: Accelerators, Spectrometers, Detectors and Associated Equipment, 600 (2009), pp. 10 – 13.
- [66] D. HELLGARTNER, *Advanced event reconstruction in LENA and precision attenuation-length measurements in liquid scintillators*. PhD Thesis, Munich Technical University, 2015.
- [67] M. SOIRON, *Studies on the sensitivity of liquid scintillator detectors for the measurement of the neutrino mass hierarchy with atmospheric neutrinos*. PhD Thesis, RWTH Aachen University - in preparation.
- [68] J.H. HOLLAND, *Adaptation in natural and artificial systems*, MIT Press, 1975.
- [69] R. M. D. BEASLEY, D.R. BULL, *An overview of genetic algorithms: Part 1. Fundamentals*, University computing, 15 (1993), pp. 58–58.
- [70] A. E. EIBEN AND C. SCHIPPERS, *On evolutionary exploration and exploitation*, 1998.
- [71] T. BLICKLE AND L. THIELE, *A comparison of selection schemes used in evolutionary algorithms*, Evolutionary Computation, 4 (1996), pp. 361–394.
- [72] A. LIPOWSKI AND D. LIPOWSKA, *Physica A: Statistical Mechanics and its Applications*, 391 (2012), pp. 2193 – 2196.
- [73] M. LITZKOW AND M. LIVNY AND M. MUTKA, *Condor - a hunter of idle workstations*, in Proceedings of the 8th International Conference of Distributed Computing Systems, June 1988.